

**Optimal Template Placement for  
Searches of Gravitational Waves  
from  
Precessing Compact Binary  
Coalescences**

Von der Fakultät für Mathematik und Physik  
der Gottfried Wilhelm Leibniz Universität Hannover  
zur Erlangung des akademischen Grades

Doktor der Naturwissenschaften  
Dr. rer. nat.

genehmigte Dissertation

von

**B. S. Nathaniel Michael Indik**

geboren am 30.06.1990 in Tucson, AZ, USA

**2018**

**Referent:**

Prof. Dr. rer. nat. Stanislav Babak  
APC Laboratory  
Paris, France

**Korreferent:**

Prof. Dr. rer. nat. Andrew Lundgren  
University of Portsmouth  
Portsmouth, UK

**Korreferentin:**

Prof. Dr. rer. nat. Archana Pai  
Department of Physics  
Indian Institute of Technology Bombay  
Bombay, India

**Tag der Promotion:**

16.04.2018

## 0.1 Kurzzusammenfassung

Mit der Entdeckung eines Gravitationswellensignales (GW150914) am Montag dem 14. September 2015 wurde ein neues Kapitel in der Astrophysik aufgeschlagen. Die Beobachtung von Gravitationswellen, erzeugt durch Neutronenstern-Schwarzes-Loch-Kollisionen konnte bislang nicht beobachtet werden. Insbesondere wäre eine Beobachtung von Neutronenstern-Schwarzes-Loch-Verschmelzungen interessant, da es eine weitere Möglichkeit bietet, Gravitationswellensignale zusammen mit elektromagnetischen und Neutrinoemissionen zu beobachten. Die Schwierigkeit beim Entdecken von präzedierenden Neutronenstern-Schwarzes-Loch-Binärsystemen (Systeme, die den gesamten Bereich von physikalisch erlaubten Spin-Konfigurationen zulassen) ist, dass die Template-Bank für präzedierende verschmelzende kompakte Binärsysteme viel mehr Templates erfordert als bereits zuvor implementierte Template-Banks.

Der Zweck dieser Dissertation ist sowohl die Konstruktion als auch die Effizienz der kompakten binären Koaleszenz Template-Banks zu verbessern. Die Konstruktion einer Template-Bank im hochdimensionalen Parameterraum für präzedierende verschmelzende kompakte Binärsysteme wird weiter erschwert durch das Fehlen eines analytischen Ausdrucks der Inspiral-Merger-Ringdown-Metrik. Bislang konnten deshalb nur die ineffizienten, langsam konvergierenden stochastisch erzeugten Template-Banks genutzt werden. In dieser Dissertation, konstruierte ich eine Template-Bank, die *Face-on-Precessing* Template-Bank, in einem Unterraum dieses präzedierenden Neutronenstern-Schwarzes-Loch Template-Bank Parameterraums. Dazu habe ich einen neuen Algorithmus entwickelt, der Konvergenz der stochastischen Platzierung dieser Templates beschleunigt. Dieser Teilraum benötigt 53 Mal mehr Templates als die Aligned-Spin-Bank. Zusätzlich entwickelte ich eine Methode, um Template-Banks durch Verschiebung der Templates zu optimieren, den Template-Nudging-Algorithmus. Diese Methode eliminiert die Wirkung von *Gridlines*. Diese künstlich dichten Regionen der Template-Bank sind charakteristisch für hybride Template-Bank-Konstruktionsmethoden, die zuvor in LIGO-Virgo Suchen nach Verschmelzungen kompakter Binärsysteme implementiert wurden. Schließlich entwickelte ich eine Koordinatentransformation in einen flachen Raum, um den Aufbau einer vollständigen Template-Bank für präzedierende verschmelzende kompakte Binärsysteme zu erleichtern.

## 0.2 Abstract

A new field of astronomy was opened up on Monday September 14<sup>th</sup> 2015, when the first detection of a *Gravitational Wave* was observed, GW150914. So far there have been no observations of gravitational waves produced from neutron-star–black-hole mergers. The observation of a neutron-star–black-hole merger would be significant because it would provide another way to study how compact binary coalescence gravitational wave signals relate to companion electromagnetic and neutrino emission signals. The difficulty in detecting precessing neutron-star–black-hole binaries (systems that allow for the full range of physical spin configurations) is that template banks for these precessing compact binary coalescence systems require many more templates than compact binary coalescence template banks that have been implemented previously.

The purpose of the work presented in this thesis is to both improve the construction and efficiency of compact binary coalescence template banks. Template bank construction in the high dimensional precessing compact binary coalescence parameter spaces is complicated by the absence of a known analytic expression of mismatch inspiral-merger-ringdown metric. Previously, these restraints only permitted the use of the inefficient and slow to converge stochastic template placement algorithms. In this thesis, I constructed a template bank, the *face-on-precessing* template bank, over a subspace of this precessing neutron-star–black-hole template bank parameter space. I accomplished this by implementing a new algorithm for speeding up the convergence of the stochastic placement of these templates. I found that this subspace required 53 times more templates than the aligned-spin bank. Additionally, I developed an alternative template placement algorithm, the template nudging algorithm, to reposition compact binary coalescence templates into more effectual configurations in order to eliminate the effect of gridlines, artificially dense regions of the bank, that are characteristic of the hybrid template bank construction methods previously implemented in LIGO-Virgo compact binary coalescence searches. Finally, I developed a technique for constructing flat coordinates for compact binary coalescence template placements in high dimensional parameter spaces to ease in the construction of a fully precessing compact binary coalescence template bank.

0.1	Kurzzusammenfassung	3
0.2	Abstract	4
<b>1</b>	<b>Introduction</b>	<b>11</b>
1.1	Compact Binary Coalescence	11
1.1.1	Stellar remnants	11
1.1.2	Gravitational waves	19
1.1.3	Compact binaries	28
1.1.4	Waveform models	31
1.1.5	Chirp time	35
1.1.6	Precessing NSBH waveform derivation	38
1.2	Matched filtering	41
1.3	Search pipeline	45
1.4	Acknowledgments	49
<b>2</b>	<b>Template Banks</b>	<b>51</b>
2.1	Geometric lattices	51
2.2	Stochastic placement algorithm	56
2.3	Hybrid methods	60
<b>3</b>	<b>Constructing a face-on precessing NSBH template bank</b>	<b>67</b>
3.1	Cell splitting methodology	69
3.2	The precessing face-on template bank (FOB)	70
3.3	Effectualness of the template bank	77
3.4	Conclusions	83
3.5	Acknowledgments	83
<b>4</b>	<b>Template Nudging</b>	<b>85</b>
4.1	Template nudging algorithm	86
4.1.1	Neighboring cell algorithm	88
4.2	Application to the CBC aligned-spin NSBH template bank	88
4.2.1	Isosurface geometry in chirp time coordinates	88
4.2.2	Template isosurfaces	89
4.2.3	Cell Structure	91
4.3	Results	92
4.4	Conclusions	94
4.5	Acknowledgments	97

<b>5</b>	<b>Method for flattening CBC parameter spaces</b>	<b>99</b>
5.1	Gaussian normal coordinates . . . . .	99
5.2	Flattening CBC parameter spaces . . . . .	101
5.3	Conclusions . . . . .	104
<b>6</b>	<b>Conclusion</b>	<b>105</b>
<b>7</b>	<b>Nathaniel Michael Indik</b>	<b>107</b>
7.1	Personal Data . . . . .	107
7.2	Education . . . . .	107
7.3	Awards . . . . .	108
7.4	Technologies . . . . .	108
7.5	Professional Experience . . . . .	108
7.6	Presentations . . . . .	108
7.7	Publication List (excluding LVC papers) . . . . .	109
<b>8</b>	<b>Acknowledgments</b>	<b>111</b>

## LIST OF FIGURES

1.1	Hubble image of the white-dwarf Sirius B [190] . . . . .	13
1.2	CHANDRA X-ray image of the Vela pulsar [76, 99]. . . . .	14
1.3	Observations by the W. M. Keck Observatory of Sagittarius A* [182, 181]. . . . .	18
1.4	GW150914, the first observation of a gravitational wave in the LIGO Hanford (H1) (left column) and Livingston (L1) (right column) detectors likely produced from the merger of two black holes [18]. . . . .	21
1.5	Orbital decay in the binary pulsar B1913+16 system demonstrated as an increasing orbital phase shift for periastron over time [171]. . . . .	23
1.6	Illustration of the location of the two LIGO detectors, a simplified diagram of the components of each Michelson interferometer and the characteristic sensitivity of the two LIGO detectors [18]. . . . .	24
1.7	A comparison of the time sequences of a selection of observed gravitational waves in the first two detection eras of LIGO-Virgo [167]. . . . .	26
1.8	The sky location and optical telescope images of the first observation of a gravitational wave with a coincident EM signal likely produced by the merger of two neutron stars [26]. . . . .	27
1.9	A flowchart for a possible model of evolution for a CBC systems [220]. . . . .	29
1.10	Diagram of parameters used to describe precession . . . . .	39
1.11	The PyCBC time-slide significance analysis of the of the observation run that led to the detection of GW150914 [14]. . . . .	47
2.1	An $A_2^*$ (i.e. hexagonal) lattice used to build a geometric bank [224]. . . . .	53
2.2	A plot of a BNS TaylorF2 template bank in $\xi$ coordinates [62]. . . . .	55
2.3	An example of a stochastic generated distribution of templates [120]. . . . .	56
2.4	Comparison of the match metric approximant implemented in Sbank and the real match. . . . .	59
2.5	Scatter plot of the component mass parameter space used in the construction of Uberbank and a plot of the recovered fitting factors obtained from a banksim of Uberbank [15]. . . . .	60
2.6	Scatter plots of <i>Hyperbank</i> , the template bank implemented in the O2 search [89]. . . . .	61
2.7	Plot of the recovered fitting factors obtained from several banksims of Hyperbank the template bank implemented in the O2 search [89]. . . . .	62
2.8	Density plot of the NSBH region of Hyperbank [89]. . . . .	64
2.9	Density plot of an NSBH stochastic template bank generated using <code>pycbc_geom_bank</code> [89]. . . . .	65
2.10	Density plot of an NSBH stochastic template bank generated using SBank [89]. . . . .	66

3.1	Convergence curves of three different cells used to construct the FOB [146]. . . . .	71
3.2	The aligned spin bank (ASB) plotted in chirp time coordinates [146]. . . . .	72
3.3	The FOB plotted in chirp time coordinates [146]. . . . .	72
3.4	Normalized distribution of the mass-ratio $q$ for the face-on precessing template and ASB [146]. . . . .	73
3.5	The component mass distribution of the FOB [146]. . . . .	74
3.6	The FOB plotted in $(q, \chi^{\parallel})$ coordinates. . . . .	74
3.7	The spin distribution of the FOB [146]. . . . .	75
3.8	The precession cone, $\beta$ and mass ratio, $q$ , distribution of the FOB [146]. . . . .	75
3.9	Plot of the templates in the cell $(\tau_0, \tau_3) = (0.14-0.15, 40-44)$ that had an overlap greater than 95% with templates placed in the cell, $(\tau_0, \tau_3) = (0.14-0.15, 36-40)$ [146]. . . . .	76
3.10	An example of vertical gridlines in the FOB. . . . .	76
3.11	Comparison of the stochastic bank and the metric approximant distributions [146]. . . . .	77
3.12	Cumulative histogram showing the recovered fitting factor of the face-on-precessing and aligned spin template banks for face-on <b>SpinTaylorF2</b> injections [146]. . . . .	78
3.13	Cumulative histogram showing the recovered fitting factor of the face-on-precessing and aligned spin template banks for <b>SpinTaylorF2</b> injections with the component masses distributed uniformly within their respective ranges, spins distributed uniformly in $\kappa$ , and $\hat{\mathbf{J}}$ distributed uniformly over the sphere [146]. . . . .	79
3.14	A plot of the difference in the recovered fitting factor between the precessing and aligned template banks over the $\{\tau_0, \tau_3\}$ parameter space for face-on <b>SpinTaylorF2</b> injections [146]. . . . .	79
3.15	A plot of the difference in the recovered fitting factor between the precessing and aligned template banks over the $\{\tau_0, \tau_3\}$ parameter space for <b>SpinTaylorF2</b> injections that are distributed uniformly in chirp time, $\{\tau_0, \tau_3\}$ , with $\hat{\mathbf{J}}$ distributed uniformly over the sphere [146]. . . . .	81
3.16	A plot of the difference in the recovered fitting factor between the precessing and aligned template banks over the $\{q, \chi^{\parallel}\}$ parameter space for face-on <b>SpinTaylorF2</b> injections [146]. . . . .	81
3.18	Recovered fitting factor of the precessing template bank over the $\{\theta_J, \beta\}$ parameter space with <b>SpinTaylorF2</b> injections that are distributed uniformly in chirp time, $\{\tau_0, \tau_3\}$ , with $\hat{\mathbf{J}}$ distributed uniformly over the sphere. . . . .	82
3.17	A plot of the difference in the recovered fitting factor between the precessing and aligned template banks over the $\{q, \chi^{\parallel}\}$ parameter space for <b>SpinTaylorF2</b> injections that are distributed uniformly in chirp time, $\{\tau_0, \tau_3\}$ , with $\hat{\mathbf{J}}$ distributed uniformly over the sphere [146]. . . . .	82
4.1	Flowchart of the template nudging algorithm procedure [145]. . . . .	86
4.2	Diagram of a simplified example displaying how template are repositioned in the NCA and template nudging algorithms [120]. . . . .	87
4.3	Template isosurface corresponding to $\{M_{BH} = 10M_{\odot}, M_{NS} = 1.4M_{\odot}, \chi_{BH} = 0.5\}$ plotted in chirp time coordinates $\{\tau_0, \tau_2, \tau_3\}$ [145]. . . . .	89
4.4	Some examples of template isosurfaces plotted in chirp time and physical coordinates [145]. . . . .	90
4.5	The improvement in the effectualness of the template bank after applying the nudging algorithm [145]. . . . .	92
4.6	The relative detection volume of the nudged bank relative to the stochastic bank [145]. . . . .	93



4.7	The relative detection volume improvement of the nudged bank relative to the original template bank [145]. . . . .	93
4.8	Comparison of fitting factors for the nudging algorithm and a closeup of the template distribution in the highly anti-aligned region of the NSBH parameter space [145]. . . . .	95



*Template banks*, the collections of signals used to *matched filter* noisy data, are an integral part to detecting *Gravitational Waves* (GWs). Determining which signals should be included in these banks is difficult to do in practice. Maximizing the likelihood of detecting gravitational waveforms produced from Compact Binary Coalescences (CBCs) requires considering a high number of search parameters. In this chapter I provide a background on the astrophysics of compact objects, the CBC gravitational waveform models produced by these objects that are placed in these template banks and the role of template banks in the LIGO-Virgo [12, 29] search pipelines (PyCBC [88, 255, 196], GstLAL [69, 223, 180] and MBTA [30]).

Chapter two describes previous methods used in CBC template bank construction. Chapter three describes a method for constructing a *face-on precessing* neutron-star-black-hole (NSBH) template bank. Chapter four describes an alternative method for template placement that repositions templates into more effectual configurations (*template nudging*) without adding additional templates. This method can reduce the number of templates required to detect CBC signals when used in conjunction with other template placement methods. Chapter five describes a method for improving CBC template bank placement coordinates by demonstrating a method that transforms the non-spinning binary-neutron-star (BNS) 2.5 PN inspiral parameter space into a coordinate system that “flattens” the mismatch metric. Chapter six summarizes how these projects have contributed to the art of template bank construction and how they can be applied to future searches for gravitational wave searches. Chapter seven is my *Curriculum vitae*.

## 1.1 Compact Binary Coalescence

### 1.1.1 Stellar remnants

A *compact object* or *stellar remnant*, is the final remnant stage of a massive star (e.g. a main sequence star [231, 246]). The template banks I have constructed in this thesis are built to detect these astrophysical objects.

At this terminal stage in stellar evolution, the star has exhausted its fusible atomic fuel to the point where the pressure of its atomic fusion is overpowered by the gravitational force of its outer layers onto its stellar core. As a result of the imbalance of these two competing forces, the star’s volume is compressed down into a fraction of its previous volume [274]. Depending on the mass of the *progenitor* main sequence star, the following compact objects are formed:

white-dwarfs (WDs), neutron-stars (NSs), and black-holes (BHs)<sup>1</sup>.

## White-dwarfs

White-dwarfs were the first examples of compact objects in the observable universe. They are different from stars like the Sun because they are a terminal phase of stellar evolution. While the template banks I constructed in this thesis (see Chapters 3 and 4) are not built to search for white-dwarfs, they nonetheless play an important role in the history of compact objects.

Discussions of compact matter were first prompted by W. S. Adams’ discovery of Sirius B (see Figure 1.1) a “white” compact companion star to Sirius A in 1914 [31]. This star’s mass was inferred from its orbit around Sirius A via Kepler’s third law and its surface temperature was inferred by an analysis of the Blackbody spectrum of the white-dwarf star. The blackbody spectrum of Sirius B was surprisingly similar to the white spectrum of Sirius A, and this led Adams to conclude that the object was extremely dense, with a mass between  $0.75 - 0.95M_{\odot}$ , a surface temperature of 8000 K and a radius of 18,000 km<sup>2</sup>. Equipped with new tools for General Relativity (see Section 1.1.1), Sir Arthur S. Eddington later attempted to better estimate Sirius B’s density by calculating the red shift of Sirius A’s blackbody spectrum. In 1926, Eddington published a book [102], stating that WDs were likely to be very abundant in the universe.

That same year, R. H. Fowler applied the newly developed theory of Fermi-Dirac statistics [121, 7] to better explain the formation of such dense stars [125]. He theorized that an *electron degeneracy pressure* prevented further gravitational collapse of the compact object. Such a pressure arises from the fact that electrons are *fermions*. As the density of the star’s matter increases, the spacing between atoms decreases. Once that spacing approaches the scale of the electron Compton wavelength, the Pauli exclusion principle [211] dictates that additional energy must be added to the system to ensure that the electrons do not occupy the same spin and orbital state. This results in an endothermic process and overall outward pressure resisting further compression.

Edmund C. Stoner [243, 244] and Wilhelm Anderson [36] were the first to attempt to build a model for the equation of state of white dwarf matter. Originally, Stoner implemented a non-relativistic formulation of the electron degeneracy pressure. Anderson brought to Stoner’s attention that for more massive white-dwarfs relativistic corrections must be considered. They developed the Stoner-Anderson equation of state. Due to a flawed implementation of the newly developed theory of special relativity, they (accidentally) found that there was a maximum allowable mass limit for white-dwarf stars.

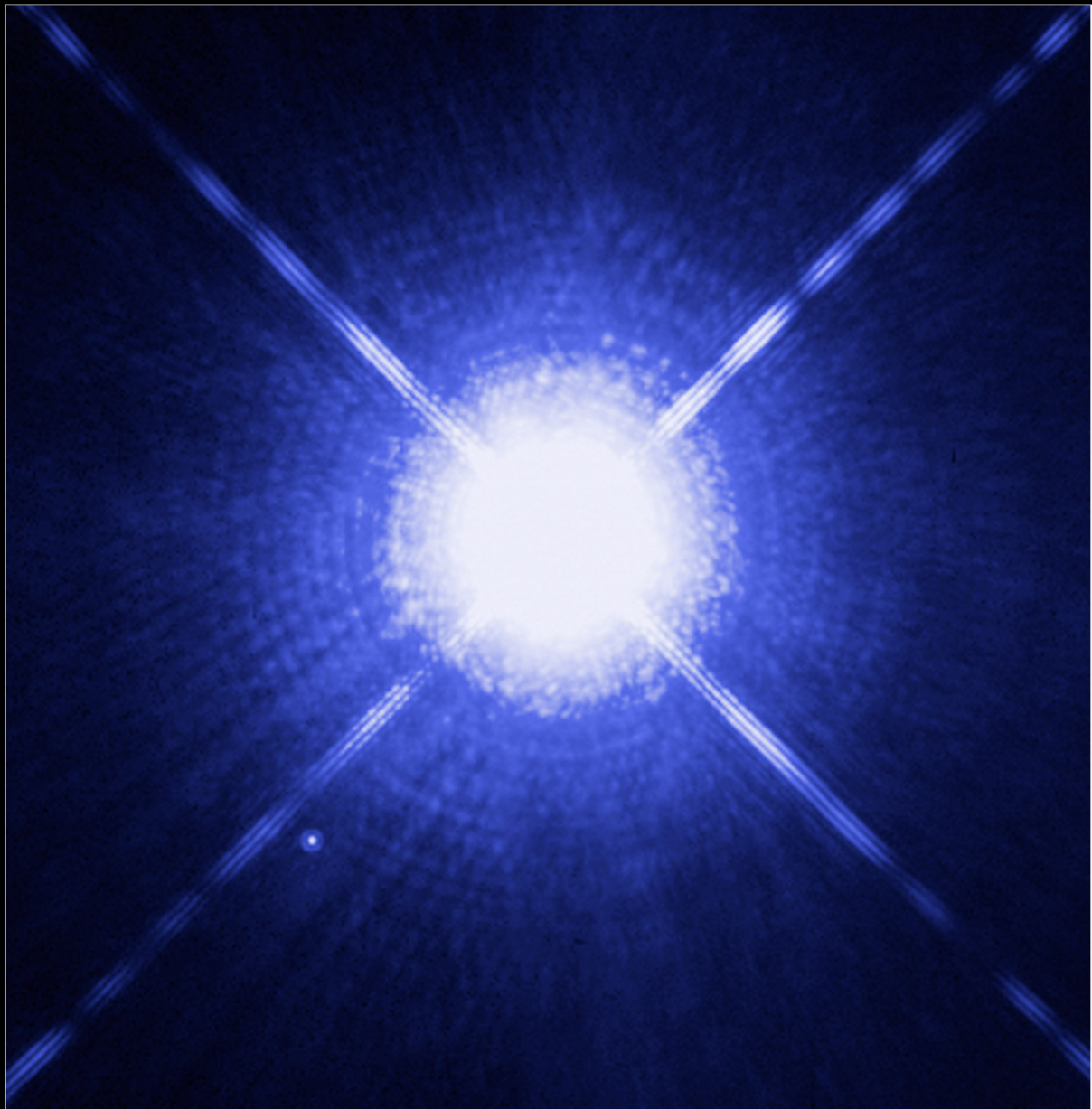
The mass limit was confirmed with better models built by Subrahmanyan Chandrasekhar and Lev D. Landau independently in the early 1930’s [79, 78, 77, 8]. Landau proposed that the maximum mass for white dwarfs was inversely proportional to the square of the “mass of the matter per electron”,  $m$ . Chandrasekhar first estimate was too low,  $0.91M_{\odot}$  [276], because he assumed the mass of the matter per electron was too high  $2.5m_p$  ( $m_p$  is the proton mass). On the other hand, Landau was closer  $1.5M_{\odot}$  [276] assuming  $2m_p$ , slightly overestimating Chandrasekhar’s recalculated value in 1935,  $1.44M_{\odot}$  [276].

The current consensus is that white-dwarfs are an equilibrium state of stellar matter achieved once a main sequence star has fused helium and hydrogen in its core to the point where the star has an abundance of carbon and oxygen [i.e. C-O WDs] (and possibly neon [i.e. C-O-N WDs] [130, 267]) in its core. These stars have masses comparable to or lower than our Sun (such stars have been observed in the mass range  $M \in \{0.17M_{\odot} - 1.33M_{\odot}\}$  [157, 151, 272]. The maximum

---

<sup>1</sup>Legal disclaimer: “The content and portions of the text presented in this section are taken from [238, 276, 239, 169] with minor paraphrasing. The use of this material is protected under ‘Fair Use’ (UrHG §24,70,63) and consistent with the requirements of § 6 Abs. 1 PromO.”

<sup>2</sup>This estimate would later be refined; Sirius B has more recently been measured to have mass  $1.018 \pm 0.011M_{\odot}$  [59] and radius  $0.0084 \pm 0.00025R_{\odot}$  [141].



Sirius A and Sirius B  
Hubble Space Telescope • WFPC2

NASA, ESA, H. Bond (STScI), and M. Barstow (University of Leicester)

STScI-PRC05-36a

Figure 1.1: Hubble image of the white-dwarf Sirius B (7,500 mi in diameter) [small white star on the lower left] and its 10,000 times more luminous companion star Sirius A (the most luminous star visible in the night sky) [large bright white star in the center]. The stars revolve around each other every 50 years. Its surface temperature has been approximated to be 25,200K. This image was taken Oct. 15<sup>th</sup>, 2003, with Hubble's Wide Field Planetary Camera 2 and the caption is taken from the same source with minor paraphrasing [190].

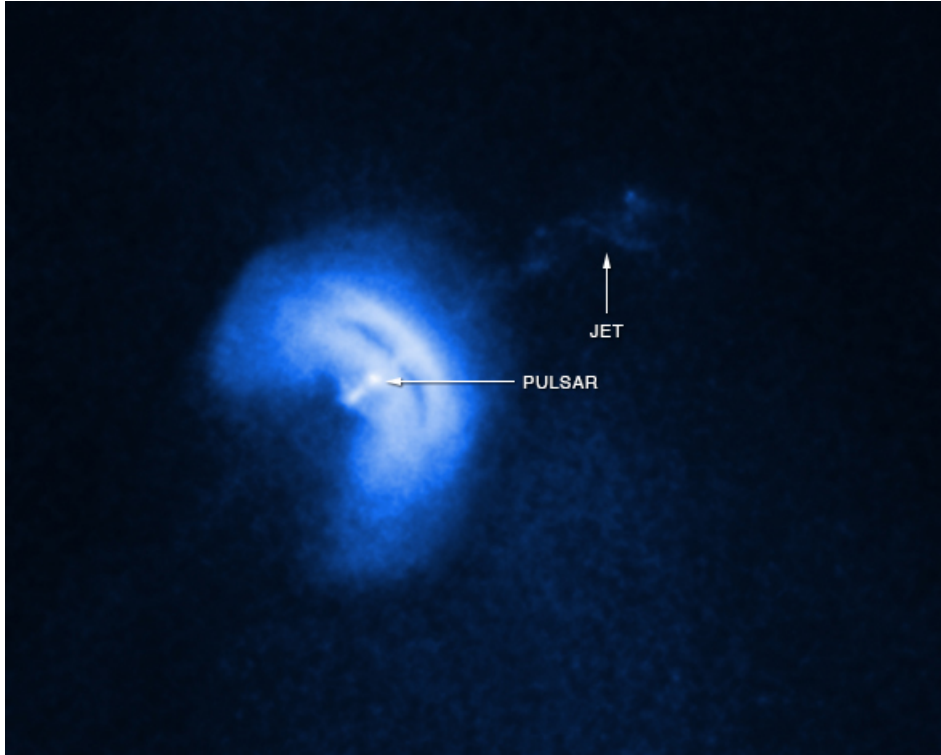


Figure 1.2: CHANDRA X-ray image of the Vela pulsar. The pulsar and the associated jet are labeled in white and indicated by white arrows. The Vela pulsar is 1,000 light years away from Earth, with a 12 mile diameter and rotation speed of 11 times per second. The jet of charged particles is approximately 0.7 light years in length. This image was taken in 2010 by CHANDRA and the caption is copied with minor paraphrasing from [76, 99].

progenitor mass is estimated to be between  $6 - 9.5M_{\odot}$  [272]. These stars form because the radiation pressure created from core fusion decreases such that the weight of the outer layers of the star compress the star. At this point, further gravitational collapse is prevented by the electron degeneracy pressure. White-dwarfs will continue to radiate its remaining energy via blackbody radiation. Theoretically as a white-dwarf continues to radiate energy, it will cool down and the wavelength of the blackbody spectrum will grow (becoming more red). Eventually these objects could stop radiating any observable EM radiation theoretically becoming *black dwarfs*.

## Neutron-stars

The existence of neutron-stars was a byproduct of attempts to calculate the white-dwarf maximum mass limit. Neutron-stars are prime target for gravitational wave searches due to their extremely compact composition and ability to produce observable electromagnetic radiation. They are components to the “neutron-star-black-hole binaries” and “binary-neutron-star” that are the targets for the template banks I construct in Chapters 3 and 4. In this subsection I provide a historical background and short discussion of the properties of these compact objects.

Landau proposed the existence of these denser stars prior to James Chadwick’s announcement of the discovery of the neutron in 1932 [74, 75], which were theorized to exist in 1920 by Lord Ernest Rutherford [6]. Landau made a completed a draft of this paper around the time Chadwick had first reported his findings to Niels Bohr in 1931 [276]. He came to his conclusion by considering what happens when stellar densities are so high that “the laws of quantum mechanics break down”. However this view was flawed and it would eventually be

shown that there are objects above the Chandrasekhar limit are still consistent with the laws of quantum mechanics.

In 1934, Walter Blaade and Fritz were the first coin the terms “Super-Novae” and “neutron star” in a publication [41]; the term neutron-star was conceived when they studied the enormous energies released during supernovas. They speculated that an immense gravitational binding energy must be released to justify the large amounts of power associated with these type of phenomena. They proposed that “supernovae represent the transition from ordinary stars into neutron stars, which in their final stages consist of closely packed neutrons” [41, 42, 276]; exceeding the compactness of white dwarfs. This was a very early attempt to model this type of extremely compact matter and it would be later refined by others. They made the mistake of proposing that the tightly packed neutrons were formed on the surface of the star and “rain” down toward the stellar core [42]. In 1937, Landau followed up his earlier model with a model for dense stars “where all the nuclei and electrons have combined to form neutrons” throughout the core of the star [162], which was closer to the current consensus for what the composition of these object look like<sup>3</sup>.

After decades of additional studies, much more is now known about these compact objects. Neutron-stars can theoretically have masses between  $\{1.39 - 3M_{\odot}\}$  [163, 71, 35]. They are formed as stellar remnants produced by *type II, Ib or Ic* super novae of a progenitor star with initial mass  $M \in \{8 - 29M_{\odot}\}$  [274]. Each “type” of supernova relies on a different mechanism for the *detonation* of the progenitor mass in order to produce the remnant star. The mass and evolutionary history of the progenitor star will determine which type of supernova it will undergo at this terminal phase of its evolution.

Unlike WDs, NSs have a sufficiently dense and hot stellar core to fuse carbon and heavier atoms. These stars continue to fuse atoms in their cores producing increasingly massive atoms. Eventually these cores will contain an abundance of iron. Fusing iron is an endothermic process; it requires more energy to be fused than is subsequently released. Once the stellar core temperature reaches  $5 \times 10^9$  K, the remnant iron stellar core is broken up further via photodisintegration [100, 270, 222] (a process in which iron nuclei are broken apart into alpha particles and neutrons by high energy gamma radiation). The protons of the former iron nuclei are further fused together to form neutrons by electron capture, thus yielding the titular neutron rich core of the NS. Further collapse is prevented by the neutron degeneracy pressure. This remaining mass of atoms is extremely dense<sup>4</sup> and they do not radiate energy through fusion. As a point of reference, these objects are so dense that a star twice as massive as our Sun would fit within the city limits of Washington D.C., and would have a density  $3 \times 10^{14}$  times that of our Sun.

In the neutron-star core, the velocity of sound approaches light speed and the surface strength of the magnetic field can be as high as  $2 \times 10^{15}$  Gauss [4, 202, 273]<sup>5</sup>. Due to the extreme heat and density of these objects they are difficult to produce in a laboratory setting, apart from their mass and electromagnetic emissions not much is known about their composition (principally the *Equation Of State*, EOS, the relationship between pressure and density within the core [203, 205]). One unique aspect of these objects is the fact that they can emit beams of high energy particles at their magnetic poles [132, 209, 172].

As a consequence of the remnant’s explosive formation, these objects typically rotate very quickly<sup>6</sup>. When the axis of rotation of the star is disparate from the poles of the magnetic field, the star appears to *pulse* in the electromagnetic (EM) regime of for an off-axis observer

---

<sup>3</sup>Having said that, it is also important to remember that a consensus alone is not sufficient to prove the validity of a theory [194, 39].

<sup>4</sup>Neutron-star radii range approximately from 6.2 – 22.6km [164, 131, 163]

<sup>5</sup>Earth’s magnetic field is on average approximately 0.5 Gauss.

<sup>6</sup>Neutron-star surface speeds can be up to a third of the speed of light [140] and rotational periodicity between  $10^{-2}$  and  $10^3$ Hz [10]

creating a *lighthouse effect* of EM emissions [172]. Such NS spin configurations are referred to as *pulsars* (see Figure 1.2), and yield a convenient type of stellar clock for astronomers since the pulsar periodicity is quite regular, typically decaying at a rate between  $10^{-9}$  and  $10^{-18}$  Hz/s [10].

## Black-holes

The history of black-hole research was a culmination of the work done to study white dwarfs, neutron-stars, and the theory of General Relativity. In 1939 [204] Robert J. Oppenheimer and Hartland Snyder made the suggestion that neutron star cores could become so massive that they will become unstable such that the escape velocity required to leave the surface of such an object would exceed the speed of light [169]. Oppenheimer and George Volkoff later bolstered this claim by finding that there was no stable solution for extremely dense stellar matter [205]. John Wheeler is often credited with coining the name “black-hole” during a lecture in 1967 [239]. However, it is unclear if this is indeed the first occurrence of the word. Some sources claim that the term was first printed in Science News Letter in 1964 by Ann Ewing, a journalist, who summarized the talks presented at the January Cleveland American Association for the Advancement of Science (AAAS) meeting that year [117, 239]. Locating where the term was first used before this date remains ambiguous to this day [239].

Due to their extreme compactness (the ratio of mass over radius), stellar black holes have an immense gravitational pull such that Newtonian physics is not sufficient to explain their physical properties. William Kingdon Clifford discussed the idea that the motion of matter is due to the geometry of space-time in 1876 [241, 83]<sup>7</sup>. In 1908, Albert Einstein published article on “special relativity” and he also introduced the “equivalence principle”, arguing that gravitational free fall is equivalent to inertial motion [111]. Albert Einstein collaborated with his colleague Marcel Grossmann to further develop this new theory by quantifying distances in space geometry via a mass dependent space-time metric  $g_{\mu\nu}$  [245]. Einstein published a follow up paper on special relativity [112] in 1911 and finally in 1915, Einstein published the theory of General Relativity [115, 113, 114].

General Relativity provided a new mathematical framework for describing the properties of gravity which would become crucial to understanding compact matter in regimes where classical physics breaks down. Karl Schwarzschild applied General Relativity to model an uncharged, non-rotating sphere and obtained a limit for the radius, the *Schwarzschild radius* [236]<sup>8</sup>, within which the escape velocity exceeds light speed. This limit quantified the radius of the *event horizon* of what would later be referred to as a “black-hole”<sup>9</sup>. This *Schwarzschild solution* was significant because it was the first exact solution to a problem in General Relativity.

Soon after Schwarzschild discovery, Hans Reissner [225] and Gunnar Nordström [198] included electric charge into Schwarzschild’s solution and developed the Reissner-Nordström metric. In 1921 and 1922 Paul Painlevé [210]<sup>10</sup> and Allvar Gullstrand [133] developed a set of coordinates, Gullstrand-Painlevé coordinates, for Schwarzschild’s solution that eliminated the horizon coordinate singularity [165].

There was little progress in this field of research for a few decades, and further work on studying extremely compact matter would not pick up again until the late 1950s. In 1963, Roy

---

<sup>7</sup>Clifford’s work was an application of Bernhard Riemann’s and Carl Friedrich Gauss’ work on differential geometry [227, 2].

<sup>8</sup>Schwarzschild published this work and two other historically significant papers over the age of 40 while volunteering to serve for the German military on the Russian front in WWI. He died in Potsdam in 1916; he had been struggling with a rare autoimmune disease pemphigus [103, 200].

<sup>9</sup>Schwarzschild considered his solution to be purely theoretical and had no physical meaning [200] due to the existence of coordinate singularities in his solution.

<sup>10</sup>To some people, Painlevé is better known as the 62<sup>nd</sup> Prime Minister of France [195].



P. Kerr generalized Schwarzschild’s solution to an uncharged spinning black-hole and developed the *Kerr metric* [153]. In 1965, Kerr and Ezra “Ted” Newman incorporated charge into Kerr’s original solution developing the Kerr-Newman metric [193, 192].

Black-holes are the stellar remnants produced by main sequence stars with mass greater than  $20M_{\odot}$  [116]. The dense cores of such stars are characterized by their high mass, greater than 2 or 3  $M_{\odot}$ <sup>11</sup>, exceeding the Tolman-Oppenheimer-Volkoff [TOV] limit [205]). Due to the absence of any known physical process to counter collapse caused by the immense gravitational pull of the object’s outer layers on its core, the object collapses to a singularity. Unlike the coordinate singularity present in Schwarzschild’s solution, this singularity is intrinsic to the manifold and can not be removed via changing the coordinates. Not much is currently known about these singularities as General Relativity alone is not sufficient to explain their internal structure. Since they occur within the event horizon, electromagnetic observations of these singularities are not possible.

All mass and energy associated with the black-hole are confined within the *Schwarzschild Radius* [236]. Within this threshold radius, mass and energy can flow into the core, but not out. Due to the apparent presence of this *horizon*, a definitive direct observation of a BH is very difficult, and before the discovery of gravitational waves, the primary method for observing such objects was indirect via the BH’s gravitational pull on nearby objects. The first indirect evidence for the existence of BHs were made by observing stars that were in binaries with very massive and dark companions, such as the BH CygnusX-1 [261], via measuring the variations of the X-rays produced by the disrupted matter rotating the compact object, the *accretion disc*. More tangible indirect evidence was later obtained by observations of main sequence stars orbiting Sagittarius A\*, the massive compact object of over  $4.1 \pm 0.6 \times 10^6 M_{\odot}$  [128] at the center of the Milky Way galaxy Figure 1.3 [129, 262, 173, 127, 182, 98, 134]. From 1995-2012, the UCLA and Max Plank research teams used the W. M. Keck Observatory to infer the mass of the super massive black hole via measuring the orbits of nearby massive stars (e.g. S0-2 and S-102) (see Figure 1.3).

---

<sup>11</sup>The precise maximum mass limit for neutron stars and the minimum mass limit for black-holes is currently unknown. This ambiguity is referred to as the *mass-gap* [35].

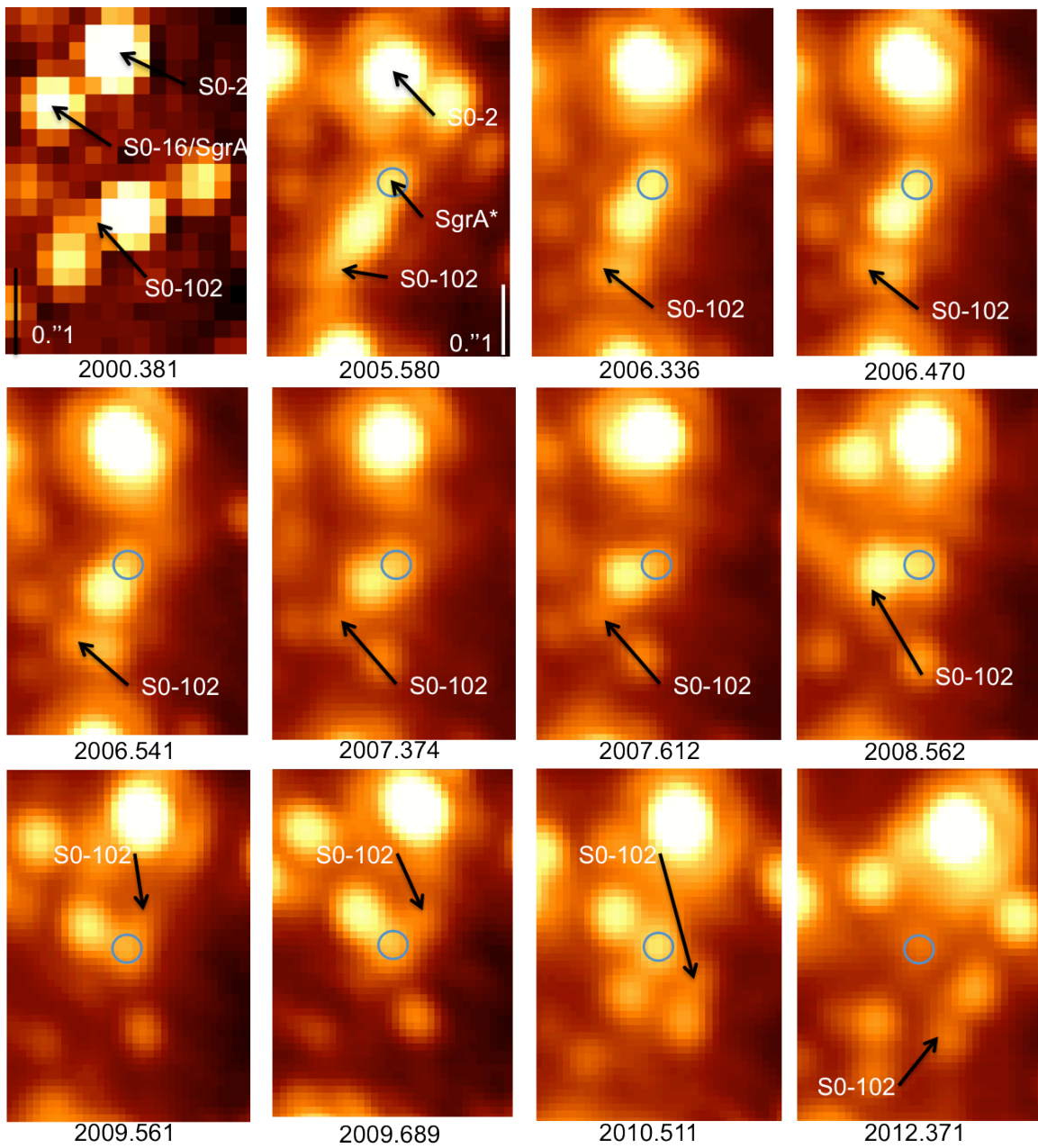


Figure 1.3: Observations by the W. M. Keck Observatory of Sagittarius A\* (the region of weakly illuminated space circled in gray) at the center of our galaxy over the duration of 12 years. The mass of Sagittarius A\* has been estimated to be  $4.02 \pm 0.16 \pm 0.04 \times 10^6 M_{\odot}$  [56], its radius less than  $7.86 \pm 0.14 \pm 0.04$  kpc [56] and its distance from Earth is estimated to be  $7.86 \pm 0.14 \pm 0.04 \pm 0.6$  kpc [56]. These observations confirmed that the stars S0-102 and S0-2 are in orbit (periods  $11.5 \pm 0.3$ [182] and  $15.56 \pm 0.35$  or  $15.92 \pm 0.04$  [56] years respectively) around the more massive compact object Sagittarius A\*. This image is taken from [182, 181].

## 1.1.2 Gravitational waves

In this subsection I walk through a brief history of *Gravitational Waves* (GWs) and the mathematical derivation of a linearized model for gravitational waves, a solution to the linearized Einstein's Field Equation in flat space<sup>12</sup>. These are the signals that we attempt to detect with template banks.

As may be expected, Einstein was a central figure to the development of gravitational waves. What is particularly remarkable about his contribution to field is that he changed his mind several times on the subject. One of the first proposals for the existence was by Oliver Heaviside in 1893, who made a comparison between the inverse square law that governs both gravitational and electromagnetic forces [139]. Henri Poincaré further developed this analogy in 1905 in an article, “Sur la dynamique d’ l’electron” [217], in the ‘Comptes Rendus of the French Academy of Sciences’, which (incorrectly) postulated gravity was transmitted across space in waves in a manner similar to electromagnetic radiation. In 1915, Einstein at first believed that general relativity would support the existence of gravitational waves. However he believed that the wave propagation would be distinct from EM wave propagation in that the waves propagated as ripples in space-time not as transmitted particles [106, 107, 73]. Then in 1916, Einstein made his first reversal on the question of the existence of gravitational waves when he wrote a letter to Karl Schwarzschild stating that he was having doubts of the feasibility of the existence of gravitational waves, due the absence of gravitational dipole radiation in General Relativity [105, 73]. Einstein later changed his mind, and he (with the help of Hermann Weyl) attempted to find a set of coordinates in which he could obtain a wave solution similar (however not identical) to Maxwell’s equations [108, 269].

The three solutions that Einstein formulated used coordinates that were: longitudinal-longitudinal, transverse-longitudinal transverse-traceless. It turns out only one of the coordinates Einstein developed would be valid. In 1922, Eddington wrote an article “The propagation of gravitational waves” [101]. In this article Eddington critiqued Einstein’s solutions, ruling out all but the transverse traceless coordinates as being suitable for describing gravitation waves. The wave solutions obtained in the other two coordinates were deemed to be mathematical artifacts.

This ultimately led to Einstein making another reversal in 1936 when he was collaborating with Nathan Rosen. They came to the conclusion “that gravitational waves do not exist” [110] because they could not find a non-linearized solution in a coordinate systems without a singularity. They attempted to publish the result in Physical Review, however the referee Howard Percy Robertson rejected the paper claiming that Einstein had not rigorously proved that the singularity he found was not just a coordinate singularity and not a property of all possible coordinate systems.

Rather than responding to the comments, Einstein chose to submit the paper to the Journal of the Franklin Society. Einstein would later be convinced by Leopold Infeld that the referee was correct, and Einstein was wrong to assume that the presence of a singularity in his coordinates was indicative that gravitational waves did not exist [73]. Einstein later took a more agnostic stance on the question of the existence of gravitational waves [109]. He submitted a correction (without Rosen’s consent<sup>13</sup>) to his earlier submission to the Franklin society stating that he believed that there were wavelike solutions and they were not just mathematical artifacts. The original version of this paper was accepted and was scheduled to be published, however Einstein submitted his revisions before the original was released.

Central to Einstein’s discomfort with gravitational waves, was how the waveform was ap-

---

<sup>12</sup>Legal disclaimer: “The content and portions of the text presented in this section are taken from [73, 242, 175, 185, 258, 146] with minor paraphrasing. The use of this material is protected under ‘Fair Use’ (UrhG §24,70,63) and consistent with the requirements of § 6 Abs. 1 PromO.”

<sup>13</sup>Rosen was never fully convinced that gravitational waves were a real phenomena.

proximated. Deriving an exact gravitational wave solution in Brinkmann coordinates [61] was key to convincing him that gravitational waves were not just an artifact of the choice of coordinate system. While this exact solution is historically important, for the purposes of this thesis, I will focus on the more tractable linearized version of this theory. The remaining portion of this section is devoted deriving this linearized solution.

So far astrophysical observations of our universe have supported Einstein's Field Equation (Eq. 1.1) as the governing equations of motion for massive bodies in the observable universe

$$R_{\mu\nu} - \frac{1}{2}Rg_{\mu\nu} + \Lambda g_{\mu\nu} = \frac{8\pi G}{c^4}T_{\mu\nu}. \quad (1.1)$$

Eq. 1.1 describes both the motion of matter and energy in *space-time* and how space-time is deformed by matter and energy. Notation is as follows:  $c$  is the speed of light in vacuum,  $g_{\mu\nu}$  is the space-time metric tensor,  $R_{\mu\nu}$  is the Ricci curvature tensor of  $g_{\mu\nu}$ ,  $R = g^{\mu\nu}R_{\mu\nu}$  is the Ricci scalar,  $G$  is Newton's gravitational constant,  $\Lambda$  is the Cosmological constant, and  $T_{\mu\nu}$  is the stress-energy tensor (which obeys the space-time conservation law  $\nabla^\mu T_{\mu\nu} = 0$ )<sup>14</sup>.

For close to flat space-time (ie  $g_{\mu\nu} \rightarrow \eta_{\mu\nu}$ ), there is a solution to Eq. 1.1 that permits for the propagation of small perturbations  $h_{\mu\nu}$ , *Gravitational Waves*, of the Minkowski metric,  $\eta_{\mu\nu}$ ,

$$g_{\mu\nu} = \eta_{\mu\nu} + h_{\mu\nu}. \quad (1.2)$$

A relatively simple expression for these solutions can be derived via a combination of gauge transformations [258]. Space-time metrics are symmetric, which implies that 6 of the 16 components of  $h_{\mu\nu}$  are redundant. Further simplifications to the solution can be made by applying the *the Lorenz gauge* ( $\partial^\nu \bar{h}_{\mu\nu} = 0$ ), where

$$\bar{h}_{\mu\nu} = h_{\mu\nu} - \frac{1}{2}\eta_{\mu\nu}h^\sigma{}_\sigma. \quad (1.3)$$

For the purposes of studying gravitational waves we are primarily interested for the case where the gravitational wave is propagating in space-time outside of the source,  $T_{\mu\nu} = 0$ . This yields a wave solution to Eq. 1.1,

$$(\nabla^2 - \frac{1}{c^2}\partial_0^2)\bar{h}_{\mu\nu} = 0. \quad (1.4)$$

It can be shown [175] that we can do further gauge transforms such that

$$h_\mu{}^{TT} = 0 \quad (1.5)$$

$$h_{0i}{}^{TT} = h_{00}{}^{TT} = 0. \quad (1.6)$$

In this *transverse-traceless gauge* [175]  $\bar{h}_{\mu\nu} = h_{\mu\nu}$  and  $\partial^j h_{ij} = h_i{}^i = 0$ . These plane wave solutions for  $h_{ij}{}^{TT}$  will have the form  $A^{ij} \exp ik_\mu x^\mu$ , where  $k^i = \mathbf{k}$  is the direction of the propagation of the gravitational wave,  $k_0 = \omega/c$  and the components of  $A^{ij}$  are the amplitudes of the gravitational wave. Since  $\partial^j h_{ij}{}^{TT} = 0$ , that implies that the component of  $A_{ij}$  parallel to  $\mathbf{k}$  are zero.

Without loss of generality, we can define  $\hat{\mathbf{k}} = \hat{\mathbf{z}}$ . Thus there are only 4 nonzero components of  $A^{ij}$ , that also satisfy the traceless and symmetric conditions  $h^{TT}{}_i{}^i = 0$  and  $h_{ij}{}^{TT} = h_{ji}{}^{TT}$ . This yields the following solution:

$$h_{ij}{}^{TT}(t, z) = \begin{pmatrix} h_+ & h_\times \\ h_\times & -h_+ \end{pmatrix}_{ij} \exp ik_\mu x^\mu. \quad (1.7)$$

There are only two independent degrees of freedom (the two waveform polarizations  $h_+, h_\times$ ) in this solution.

<sup>14</sup>The greek indicies (e.g.  $\mu, \nu$ ) go from 0 to 3. The latin indicies (e.g.  $i, j$ ) go from 1 to 3.

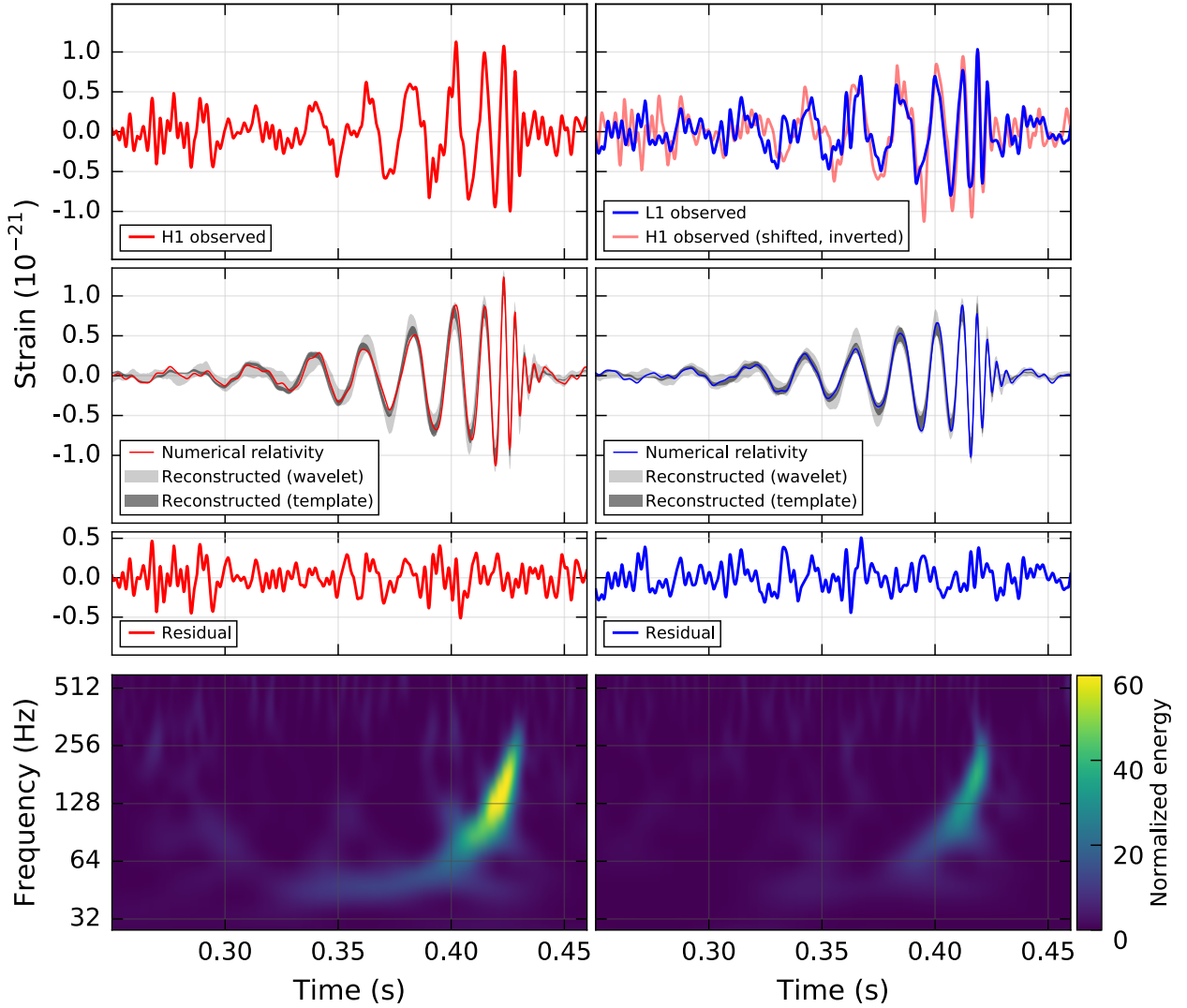


Figure 1.4: GW150914, the first observation of a gravitational wave in the LIGO Hanford (H1) (left column) and Livingston (L1) (right column) detectors likely produced from the merger of two black holes. The horizontal axis denotes time relative to September 14<sup>th</sup>, 2015 09:50:45 UTC. On the first row, the signal first detected at L1 ( $6.9^{+0.5}_{-0.4}$  ms later at H1) are plotted. On the second row, we see how well these signals match the predicted model. Solid lines show a numerical relativity waveform for a CBC system with parameters consistent with those recovered from the detection [68, 189, 18]. The (dark gray) lines indicate the recovered template waveform [20, 18]. The other (light gray) does not use an astrophysical model, but instead calculates the strain signal as a linear combination of sine-Gaussian wavelets [85, 19, 18]. The third row denotes the residuals of the fits in the second panel. In the last row we see a time-frequency representation of the detected “chirp” signal in both detectors [80, 18]. This image and caption are taken from [18] with minor paraphrasing.

## Discovery of gravitational waves

After Einstein was convinced that gravitational waves were a real phenomena, discussions became focused on the feasibility of detecting gravitational waves. In the 1950s, it was unclear how gravitational waves could be detected and subject was considered a bit of a fringe field of research. It eventually attracted the attention of an eccentric American billionaire, Roger W. Babson.

Babson founded the Gravitation Research Foundation [1] as means for paying off the “debt” that he thought he owed Newton’s laws. Babson was an investor, and used a charming interpretation of the principle “What goes up must come down” to time his speculation on stock prices [1, 73]. He had also sought to avenge his sister’s death, who drowned in a well during his childhood, by coming up with a way to control gravity. With the help of fellow financier Agnew Bahson, the physicists John Archibald Wheeler and Bryce DeWitt, the Institute of Field Physics was established in Chapel Hill, North Carolina in 1957 [73].

An inaugural week long conference was held at the new headquarters to investigate “The role of gravitation in Physics” with about 40 invited speakers from 11 countries including Hermann Bondi, Richard “Mr. Smith” Feynman, Joseph Weber and Wheeler [49, 73]. One of the most notable moments of the meeting was a session that Bondi held at this conference to debate if gravitational waves could transmit energy to particles [226]. In this session, Feynman formulated a thought experiment, the “sticky bead argument”, in which he postulated a scenario in which two beads were placed on a bar<sup>15</sup>. In the setup of the experiment, Feynman stated that if the contacts between the beads and the bar are “sticky” (i.e. the system is not frictionless), a gravitational wave that travels orthogonal to the length of the bar will slide the beads against the bar. This results in a transfer of energy from the beads to the bar in the form of friction. This thought experiment was a crucial moment in the development of experiments for detecting gravitational waves because it provided a mechanism in which gravitational wave energy could be converted into a more readily observable form of energy [215].

This thought experiment convinced many other physicists at the conference that gravitational waves could be observable as a physical phenomena and Feynman’s thought experiment is recognized as a seminal moment in the history of the effort to detect gravitational waves [73]. It inspired Joseph Weber [260, 259], Felix Pirani [215, 214] and later Rainer Weiss [265, 266] to construct experiments and instruments in order to detect gravitational waves. The first indirect evidence for the existence of gravitational waves arrived in the 1970s. This evidence was obtained by measuring the periodicity of PSR B1913+16, a pulsar in a binary with a main sequence star [143, 251, 264, 171, 263]. General Relativity predicts that the energy lost from gravitational waves alone will, to leading order, cause the phase of the orbit to decay at a constant rate. When integrated over several orbits, the cumulative shift in the phase will be parabolic (see Figure 1.5). A direct detection of a gravitational wave was only possible by the analysis of data from the LIGO-Virgo *laser interferometers* (see Figure 1.6)[126, 60, 188, 123, 265, 266]<sup>16</sup>.

The laser interferometer gravitational wave detector measures an interference pattern created by bouncing light against mirrors attached to test masses located at the end of its two orthogonal detector arms. Transient deviations in the lengths of the detector arms will result in the two reflected light beams returning to the central beam splitter of the detector with different phases thus altering the interference pattern. One of the primary challenges in constructing these instruments is isolating the mirrored test masses of the detector from non astrophysical noise sources (see search pipeline Section 1.3). By removing these sources of noise it is possible to measure displacements smaller than  $10^{-18}$  m [16] in order to measure gravitational

---

<sup>15</sup>It is worth noting that the experiment is also valid for just one bead.

<sup>16</sup>The design of which was based on enhancements to the original Michelson interferometer of the 1887 experiment by Albert Michelson and Edward Morley which disproved the “ether” theory of the motion of light [183].

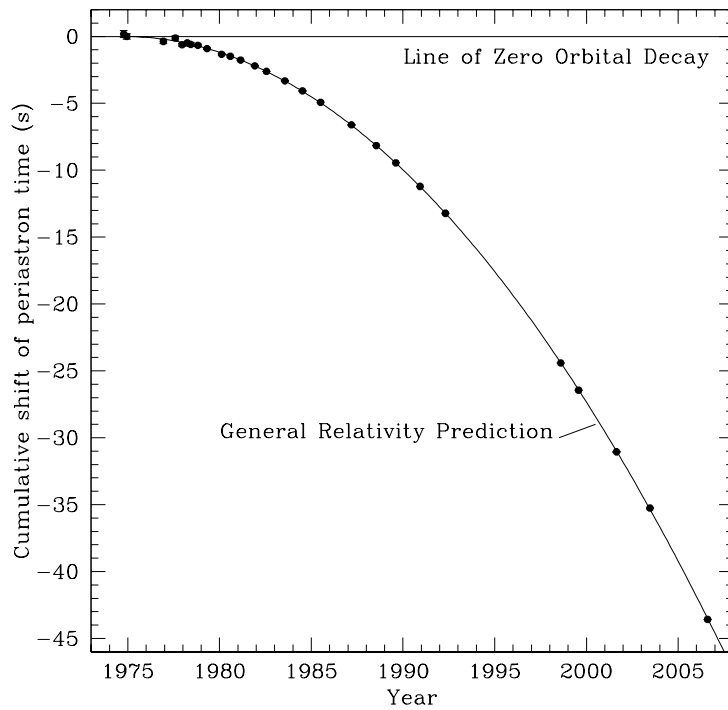


Figure 1.5: Orbital decay in the binary pulsar B1913+16 system demonstrated as an increasing orbital phase shift for periastron over time. The black dots indicate the measurements in the deviation of the cumulative orbital phase. The solid line parabolic line indicates the General Relativity prediction for the decay of the periastron time via the emission of gravitational waves. This image and caption are taken from [171] with minor paraphrasing.

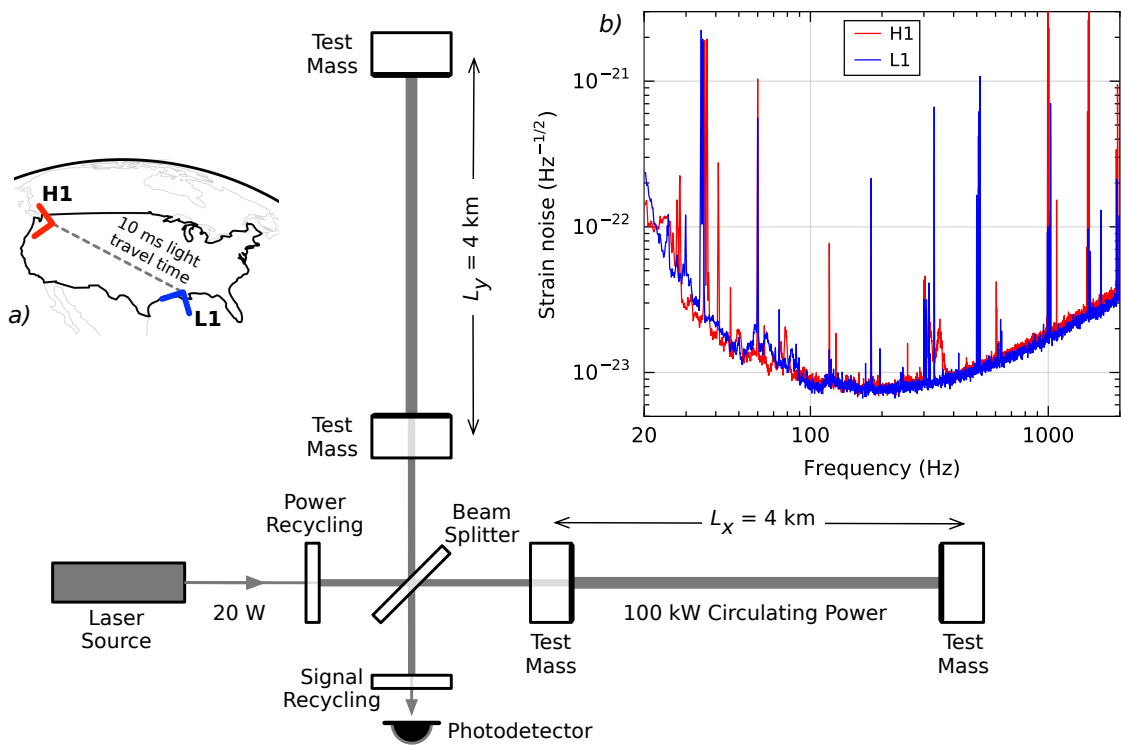


Figure 1.6: a) An illustration of the location of the two LIGO detectors and a simplified diagram of the components of each Michelson interferometer. b) The characteristic sensitivities (i.e. PSDs see Section 1.2) of the two LIGO detectors. This image and caption are taken from [18] with minor paraphrasing.



waves sources in the frequency band 20 Hz-2048 Hz in the first observation run of aLIGO (O1). Gravitational waves travel at light speed and they squeeze and stretch space-time, altering the lengths of the detector arms. If a gravitational wave is observed in multiple detectors, the offset in the observation times allow for the location of the gravitational wave source in the sky to be found.

Different orientations of the detector will make it more/less sensitive to the two linearly independent *waveform polarizations*  $\{h_+, h_\times\}$  (see Eq. 1.7). The detector response functions to these polarizations are denoted by  $F_+(\theta, \phi, \psi)$  and  $F_\times(\theta, \phi, \psi)$  [38],

$$\begin{aligned} F_+(\theta, \phi, \psi) &= \frac{1}{2}(1 + \cos^2 \theta) \cos 2\phi \cos 2\psi - \cos \theta \sin 2\phi \sin 2\psi \\ F_\times(\theta, \phi, \psi) &= \frac{1}{2}(1 + \cos^2 \theta) \cos 2\phi \cos 2\psi + \cos \theta \sin 2\phi \cos 2\psi. \end{aligned} \quad (1.8)$$

They are a function of the sky location of the GW source, determined by the angles  $\{\theta, \phi\}$ , and the polarization angle  $\psi$  (see Eq. 1.38 in Section 1.1.6). When the arms of the detector are both orthogonal to the orbital angular momentum of the CBC GW source, the detector will only be sensitive to the “plus” polarization of the GW waveform,  $h_+$ . Similarly the “cross” polarization of the GW wave will be dominant in the detector if the arms of the detector are orthogonal to an axis that is  $45^\circ$  misaligned with the orbital angular momentum of the binary. If the GW signal is parallel to one of these “plus” or “cross” configurations, it is said to be *linearly polarized*. In contrast, a signal of the form Eq. 1.9 that can be decomposed into an equal linear combination of these two waveform polarizations is *circularly polarized*. In general, the signal seen by the detector  $h(t)$  will be some linear combination of these two polarizations:

$$h(t) = h_+(t)F_+(\theta, \phi, \psi) + h_\times(t)F_\times(\theta, \phi, \psi). \quad (1.9)$$

On September 14<sup>th</sup> 2015 at 09:50:45 UTC, there were two laser interferometers in operation: LIGO-Hanford (H1) located in WA, USA and LIGO-Livingston (L1) located in LA, USA [12]. The signal was first detected by the Livingston detector and  $6.9_{-0.4}^{+0.5}$  ms later in the Hanford detector, a gravitational wave likely produced by the collision of two BHs was observed passing through the Earth.

Since that date, the LIGO-Virgo detectors have found a total of five gravitational waves consistent with binary black hole (BBH) collisions (see Figure 1.7) [18, 17, 22, 23, 24, 14] (and one loud BBH “trigger” LVT151012<sup>17</sup> [see Section 1.3]). In the second observation run (O2), the LIGO-Virgo detectors found a gravitational wave consistent with the collision of two neutron stars (BNS) [25]. What made this GW detection particularly significant was that an additional companion electro-magnetic signal was observed by Fermi X-ray telescope (see Figure 1.8). Over 70 telescopes around the world and in space also found companion signals to the BNS event [21, 26]. This was the first published coincident EM/GW detection. Further solidifying the proof that gravitational waves exist and, more importantly, can be measured.

---

<sup>17</sup>While at the time LVT151012 did officially not meet the detection criteria, when re-examined *ex post facto* in the context of other observations of GWs, it is very likely LVT151012 was a real detection.

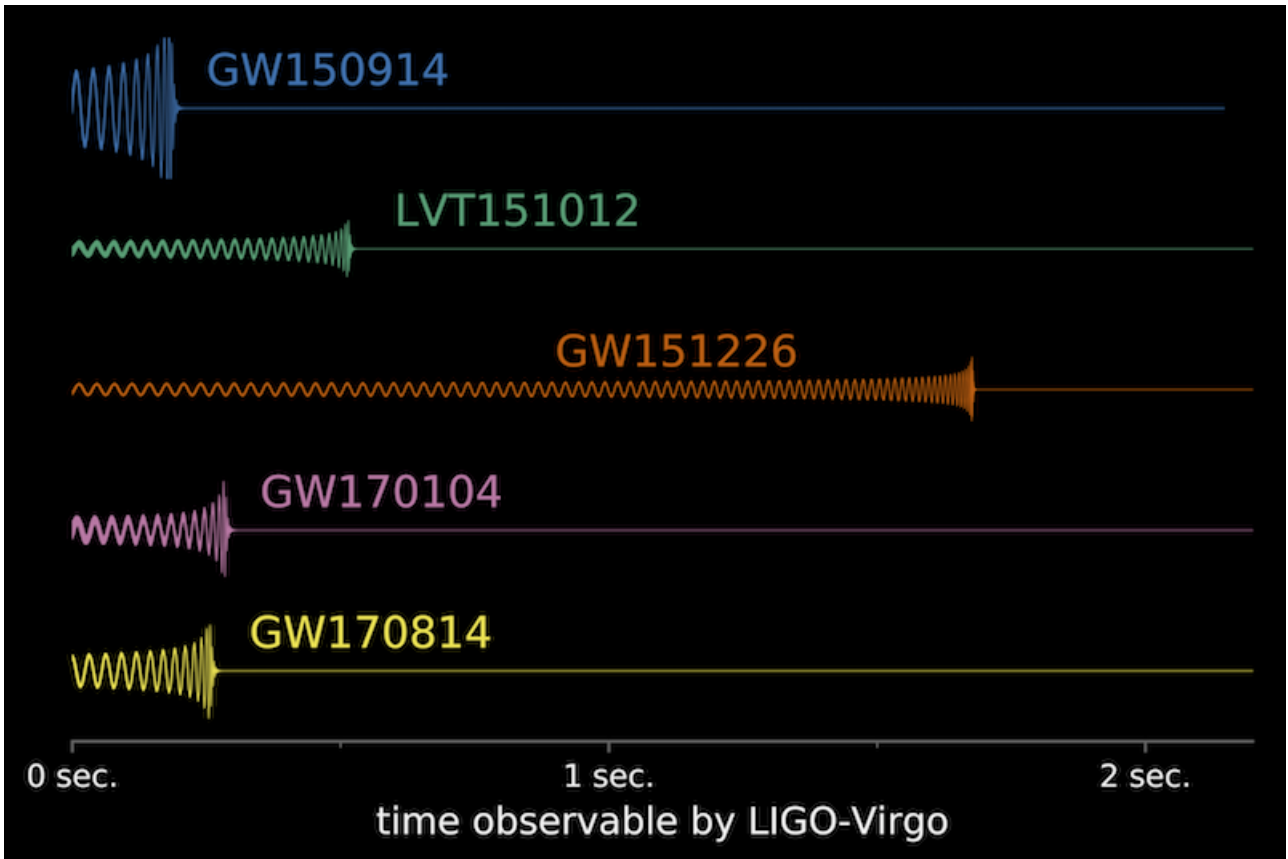


Figure 1.7: A comparison of the time sequences of a selection of observed gravitational waves (with the addition of the GW “trigger” LVT151012 with a significance between  $1.7 - 2.0\sigma$  [14]) in the first two detection eras of LIGO-Virgo. This image is taken from [167] the caption is paraphrased with some augmentation from the same source.

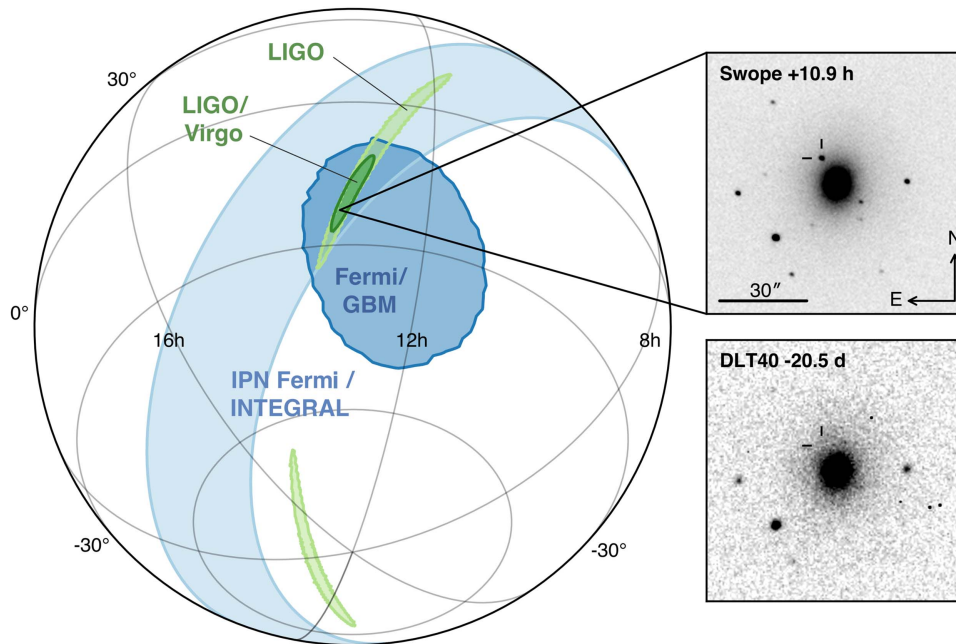


Figure 1.8: The sky location of the first observation of a gravitational wave with a coincident EM signal likely produced by the merger of two neutron stars. The GW signal was triangulated using the LIGO-Virgo gravitational wave detectors. The diagram shows an orthographic projection of the 90% credible regions indicated by the two LIGO detectors (the light green regions), the initial LIGO-Virgo localization (the dark green regions), the *IPN* triangulation determined by comparing the time delay between *Fermi* and *INTEGRAL* (indicated by the light blue region), and the sky location determined from *Fermi*-GBM (indicated in dark blue). The two panels on the right are the 1 meter Swope optical telescope images [86] of galaxy NGC 4993 10.9 hrs after the merger was detected by LIGO-Virgo (top panel) and the DLT40 telescope image [277, 256] of the same region of the sky 20.5 days before the events (bottom panel). The cross-hairs show there is a new luminous object that became visible after the merger. This image is taken from [26] and the caption is copied with minor paraphrasing from the same source.

### 1.1.3 Compact binaries

Binary star systems are very common in the observable universe and are likely the progenitor star systems for CBC systems [158, 144, 142, 161, 159]<sup>18</sup>. In Newtonian physics, these orbits would never decay. In General Relativity, the orbits will decay through emission of gravitational waves (see Section 1.1.2). One poorly understood aspect of the existence of CBC binaries in the observable universe, is how these component masses coalesce. A CBC system with a separation of  $1AU = 1.5 \times 10^{11}$  km would take longer than the age of the universe to decay as a result of GW emission alone. Other mechanisms (e.g. supernova kicks, dynamics within globular clusters, and common mass envelopes) must push the two stars closer together in order for the stars to collide within the Hubble time.

There are three evolutionary scenarios, *channels*, that have been proposed that ensure that the binaries coalesce within the Hubble time: *dynamical formation evolution*, *chemically homogenous evolution*, and *classical isolated binary evolution*. Each channel is distinct in its mechanism to help push the stars closer together.

The dynamical formation channel is a scenario that takes place in star-clusters that are densely populated with compact objects, *globular clusters* [240, 219, 184, 187, 228, 37]. The massive black-holes will be pulled toward the center of the cluster and will form compact binaries with a short enough separation to coalesce on an observable time scale for LIGO. This scenario favors the formation of binary-black-hole systems.

The chemically homogeneous evolution channel has been proposed to describe the evolution of a binary of two massive progenitor stars that are in near contact (period of approximately 2 days) with each other that are on the onset of hydrogen burning [96, 95, 94, 177]. At such close proximity, the tidal forces on the two stars cause the interiors of the two stars to mix and burn hydrogen into helium homogeneously throughout the interiors of the two stars. The stars eventually undergo *type I b/c* supernovas and become black-holes. Assuming that the stellar winds are not sufficient to disrupt the binary, this channel tends to produce two massive black-holes in a close orbit.

The third channel, isolated binary evolution, is often accepted as the “standard” mechanism for CBC formation [254, 150, 220, 221, 48, 250]. This channel is distinct from the other two channels in that it favors the formation of less massive CBC binaries, including *binary-neutron-star* (BNS), *binary-black-hole* (BBH), and *neutron-star-black-hole binaries* (NSBH) systems. The goal of this thesis is to search for BNS and NSBH systems, therefore the remaining portion of this section is devoted to explaining this mechanism for a CBC system consistent to PSR 1913+16 [208, 178] (see Figure 1.5).

In this standard mechanism a *common-mass-envelope* is responsible for pulling the two stars closer together. This scenario starts when two OB stars [231, 246] with at least one component mass  $M_1 \geq 8 - 12M_\odot$  [186, 274, 160, 149, 247] burn the majority of their hydrogen fuel in under 10 Myr. The duration of this hydrogen burning is in proportion to the inverse square of the mass of the star. As a result of the hydrogen burning, the stars form denser helium cores with masses on the order of  $0.1(M/M_\odot)^{1.4}M_\odot$  [254].

Once the more massive of the two stars ceases to fuse hydrogen in its core and its core composition becomes dominated by helium, that star expands beyond its *Roche Lobe* (the region of space where the gravitational force on matter from the companion star is not sufficient to transfer it to the other star [104]). This allows for the mass transfer onto the other star causing the separation between the two stars to decrease and the radius of the other star to grow. This creates a feedback mechanism in which the mass transfer becomes unstable and the the

---

<sup>18</sup>Legal disclaimer “The content and portions of the text presented in this section are taken from [220, 221, 48, 250, 94] with minor paraphrasing. The use of these materials is protected under ‘Fair Use’ (UrHG §24,70,63) and consistent with the requirements of § 6 Abs. 1 PromO.”

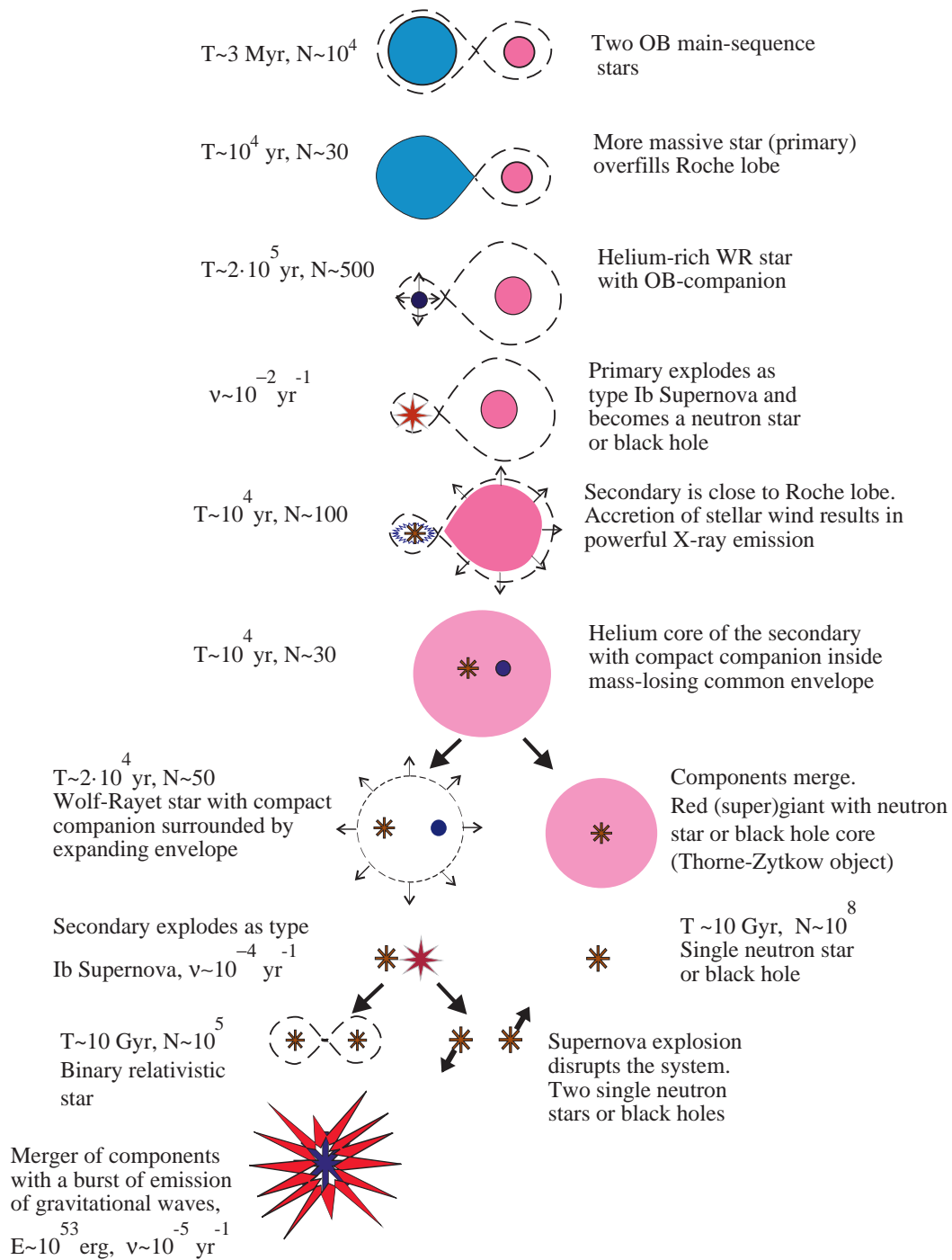


Figure 1.9: A flowchart for the classical isolated binary evolution model for CBC system consistent with PSR 1913+16.  $T$  indicates the approximate time each phase of evolution is expected to take and  $N$  indicates possible population estimates for how many such systems in a given state currently exist in the observable universe [220]. This diagram is taken from [220] and the caption is paraphrased from the same source.

second star can't absorb mass overflow. This overflow of mass envelopes both stars forming the common mass envelope.

This mass exchange lasts on the order of  $10^4$  yrs until most of the outer hydrogen layers of the once more massive star have been shed on to the second star exposing a dense helium core observable as a Wolf-Rayet star [WR] (a star whose structure is disrupted by intense solar winds) if its mass exceeds  $7 - 8M_{\odot}$  [118, 119, 199].

On the order of  $10^5$  yrs, the first star undergoes core fusion of the helium rich core and heavier elements until the stellar core is dominated by the heavier elements of iron and nickel at which the point the radiative pressure of the fusion of elements at the core and the electron degeneracy pressure is insufficient to balance the weight of the outer layers of the star [220]. At this point the first star sheds its less massive outer layers and, depending on its progenitor mass, undergoes an *electron-capture-super-nova* (a *type II super nova*) if  $8M_{\odot} \leq M_1 \leq 12M_{\odot}$ , or an *Fe core collapse* (a *type I b/c*) supernova for  $12M_{\odot} \leq M_1$ . This is a key step in this evolution because it determines whether the the components of the final CBC binary will be black-holes or neutron-stars.

This explosive re-equilibration of the first star lasts on the order of a few days; kicking the remnant NS or BH core and altering the eccentricity of the orbit of the binary. If the binary is still stable after the onslaught of stellar winds produced by the super nova of the first star, the second star will continue to undergo core fusion until it expends its hydrogen core fuel. It will then swell in size exceeding the scope of its Roche Lobe, over the course of  $10^4$  yrs [220]. Eventually the remnant mass of the first star will accumulate enough matter from the second star to form an accretion disc of charged particles capable of the emission of X-rays.

Accretion will continue on the order of  $10^4$  yrs until both the first compact object and the remnant helium rich core of the second mass are embedded within a hydrogen rich common mass envelope [220]. A compact binary will be left if the common-mass-envelope is ejected off the remnant masses<sup>19</sup> and if the second supernova is not strong enough to disrupt the binary. Failure to eject the common-mass-envelope will result in the system ending its evolution as a Thorne-Zytkow object (A star that has a compact object in its core) [252, 253, 47]<sup>20</sup>. This final phase of stellar binary evolution can last up to 10 Gyr [220], as the compact objects *inspiral* into one another as energy is lost due to the emission of gravitational waves.

As a result of the kick to the component masses from the second supernova, it is possible for the individual objects to have angular momenta, *spins*, that are not aligned with the orbital angular momentum of the system. The higher the aligned component of the spin in the direction of the orbital angular momentum of the orbit, the longer it will take for the orbit to decay. The greater the anti-aligned component of the spin with respect to the orbital angular momentum, the shorter the time it takes for the orbit to decay. The greater the perpendicular component of the spins relative to the orbital angular momentum of the binary, the more the binary will *precess* as the objects inspiral one another. Precession will be discussed in detail in Section 1.1.6. Precession has a tendency to heavily modulate the gravitational wave signal of CBC. Searches for gravitational waves produced from precessing CBC systems poses a problem for template bank construction as it requires many more templates than non-precessing and non-spinning searches (see Chapter 3).

Eventually the orbit of the compact objects will decay to the *Innermost-Stable-Circular-Orbit* (ISCO). If the orbit decays further, the orbit will no longer be quasi-stable, and the compact objects will *plunge* into one another (this portion of the evolution is called the *late-*

<sup>19</sup>The mechanism in which the common-mass-envelope is ejected is currently unknown [252, 253, 47].

<sup>20</sup>Observational confirmation of Thorne-Zytkow objects is currently unclear. The problem is that these objects would look nearly identical to late stage main-sequence or super giant stars when observed outside of the structure of the star via EM emissions. HV 2112 is believed to be a strong Thorne-Zytkow object candidate due to its abundance of heavy elements in its EM emission lines [166].

*inspiral*). At the end of the plunge the two objects will violently *merge* together into one massive object, releasing on the order of  $10^{46}$  Joules or higher [81, 82, 220] in the form of gravitational waves within an order of a minutes (up to fractions of second for more massive BBH systems) followed by a *gamma-ray-burst* (GRB) up to a few hours later after merger if at least one of the component masses is a neutron-star. If the remaining single compact object is over the TOV limit (see footnote in Section 1.1.1), it becomes a BH. During the merger the object will have an asymmetric surface/event horizon maintaining a significant mass quadrupole and will continue to emit gravitational waves. As the system undergoes *ringdown*, the last phase of GW emission, the space time around the final mass approaches the Kerr solution and GWs are emitted which can be modeled as perturbations of the Kerr metric.

As I will show in Section 1.1.4, modeling CBC evolution after inspiral poses a computational challenges since there are currently no accurate analytic solutions for these later parts of the waveform. As will be discussed in Chapter 4, this poses problems for template bank construction for searches since there is no mismatch metric for template placement of inspiral-merger-ringdown waveforms (see Section 1.1.4).

### 1.1.4 Waveform models

As outlined in the previous section, the evolution of a CBC gravitational waveform signal is classified into four portions: inspiral, late-inspiral, merger, and ringdown<sup>21</sup>. The inspiral portion of the waveform is most critical for constructing BNS template banks. The other portions are more important for constructing heavier mass NSBH and BBH template banks. In general, obtaining an analytic expression for the entire evolution of these waveforms is not currently possible, and one must apply additional approximations and numerical methods to use them in a way that is computationally efficient.

For the purposes of modeling *inspiral-only* gravitational wave models, the post-Newtonian (PN) formalism provides a reasonable approximation to the observed gravitational waveform. There are a variety of PN approximants available which differ in how one deals with the energy, flux and balance equations [64]. For this first phase of CBC evolution, most approximants should give similar results and the main consideration is computational efficiency.

For non-precessing systems, currently several waveform approximant models exist that each have their own way of approximating the underlying CBC dynamics. All these waveform models presented in this section use the *adiabatic approximation*: the condition that the orbit decays slowly during the inspiral such that the fractional change in orbital frequency,  $F_{orb}$ , is negligible (i.e.  $\dot{F}_{orb}/F_{orb}^2 \ll 1$ ) for the majority of the GW signal. The GW phase is fixed to be twice the orbital phase,  $\phi(t)$ , the waveform to leading PN order. These approximations will be accurate up until around the system reaches its ISCO,  $f_{ISCO} = (6^{3/2}\pi M)^{-1}$  [258]<sup>22</sup>. Frequencies beyond this threshold enter the late-inspiral portion of the waveform, in which the adiabatic approximation fails. Exploiting these approximations and Kepler’s law yields the following expression for orbital velocity,

$$v(t) = (\pi M f(t))^{1/3}. \quad (1.10)$$

Now it is possible to define a system of differential equations describing the evolution of the orbital phase and velocity,

$$\dot{\phi}(t) = v^3/M$$

---

<sup>21</sup>Legal disclaimer: “Some of the content and portions of the text presented in this section are taken from [64, 32, 57, 92, 93, 97, 50, 146] with minor paraphrasing. The use of these materials is protected under ‘Fair Use’ (UrhG §24,70,63) and consistent with the requirements of § 6 Abs. 1 PromO.”

<sup>22</sup>This orbit is the innermost stable circular orbit for test particles orbiting a Schwarzschild black-hole. It is only an approximation for systems with spinning black-holes.

$$\dot{v}(t) = -\mathcal{F}(v)/\partial_v\mathcal{E}(v). \quad (1.11)$$

Here  $\mathcal{F}(v)$  is the *gravitational-wave luminosity* and  $\mathcal{E}(v)$  is the *binding energy* of the CBC system as a function of orbital velocity. It can be shown that the gravitational wave luminosity and binding energy can be expanded expressed as follows via a *post-Newtonian* (PN) approximation, that assumes that the *orbital velocity*,  $v = (\pi M f)^{1/3}$ , of the CBC system is much smaller than the speed of light<sup>23</sup>,

$$\begin{aligned} E_3(v) &= -\frac{1}{2}\eta v^2 \left[ 1 - \left( \frac{3}{4} + \frac{1}{12}\eta \right) v^2 - \left( \frac{27}{8} - \frac{19}{8}\eta + \frac{1}{24}\eta^2 \right) v^4 \right. \\ &\quad \left. - \left\{ \frac{675}{64} - \left( \frac{34445}{576} - \frac{205}{96}\pi^2 \right) \eta + \frac{155}{96}\eta^2 + \frac{35}{5184}\eta^3 \right\} v^6 \right], \\ \mathcal{F}_{3.5}(v) &= \frac{32}{5}\eta^2 v^{10} \left[ 1 - \left( \frac{1247}{336} + \frac{35}{12}\eta \right) v^2 + 4\pi v^3 \right. \\ &\quad - \left( \frac{44711}{9072} - \frac{9271}{504}\eta - \frac{65}{18}\eta^2 \right) v^4 - \left( \frac{8191}{672} + \frac{583}{24}\eta \right) \pi v^5 \\ &\quad + \left\{ \frac{6643739519}{69854400} + \frac{16}{3}\pi^2 - \frac{1712}{105}\gamma + \left( \frac{41}{48}\pi^2 - \frac{134543}{7776} \right) \eta \right. \\ &\quad \left. - \frac{94403}{3024}\eta^2 - \frac{775}{324}\eta^3 - \frac{856}{105}\log(16v^2) \right\} v^6 \\ &\quad \left. - \left( \frac{16285}{504} - \frac{214745}{1728}\eta - \frac{193385}{3024}\eta^2 \right) \pi v^7 \right]. \end{aligned} \quad (1.12)$$

The principle difference between the **TaylorT2** and the **TaylorF2** models is how they approximate the ratio  $\mathcal{F}(v)/\partial_v\mathcal{E}(v)$ . For this thesis, the **TaylorT2**, **TaylorF2** and **IMRPhenomD** and **IMRPhenomP** models were primarily used and are the focus of this section.

The **TaylorT2** model [55, 54, 271, 72, 13, 92, 93, 53] uses a finite integral solution to Eqs. 1.11. It expands the ratio of polynomials  $\mathcal{F}(v)/\partial_v\mathcal{E}(v)$  to consistent PN order, integrates the differential equations, and extracts a set of parametric equations for  $\phi(v)$  and  $t(v)$ . For the purposes of describing this methodology, I will focus on the non-spinning systems. We start with the following systems of equations:

$$\phi_{n/2}^{(T2)}(v) = \phi_{\text{ref}}^{(T2)} + \phi_N^v(v) \sum_{k=0}^n \hat{\phi}_k^v v^k, \quad (1.13)$$

$$t_{n/2}^{(T2)}(v) = t_{\text{ref}}^{(T2)} + t_N^v(v) \sum_{k=0}^n \hat{t}_k^v v^k. \quad (1.14)$$

Solving Eqs. 1.13 and 1.14 is computationally inefficient and after requires solving a set of transcendental equations. It can be shown that the following is the solution for  $n/2 = 3.5$ ,

$$\begin{aligned} \phi_{3.5}^{(T2)}(v) &= \phi_{\text{ref}}^{(T2)} - \frac{1}{32\eta v^5} \left[ 1 + \left( \frac{3715}{1008} + \frac{55}{12}\eta \right) v^2 \right. \\ &\quad \left. - 10\pi v^3 \left( \frac{15293365}{1016064} + \frac{27145}{1008}\eta - \frac{3085}{144}\eta^2 \right) v^4 \right. \\ &\quad \left. + \left( \frac{38645}{672} - \frac{65}{8}\eta \right) \log\left(\frac{v}{v_{\text{ISCO}}}\right) \pi v^5 + \left\{ \frac{12348611926451}{18776862720} - \frac{160}{3}\pi^2 - \frac{1712}{21}\gamma \right. \right. \end{aligned} \quad (1.15)$$

---

<sup>23</sup>The energy is expanded to 3 PN order and the power flux is expanded to 3.5 PN order [64].  $\gamma$  denotes the Euler constant.



$$\begin{aligned}
& + \left( \frac{2255}{48} \pi^2 - \frac{15737765635}{12192768} \right) \eta \\
& + \frac{76055}{6912} \eta^2 - \frac{127825}{5184} \eta^3 - \frac{856}{21} \log(16v^2) \} v^6 \\
& + \left( \frac{77096675}{2032128} + \frac{378515}{12096} \eta - \frac{74045}{6048} \eta^2 \right) \pi v^7 \Big] \\
t_{3.5}^{(\text{T2})} = & t_{\text{ref}}^{\text{T2}} - \frac{5M}{256\eta v^8} \left[ 1 + \left( \frac{743}{252} + \frac{11}{3} \eta \right) v^2 - \frac{32}{5} \pi v^3 + \left( \frac{3058673}{508032} + \frac{5429}{504} \eta + \frac{617}{72} \eta^2 \right) v^4 \right. \\
& - \left( \frac{7729}{252} - \frac{13}{3} \eta \right) \pi v^5 + \left\{ -\frac{10052469856691}{23471078400} + \frac{128}{3} \pi^2 + \frac{6848}{105} \gamma \right. \\
& + \left( \frac{3147553127}{3048192} - \frac{451}{12} \pi^2 \right) \eta - \frac{15211}{1728} \eta^2 + \frac{25565}{1296} \eta^3 + \frac{3424}{105} \log(16v^2) \Big\} v^6 \\
& \left. + \left( -\frac{15419335}{127008} - \frac{75703}{756} \eta + \frac{14809}{378} \eta^2 \right) \pi v^7 \right]. \tag{1.16}
\end{aligned}$$

The **TaylorF2** model is a computationally efficient, frequency-domain waveform model that utilizes the *Stationary-Phase-Approximation* (SPA) [97]. This approximation utilizes the idea that the main contribution to the Fourier integral (which is computed to calculate the frequency domain waveform) is from the region where the waveform phase is stationary. Therefore, since the majority of the GW signal exists in the low frequency range, most of the power associated with the signal is focused in that region of the frequency spectrum.

The **TaylorF2** waveform used in this thesis describes aligned spin systems with spins on the component objects  $\{\mathbf{S}_1, \mathbf{S}_2\}$  (total spin  $\mathbf{S} = \mathbf{S}_1 + \mathbf{S}_2$ ). This waveform can be decomposed into terms that are dependent on the extrinsic *angles* associated with the observation of the waveform (e.g. sky position, polarization and orientation), the distance  $D$  from the observer to the GW source, the ‘‘chirp mass’’ of the system (see Eq. 1.22),  $\mathcal{M}$ , and most importantly the GW phase  $\Phi(f)$ .

$$\tilde{h}(f) = \frac{1}{D} \mathcal{M}^{5/6} Q(\text{angles}) f^{-7/6} \exp i\Psi(f) \tag{1.17}$$

The phase of the waveform,  $\Psi(f)$ , can be calculated to 3.5 PN order with respect to a reference frequency,  $f_0$ , and the *spin-orbit* parameter  $\beta_C$  (see Eq. 1.28), and the PN coefficients  $\lambda_i^{(\text{F2})}$ ,

$$\begin{aligned}
\Psi_{3.5}^{(\text{F2})}(f) = & 2\pi f_0 \frac{f}{f_0} - \phi_C + \lambda_0^{(\text{F2})} \left( \frac{f}{f_0} \right)^{-5/3} + \lambda_2^{(\text{F2})} \left( \frac{f}{f_0} \right)^{-1} + \lambda_3^{(\text{F2})} \left( \frac{f}{f_0} \right)^{-2/3} + \lambda_4^{(\text{F2})} \left( \frac{f}{f_0} \right)^{-1/3} \\
& + \lambda_{5L}^{(\text{F2})} \log \left( \frac{f}{f_0} \right) + \lambda_6^{(\text{F2})} \left( \frac{f}{f_0} \right)^{1/3} + \lambda_{6L}^{(\text{F2})} \log \left( \frac{f}{f_0} \right) \left( \frac{f}{f_0} \right)^{1/3} + \lambda_7^{(\text{F2})} \left( \frac{f}{f_0} \right)^{2/3} \tag{1.18}
\end{aligned}$$

$$\begin{aligned}
\lambda_0^{(\text{F2})} &= \frac{3}{128} (\pi \mathcal{M} f_0)^{-5/3} \\
\lambda_2^{(\text{F2})} &= \frac{5}{96 \eta^{2/5}} \left( \frac{743}{336} + \frac{11}{4} \eta \right) (\pi \mathcal{M} f_0)^{-1} \\
\lambda_3^{(\text{F2})} &= -\frac{3\pi}{8 \eta^{3/5}} \left( 1 - \frac{1}{4\pi} \beta_C \right) (\pi \mathcal{M} f_0)^{-2/3} \\
\lambda_4^{(\text{F2})} &= \frac{15}{64 \eta^{4/5}} \left( \frac{3058673}{1016064} + \frac{5429}{1008} \eta + \frac{617}{144} \eta^2 - \sigma \right) (\pi \mathcal{M} f_0)^{-1/3} \\
\lambda_{5L}^{(\text{F2})} &= \frac{3}{128 \eta} \left( \frac{38645\pi}{756} - \frac{65\pi}{9} \eta \right)
\end{aligned}$$

$$\begin{aligned}
\lambda_6^{(\text{F2})} &= \frac{3}{128\eta^{6/5}} \left[ \frac{11583231236531}{4694215680} - \frac{640\pi^2}{3} - \frac{6848}{21} \left( \gamma + \log 4 - \frac{1}{5} \log \eta + \frac{1}{3} \log(\pi \mathcal{M} f_0) \right) \right. \\
&\quad \left. - \frac{15737765635}{3048192} \eta + \frac{2255\pi^2}{12} \eta + \frac{76055}{1728} \eta^2 - \frac{127825}{1296} \eta^3 \right] (\pi \mathcal{M} f_0)^{1/3} \\
\lambda_{6L}^{(\text{F2})} &= -\frac{1}{128\eta^{6/5}} \frac{6848}{21} (\pi \mathcal{M} f_0)^{1/3} \\
\lambda_7^{(\text{F2})} &= \frac{3}{128\eta^{7/5}} \left( \frac{77096675\pi}{254016} + \frac{378515\pi}{1512} \eta + \frac{74045\pi}{756} \eta^2 \right) (\pi \mathcal{M} f_0)^{2/3}. \tag{1.19}
\end{aligned}$$

A family of inspiral-merger-ringdown waveform models that make a particularly efficient use of computation time (without compromising accuracy) are the *inspiral-merger-ringdown-Phenomenological* **IMRPhenom** family of models [32, 232, 234, 135, 155]. These models are not exact solutions to Einstein’s equations. They use a combination of analytic models for the inspiral and ringdown portions of the waveform and *phenomenological* frequency domain parametrized fits of numerical simulations of Einstein’s equations to determine the late-inspiral and merger portions of the waveform. They also simplify how the spins on the component masses are considered, reducing the mass and spin of the CBC system as one *effective mass*,  $M = M_1 + M_2$ , and an *effective spin*,  $\chi_{eff}$ ,

$$\chi_{eff} = \frac{\chi_1 + \chi_2}{2} + \frac{M_1 M_2}{M^2} \frac{\chi_1 - \chi_2}{2}. \tag{1.20}$$

While the individual components that are parametrized in these fits are constructed *ad hoc*, linear combinations of these terms have been shown to accurately approximate numerical solutions to Einstein’s equations [32, 232, 234, 135, 155]. For the inspiral portion of the waveform, either the **TaylorF2** or **SpinTaylorF2** (see Section 1.1.6) models are used depending if the CBC systems being modeled are aligned-spin or precessing respectively. The solutions for the ringdown portion of the waveform can be modeled analytically by perturbing the space-time around the event horizon of a Kerr black-hole [50]. These ringdown models are dependent on the final mass and spin of the final merged compact object; they must be determined by conducting numerical simulations of Einstein’s equations.

While the numerical simulations of Einstein’s equations are used to determine both the coefficients for the late-inspiral and merger portion and the mass and spin of the final object needed for the ringdown portion of the waveform, these simulations do not have to be repeated every time an **IMRPhenom** model is evoked. Rather, a database is constructed once, containing all the prerequisite fit parameters and final masses and spins of the range of possible final merged objects. Due to their *ad hoc* formulation, these waveforms are not true solutions of Einstein’s equations and are only valid to the extent they are faithful to numerical simulations.

### 1.1.5 Chirp time

The choice of coordinates will greatly ease the construction of a template bank (as will further be discussed in Chapters 2,3,4 and 5)<sup>24</sup>. As is often the case, component masses and spins are not the best coordinates for placing templates. While inspiral-only gravitational waveforms use these intrinsic parameters, as shown in the previous section, these waveforms are constructed via PN expansions. The so called “chirp times”, to leading PN order, approximate the duration of the CBC inspiral in seconds. Hence the motivation for using a chirp time coordinate space to better describe these waveforms.

As can be seen in the previous section, it is often useful to expand the general expression for the gravitational waveform in terms of corrections to a low-velocity Newtonian limit (see Section 1.1.4). There are many different ways to expand the gravitational waveform in this limit, however the key conditions for all these expansions is that the source orbital velocity is non-relativistic  $v/c \ll 1$  and that the distance,  $d$ , to the source is sufficiently far away from the observer. For the purposes of this thesis I also use the approximation that the orbits are *quasi-circular*<sup>25</sup>. The differential orbital energy of such CBC systems can be generalized as

$$\frac{dE}{dt} = \frac{c^3 r^2}{32\pi G} \int d\Omega \langle \dot{h}_{ij}^{TT} \dot{h}_{ij}^{TT} \rangle. \quad (1.21)$$

The post-Newtonian (PN) terms used in this thesis are constructed by expanding  $h^{TT}(f(t))$  in terms of powers of the orbital velocity of the component masses  $v/c$  at some orbital frequency  $f(t)$  observed at some time  $t$ . For the purposes of this expansion, it is assumed that the PN corrections to the waveforms amplitude are ignored and the gravitational waveform can be re-expressed in terms of the waveform’s phase,  $\Phi(t) = \int 2\pi dt f(t)$  (see Eq. 1.17). It is notationally advantageous when calculating these “chirp time” coordinates to define the “chirp mass”,  $\mathcal{M}$ , the mass ratios  $q, \nu$ , and the dimensionless mass ratio,  $\eta$ , all calculated from the CBC component masses,  $M_1, M_2$ ,

$$\begin{aligned} q &= M_1/M_2 \\ \nu &= M_1/M \\ \eta &= \frac{M_1 M_2}{M^2} \\ \mathcal{M} &= \eta^{\frac{3}{5}} M. \end{aligned} \quad (1.22)$$

When only considering the leading order term in Eq. 1.21, it can be shown that the total power radiated as a function of the orbital frequency,  $\omega$ , to leading order in  $v$  is as follows.

$$\frac{dE}{dt} = \frac{32c^5}{5G} \left( \frac{G\mathcal{M}\omega}{2c^3} \right)^{10/3} \quad (1.23)$$

As was seen in Figure 1.5, the periastron of the Hulse-Taylor Binary shifts parabolically with time. This is a consequence of the decay of the orbit due to energy being radiated from the system in the form of gravitational radiation. Since the source for the total radiated energy of a binary in a fixed *quasi-circular* Keplerian orbit is equal to the sum of the kinetic and potential energy of the system. Assuming that the component masses are moving at speed well under the speed of light we obtain the following equation:

<sup>24</sup>Legal disclaimer: “The content and portions of the text presented in this section are taken from [175, 218, 152, 51, 64, 237, 233, 88, 171, 146] with minor paraphrasing. The use of these materials are protected under ‘Fair Use’ (UrhG §24,70,63) and consistent with the requirements of § 6 Abs. 1 PromO.”

<sup>25</sup>Corrections to this assumption are expected to be small. For example, for elliptic orbits it can be shown that the ellipticity of the orbit will decrease at a faster rate than the orbital decay rate of the CBC system [213].

$$E_{\text{orbital}} = E_{\text{kinetic}} + E_{\text{potential}} = -\frac{GM_1M_2}{2R} = -\left(G^2\mathcal{M}^5\omega^2/32\right)^{1/3}. \quad (1.24)$$

As a CBC binary emits GWs,  $E_{\text{orbital}}$  becomes increasingly negative causing the radius of the orbit,  $R$ , to decrease. As a consequence of Kepler's law, the orbital frequency,  $\omega$ , is proportional to  $R^{-2/3}$ . Therefore as the orbit decays, the system rotates faster. In the adiabatic approximation we see that the right hand side of Eq. 1.23 does not change with time. Therefore when calculating the cumulative shift in the periastron of the binary, integrating this power loss yields the characteristic parabolic curve in Figure 1.5.

The adiabatic approximation also allows for the following relation between the orbital and GW angular frequencies  $\omega_{\text{GW}} = 2\omega$ . Utilizing this substitution and combining Eqs 1.23 and 1.24 yields the following differential equation for the evolution of the angular frequency of the GW as a function of time,

$$\dot{\omega}_{\text{GW}} = \frac{12}{5}2^{1/3}\left(\frac{GM}{c^3}\right)^{5/3}(\omega_{\text{GW}})^{11/3}. \quad (1.25)$$

Exploiting that  $\omega_{\text{GW}} = 2\pi f$ , and integrating Eq 1.25 yields the following relationship between gravitational wave frequency and the time it takes for the system to coalesce, the zeroth order ‘‘chirp time’’  $\tau_0 = t_c - t$ ,

$$f(\tau_0) = \frac{1}{\pi}\left(\frac{GM}{c^3}\right)\left(\frac{5}{256\tau_0}\right)^{3/8}. \quad (1.26)$$

We can repeat this derivation with higher order PN corrections to the phase.

Expanding the time derivative of the orbital frequency yields the following expression:

$$\begin{aligned} \frac{\partial f}{\partial t} = \frac{96}{5\pi\mathcal{M}^2}v^{11} & \left\{ 1 - \left(\frac{743}{336} + \frac{11}{4}\eta\right)v^2 + (4\pi - \beta_C)v^3 \right. \\ & \left. + \left(\frac{34103}{18144} + \frac{13661}{2016}\eta + \frac{59}{18}\eta^2 + \sigma\right)v^4 + \dots \right\}. \end{aligned} \quad (1.27)$$

$\beta_C$  is the *spin-orbit* parameter,  $\mathbf{L}$  is the orbital angular momentum,  $\{\mathbf{S}_i\}$  are the two spins of the component masses of the CBC system and  $\{\chi_i\} = \{\chi_1, \chi_2\} = \left\{\frac{\mathbf{S}_i}{M_i^2}\right\}$  are the dimensionless spins of the two component masses<sup>26</sup>,

$$\beta_C = \frac{1}{12}\sum_i(113(M_i/M)^2 + 75\eta)\hat{\mathbf{L}} \cdot \chi_i. \quad (1.28)$$

$\sigma$  is the spin-spin parameter,

$$\sigma = \frac{\eta}{48}(-247\chi_1 \cdot \chi_2 + 721\hat{\mathbf{L}} \cdot \chi_1\hat{\mathbf{L}} \cdot \chi_2). \quad (1.29)$$

For the purposes of this thesis I am primarily interested in modeling NSBH systems (see Chapters 3 and 4). Since NS spins are expected to be small relative to BH spin [171], I only consider CBC systems with spin on the first component mass. With this in mind, the phase of the waveform is solved as a function of the frequency of the coalescence,  $f$ , the *intrinsic* parameters of the CBC system  $\theta = \{M_1, M_2, \chi_1\}$  relative to some reference frequency  $f_0$ ,  $\phi_C$  is the coalescence phase when  $f \rightarrow \infty$  and a coalescence time,  $t_C$ , for the merging of the compact

<sup>26</sup>For neutron-stars and Kerr black-holes  $|\mathbf{S}_i| < M_i^2$  [154, 193, 192].

objects<sup>27</sup>. The accumulated phase of the gravitational waveform,  $\Phi(f; \theta, f_0)$ , can be expanded in the following form [175],

$$\begin{aligned} \Phi(f; \theta, f_0) = & \frac{16\pi f_0 \tau_0(\theta, f_0)}{5} \left\{ \left( 1 - \left( \frac{f}{f_0} \right)^{-5/3} \right) + \frac{5}{4} \frac{\tau_2(\theta, f_0)}{\tau_0(\theta, f_0)} \left( 1 - \left( \frac{f}{f_0} \right)^{-1} \right) \right. \\ & \left. - \frac{25}{16} \frac{\tau_3(\theta, f_0)}{\tau_0(\theta, f_0)} \left( 1 - \left( \frac{f}{f_0} \right)^{-2/3} \right) + \dots \right\}. \end{aligned} \quad (1.30)$$

Eq. 1.30 yields three chirp time coordinates  $\{\tau_0, \tau_2, \tau_3\}$  [218, 152, 51, 64, 237, 233, 175] which have been demonstrated to flatten out the **TaylorF2** template bank [88]. These additional chirp times are used to approximate the duration of the “chirp” signal in seconds to higher order in starting from from some reference frequency  $f_0$ . The subscript for the chirp time coordinates are defined to be twice the PN order of the correction to the GW phase  $\Phi$ . Thus the  $\tau_2$  chirp time is the coefficient for the 1 PN order expansion in Eq. 1.27; the coefficient of  $v^2 = (\pi M f)^{2/3}$ . Therefore Eqs. 1.30, 1.27 lack  $\tau_1$  terms, because the original PN expansion lacks a 0.5 PN coefficient (i.e.  $v^1 = (\pi M f)^{1/3}$  does not appear in the expansion). These first three non-zero chirp times are calculated in the following way,

$$\begin{aligned} \tau_0 &= \frac{5}{256} \frac{(\pi f_0)^{-8/3} (M_1 + M_2)^{1/3}}{M_1 M_2}, \\ \tau_2 &= \frac{5}{256} \frac{M_1 + M_2}{M_1 M_2} (\pi f_0)^{-8/3} \left( \frac{743}{336} + \frac{11}{4} \frac{M_1 M_2}{(M_1 + M_2)^2} \right), \\ \tau_3 &= \frac{(\pi f_0)^{-5/3}}{128} (M_1 + M_2)^{32/15} (M_1 M_2)^{-7/5} \\ &\times \left( 16\pi - \frac{\chi_1}{6} \left( \frac{19 M_1 M_2}{(M_1 + M_2)^2} + \frac{113 M_1}{M_1 + M_2} + 94 \right) \right). \end{aligned} \quad (1.31)$$

---

<sup>27</sup>This is only valid for PN inspiral waveforms. In the IMRPhenom models this cutoff is handled differently since the frequency does not become infinite at the end of inspiral.

### 1.1.6 Precessing NSBH waveform derivation

The **SpinTaylorF2** model [174] is a variant of the **TaylorF2** model that includes extra degrees of freedom in order to describe *precessing* CBC systems<sup>28</sup>. To leading PN order, the inspiral portion of the waveform is independent of the properties of the interiors of the neutron-star or black-hole. It can be modeled analytically or numerically by using the masses and spins of the compact objects and the orientation of their orbit beyond ISCO. The later parts of the waveform evolution are currently modeled numerically and are highly dependent on the compositions and hydro-magnetic dynamics inside the objects. In this section I give a detailed explanation of this waveform model.

Precessing CBC systems waveforms can be represented in the CBC source frame,  $\tilde{h}$ ; a frame whose vertical axis is parallel with the initial orientation of the the total angular momentum  $\mathbf{J} = \mathbf{L} + \sum_i \mathbf{S}_i = \mathbf{L} + \mathbf{S}$ . The orientation of the orbital angular momentum,  $\mathbf{L}$ , will vary with time for precessing systems. However the orientation of the total angular momentum  $\{\theta_{\mathbf{J}}, \phi_{\mathbf{J}}\}$  of the binary is approximately constant for most scenarios [63]<sup>29</sup>. This setup allows for the waveform to be expressed as a sum of products of orthogonal *spherical harmonics*,  $Y_{l,m}^{-2}(\theta_{\mathbf{J}}, \phi_{\mathbf{J}})$ <sup>30</sup>, and their associated time dependent *modes*,  $\tilde{h}^{l,m'}(t)$  [40] that have characteristic time dependent phase,  $\phi_{l,m}(t) \approx m\Phi_{\text{orbit}}$ , and amplitude,  $\mathcal{A}_{l,m}(t)$ ,

$$\tilde{h}(t) = \sum_{l,m} Y_{l,m}^{-2}(\theta_{\mathbf{J}}, \phi_{\mathbf{J}}) \tilde{h}^{l,m}(t) = \sum_{l,m} Y_{l,m}^{-2}(\theta_{\mathbf{J}}, \phi_{\mathbf{J}}) \mathcal{A}_{l,m}(t) \exp -i\phi_{l,m}(t). \quad (1.32)$$

The **SpinTaylorF2** model is a frequency domain inspiral only model introduced in [174] publicly available in the `LSC_library` [168, 197]. This model only considers the  $(l, m) = (2, \pm 2)$  spherical modes in Eq. 1.32. This is the dominant mode to consider when modeling most CBC inspirals. Higher order modes,  $l > 2$ , have amplitudes that are typically one or more orders of magnitude less than  $l = 2$  modes for systems with near equal mass ratios that have total angular momentum that are oriented *face-on/off* to the observer ( $\theta_{\mathbf{J}} = 0, \pi$ ). These higher order modes have been shown to be larger for the late-inspiral portion of the waveform for systems with larger mass ratios that have total angular momentum that are oriented in the sky *edge-on* to the observer ( $\theta_{\mathbf{J}} = \pi/2, 3\pi/2$ ) [40, 170, 148, 67, 66, 65, 257]. For the purposes of this thesis we have chosen to focus on “face-on” systems (see Chapter 3), i.e. we assume that  $\mathbf{J}$  is either aligned or anti-aligned with the observer,  $\mathbf{N}$ , so that  $\theta_{\mathbf{J}} = 0^\circ$  or  $180^\circ$ . For face-on/off cases,  $\psi_{\mathbf{J}}$  will disappear from the waveform expression thus the underlying waveform is approximated well by the **SpinTaylorF2** model. These systems will also be, on the average, more luminous than edge-on systems and thus more likely to be detected [90]. Therefore I use this waveform model heavily in Chapter 3. The remaining portion of this section is devoted to deriving this model.

Consider an NSBH system consisting of a BH with mass  $M_{BH}$ , spin  $\mathbf{S}_{BH}$ , and a non-spinning neutron star of mass  $M_{NS}$  (see Figure 1.10). Let  $\hat{\mathbf{N}}(\theta, \phi)$  be the unit vector along the line-of-sight from the observing laser interferometer detector to the binary system. The component of  $\mathbf{S}$  along  $\mathbf{L}$  is determined by the quantity  $\kappa = \hat{\mathbf{S}} \cdot \hat{\mathbf{L}}$ , and the component of  $\mathbf{S}$  orthogonal to  $\mathbf{L}$  is

$$\mathbf{S}^\perp = \mathbf{S} - (\mathbf{S} \cdot \hat{\mathbf{L}}) \hat{\mathbf{L}}. \quad (1.33)$$

<sup>28</sup>Legal disclaimer: “The content and the text presented in this section are copied from [40, 174, 170, 148, 67, 66, 65, 257] and a paper I wrote with co-authors K. Haris, Tito Dal Canton, Henning Fehrmann, Badri Krishnan, Andrew Lundgren, Alex B. Nielsen and Archana Pai [146] with minor paraphrasing. The use of these materials is protected under ‘Fair Use’ (UrhG §24,70,63) and consistent with the requirements of § 6 Abs. 1 PromO.”

<sup>29</sup>This is not the case for more exotic spin configurations such as *transitional precession*. For these systems the orientation of  $\mathbf{J}$  will change dramatically as the orbit decays [235].

<sup>30</sup>The angles  $(\theta_{\mathbf{J}}, \phi_{\mathbf{J}})$  denote the orientation of the total orbital angular momentum,  $\mathbf{J}$ , with respect to the observer  $\mathbf{N}$ .

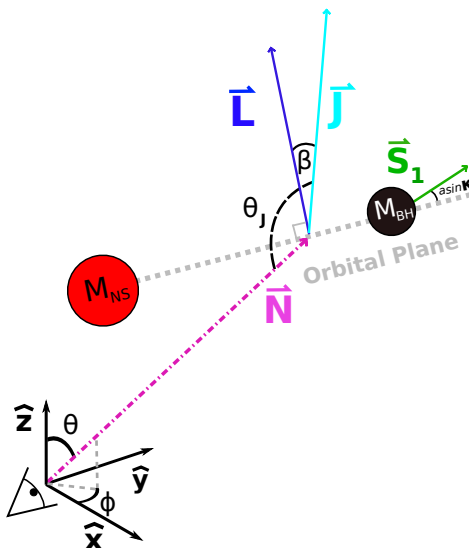


Figure 1.10: Diagram of parameters used to describe precession.

It can be shown that the direction of the total angular momentum  $\mathbf{J} = \mathbf{L} + \mathbf{S}$  is approximately conserved [38], and that  $\hat{\mathbf{L}}$  and  $\hat{\mathbf{S}}$  precess around  $\mathbf{J}$ . The magnitude of  $\mathbf{L}$  decreases steadily because of the emission of gravitational radiation but the magnitude of  $\mathbf{S}$  remains constant as does the angle between  $\mathbf{L}$  and  $\mathbf{S}$ . The opening angle  $\beta$ <sup>31</sup> of the precession cone is given by

$$\cos \beta = \hat{\mathbf{J}} \cdot \hat{\mathbf{L}}. \quad (1.34)$$

As the magnitude of  $\mathbf{L}$  decreases,  $\beta$  should increase in order to maintain the direction of  $\mathbf{J}$  and the angle between  $\mathbf{L}$  and  $\mathbf{S}$  [38]. However, the precession time-scale is smaller than the radiation reaction time scale (which determines the rate at which  $\|\mathbf{L}\|$  decreases). It can be shown [63] that for the advanced LIGO [12] and Virgo [29] detectors, to a reasonable approximation,  $\mathbf{L}$  and  $\mathbf{S}$  precess steadily around  $\mathbf{J}$  with a constant opening angle  $\beta$ . *Transitional precession* occurs when  $\mathbf{J} \sim \mathbf{0}$  at some point during the evolution of the binary system. Finally,  $\alpha_0$  is an azimuthal angle that expresses the orientation of  $\hat{\mathbf{L}}$  relative to  $\hat{\mathbf{J}}$  in the inertial detector frame and we shall define the angle  $\theta_J$  as  $\cos \theta_J = \hat{\mathbf{J}} \cdot \hat{\mathbf{N}}$ .

For a plane GW traveling in a direction  $\hat{\mathbf{z}}$ , and a frame  $(\hat{\mathbf{x}}, \hat{\mathbf{y}})$  (where  $\hat{x}$  and  $\hat{y}$  are the principle axes of polarization) in the plane orthogonal to  $\hat{\mathbf{z}}$ , the following tensors can be defined

$$\mathbf{e}_{ab}^+ = \hat{\mathbf{x}}_a \hat{\mathbf{x}}_b - \hat{\mathbf{y}}_a \hat{\mathbf{y}}_b, \quad \mathbf{e}_{ab}^\times = \hat{\mathbf{x}}_a \hat{\mathbf{y}}_b + \hat{\mathbf{y}}_a \hat{\mathbf{x}}_b. \quad (1.35)$$

As seen in Section 1.1.2, the gravitational wave can be written as a sum of two transverse polarizations

$$h_{ab}(t) = h_+(t) \mathbf{e}_{ab}^+ + h_\times(t) \mathbf{e}_{ab}^\times. \quad (1.36)$$

It is always possible to find a frame  $(\hat{\mathbf{x}}, \hat{\mathbf{y}})$  such that

$$h_+(t) = A_+(t) \cos 2\Phi(t), \quad h_\times(t) = A_\times(t) \sin 2\Phi(t), \quad (1.37)$$

where  $A_{+,\times}$  are slowly varying amplitudes and  $\Phi(t)$  is a rapidly varying phase. For the case of a binary system, the wave-frame  $(\hat{\mathbf{x}}, \hat{\mathbf{y}})$  is tied to the direction of the orbital angular momentum, and  $\hat{\mathbf{x}}$  is taken to be  $\pm \hat{\mathbf{N}} \times \hat{\mathbf{L}}$ . The direction of  $\mathbf{x}$  in the detector frame defines a polarization angle  $\psi$  and, following [38], the following convention is chosen:

$$\psi(t) = \tan^{-1} \left( \frac{\hat{\mathbf{L}}(t) \cdot \hat{\mathbf{z}} - (\hat{\mathbf{L}}(t) \cdot \hat{\mathbf{N}})(\hat{\mathbf{z}} \cdot \hat{\mathbf{N}})}{\hat{\mathbf{N}} \cdot (\hat{\mathbf{L}}(t) \times \hat{\mathbf{z}})} \right). \quad (1.38)$$

<sup>31</sup>The opening cone angle should not be confused with the spin-orbit parameter Eq. 1.28.

Note that because of precession, the direction of  $\mathbf{L}$  changes in time and thus  $\psi$  also changes with time. With these conventions, the expressions for  $h_{+,\times}$  are:

$$h_{+}(t) = -\frac{2\pi M}{rD} \left[ 1 + (\hat{\mathbf{L}}(t) \cdot \hat{\mathbf{N}})^2 \right] \cos 2\Phi(t), \quad (1.39)$$

$$h_{\times}(t) = -\frac{2\pi M}{rD} \left[ -2 \hat{\mathbf{L}}(t) \cdot \hat{\mathbf{N}} \right] \sin 2\Phi(t), \quad (1.40)$$

where  $D$  is the distance to the binary system and  $r$  is the binary orbital diameter.

It is also convenient to express the BH spin via the dimensionless vector  $\chi := \mathbf{S}_{\text{BH}}/M_{\text{BH}}^2$ . It is sometimes advantageous to decompose  $\chi$  into components parallel and perpendicular to  $\hat{\mathbf{L}}$ ,  $\chi^{\parallel}$  and  $\chi^{\perp}$  respectively. The total dimensionless spin magnitude is thus  $\chi = \sqrt{(\chi^{\parallel})^2 + (\chi^{\perp})^2}$ .

As first introduced in Eq. 1.8, the detector response functions to these polarizations are denoted by  $F_{+}(\theta, \phi, \psi)$  and  $F_{\times}(\theta, \phi, \psi)$ . In general, the signal seen by the detector  $h(t)$  will be a linear combination of the two polarizations:

$$\begin{aligned} h(t) &= h_{+}(t)F_{+}(\theta, \phi, \psi(t)) + h_{\times}(t)F_{\times}(\theta, \phi, \psi(t)) \\ &= A(t) \cos[2\Phi(t) + \varphi(t)], \end{aligned} \quad (1.41)$$

where

$$\begin{aligned} A(t) &= \frac{2\pi M}{rD} \left( \left[ 1 + (\hat{\mathbf{L}}(t) \cdot \hat{\mathbf{N}})^2 \right]^2 F_{+}(\theta, \phi, \psi(t)) \right. \\ &\quad \left. + 4 \left[ \hat{\mathbf{L}}(t) \cdot \hat{\mathbf{N}} \right]^2 F_{\times}(\theta, \phi, \psi(t)) \right)^{1/2}, \end{aligned} \quad (1.42)$$

and

$$\varphi(t) = \tan^{-1} \left( \frac{2 (\hat{\mathbf{L}}(t) \cdot \hat{\mathbf{N}}) F_{\times}(\theta, \phi, \psi(t))}{\left[ 1 + (\hat{\mathbf{L}}(t) \cdot \hat{\mathbf{N}})^2 \right] F_{+}(\theta, \phi, \psi(t))} \right). \quad (1.43)$$

In summary, gravitational wave signals from an NSBH precessing binary system can be expressed in terms of the following parameters: the component masses ( $M_{\text{BH}}, M_{\text{NS}}$ ), the black hole spin vector  $\mathbf{S}$ , the luminosity distance  $D$ , the polar angles of total angular momentum vector ( $\theta_J, \psi_J$ ), the sky location of the source ( $\theta, \phi$ ), the time of arrival of the signal  $t_0$  and the initial phase  $\phi_0$ .



## 1.2 Matched filtering

Matched filtering is a methodology used to determine if data from a gravitational wave detector  $x(t)$ , contains some signal of known form,  $h(t)$ , or only Gaussian noise  $n(t)$ <sup>32</sup>. Thus, in the absence of a signal,

$$x(t) = n(t), \quad (1.44)$$

and in the presence of a signal

$$x(t) = h(t) + n(t). \quad (1.45)$$

$P(h)$  is the *a priori* probability that a signal  $h$  is present.  $P(x)$  is the probability that the data stream  $x$  is observed.  $P(x|h)$  is the conditional probability of measuring the data stream  $x$  assuming a signal  $h$  is present.  $P(h|x)$  denotes the conditional probability that a signal,  $h(t)$ , is present in a given data stream,  $x(t)$ .  $P(h|x)$  can be calculated via Baye's law of conditional probabilities.

$$P(h|x) = \frac{P(x|h)P(h)}{P(x)} \quad (1.46)$$

$P(x)$  can be calculated by assuming that there are two possibilities: either a signal  $h(t; \Omega)$  described by a particular set of parameters,  $\Omega$ , is present or absent in the data stream  $x(t)$ .  $P(0)$  is the *a priori* probability that a signal,  $h(\Omega)$ , is not present.  $p(x|0)$  is the probability density of observing the data stream,  $x(t)$ , absent of a signal.  $p(x|h(\Omega))$  is the probability density of observing the data stream,  $x(t)$ , with a signal,  $h(\Omega)$ , present.  $p(\Omega)$  is the probability density that a signal  $h(\Omega)$  is characterized by a set of parameters  $\Omega$ .

$$P(x) = P(x|0)P(0) + P(x|h)P(h) = p(x|0)P(0) + P(h) \int d^N \Omega p(\Omega) p(x|h(\Omega)) \quad (1.47)$$

The *likelihood ratio*,  $\Lambda$ , is used to describe the plausibility of observing a given value of a parameter following the formalism of the Neyman-Pearson lemma. The definition is as follows.

$$\Lambda \equiv \int d^N \Omega \Lambda(\Omega) = \int d^N \Omega p(\Omega) \frac{p(x|h(\Omega))}{p(x|0)} \quad (1.48)$$

Plugging Eq. 1.47 into Eq. 1.46 yields the following expression.

$$P(h|x) = \frac{\Lambda}{\Lambda + P(0)/P(h)} \quad (1.49)$$

The noise,  $n(t)$ , is said to be *stationary* if its statistical properties do not change with time. For example, if the ensemble average of the product of the noise observed at two times,  $t$  and  $t'$ , is only a function of the difference between those two times.

$$\langle n(t)n(t') \rangle = \alpha(t - t') \quad (1.50)$$

Here the brackets  $\langle \cdot \rangle$  denote an average over many realizations of the noise, and  $\tilde{n}(f)$  denotes the Fourier transform of  $n(t)$ .

The *power-spectral-density* (PSD)  $S_n(f)$  describes the average sensitivity of the detector for a range of time. Noise sources,  $n(t)$ , greatly impact the detector's sensitivity for detecting gravitational waves in different frequency ranges. The shape of the PSD is dependent on the

---

<sup>32</sup>Legal disclaimer: "The content and the text presented in this section are copied from a paper I wrote with co-authors K. Haris, Tito Dal Canton, Henning Fehrmann, Badri Krishnan, Andrew Lundgren, Alex B. Nielsen and Archana Pai [146], and another paper that I wrote with Henning Fehrmann, Badri Krishnan, Franz Harke and Alex B. Nielsen [145]. I also used material from [255, 34, 122, 91, 88, 90]. The use of these materials is protected under 'Fair Use' (UrhG §24,70,63) and consistent with the requirements of § 6 Abs. 1 PromO."

instruments susceptibility of the source of these various noise sources: some from fundamental *stationary* processes that contribute to the stationary noise component of the PSD (processes that are seismic, quantum, and thermal in origin), and some transient noise sources (random non-astrophysical events *glitches* that are environmental in origin like lightning and or instrumental in origin like fluctuations in the electrical equipment powering the detector).

Due to presence of transient noise in the detector, the Gaussian portion of the noise can only be approximated to be stationary for short durations of time. When this stationary approximation is valid, the noise can be characterized by the single-sided *power-spectral-density* (PSD)  $S_n(f)$  by Fourier transforming Eq. 1.50.

$$\langle \tilde{n}^*(f) \tilde{n}(f') \rangle = \frac{1}{2} S_n(f) \delta(f - f'). \quad (1.51)$$

The PSD is calculated via a modified Welch's method [34, 212]. The basic idea of this method is to split up the detector data stream time segments and Fourier transform these segments to obtain the frequency domain PSD.<sup>33</sup>

The PSD is critical for matched filtering because it is used to define the inner product between two time-series  $x(t)$  and  $y(t)$ . To obtain an expression for the inner product, we assume the noise,  $n(t)$ , is a normal process with zero mean, characterized by a *correlation function*  $C_n$  and that the data streams,  $x(t)$  and  $y(t)$ , can be expressed as discrete sampled series of values,  $\{x_i : i = 1, \dots, N\}$  and  $\{y_i : i = 1, \dots, N\}$ . This allows for the following expression for  $P(x_i|0)$ ,

$$P(x_i|0) = \frac{\exp\left[-\frac{1}{2} \sum_{i,j=1}^N C_{ij}^{-1} x_i x_j\right]}{[(2\pi)^N |C_{ij}|^{1/2}]}. \quad (1.52)$$

The object in the exponent is the inner product of of the discrete series  $x$  against itself. The quantities  $C_{ij}$  and  $C_{ij}^{-1}$  are defined as follows:

$$\delta_{jk} \equiv \sum_l C_{jl} C_{lk}^{-1}. \quad (1.53)$$

Applying Parseval's theorem to Eq. 1.52 we obtain the following expression[122],

$$\lim_{\Delta t \rightarrow 0, T \rightarrow \infty} \sum_{j,k=1}^N C_{jk}^{-1} x_j y_k = 2 \left\{ \int_{-\infty}^{\infty} df \frac{\tilde{y}(f) \tilde{x}^*(f)}{S_n(|f|)} \right\}. \quad (1.54)$$

Therefore the inner product can be expressed as

$$(x|y) := 4\text{Re} \int_0^{\infty} \frac{\tilde{x}^*(f) \tilde{y}(f)}{S_n(f)} df. \quad (1.55)$$

This inner product is used to define the norm of a time series  $x(t)$  and a normalized time series  $\hat{x}$  in the usual way:

$$\|x\| := (x|x)^{1/2}, \quad \hat{x} = x/\|x\|. \quad (1.56)$$

The likelihood function  $\Lambda$  can be further simplified [122, 147]:

$$\begin{aligned} \Lambda &= \frac{P(x|h)}{P(x|0)} \\ &= \frac{p(x|h)}{p(x|0)} \end{aligned}$$

---

<sup>33</sup>Splitting up the data stream with this method reduces the effect of transient noise sources in the data stream.

$$\begin{aligned}
&= \frac{p(x-h|0)}{p(x|0)} \\
&= \frac{\exp\left[-\frac{1}{2}(x-h|x-h)\right]}{\exp\left[-\frac{1}{2}(x|x)\right]} \\
&= \exp\left\{-\frac{1}{2}[(x|x) - 2(x|h) - (h|h)] + \frac{1}{2}(x|x)\right\} \\
&= \exp\left[(x|h) - \frac{1}{2}(h|h)\right].
\end{aligned} \tag{1.57}$$

It is often more convenient to express Eq. 1.57 logarithmically

$$\log \Lambda = (x|h) - \frac{1}{2}(h|h). \tag{1.58}$$

The idealized procedure to search for a signal with unknown parameters is to compute  $\log \Lambda$  for all suitable points in a given parameter space and to find the point where  $\log \Lambda$  is maximum. The likelihood can be analytically maximized for certain parameters (such as the *coalescence time*  $t_0$ , the initial phase  $\phi_0$  and an overall constant amplitude,  $A$ ) or by a Fast-Fourier transform [34]. It is particularly important to maximize over the *coalescence time* and *coalescence phase* of the CBC waveform, since these quantities cannot be determined *a priori* and will affect the match. Determining the ‘‘best match’’ coalescence phase,  $\phi_0$ , can be found by maximizing the match,  $m(t_0) = (x(f)|h(f))$ , with respect to,  $\phi_0$ ,

$$m(t_0) = 4\mathcal{R} \int_0^\infty df \frac{\tilde{x}(f) [\tilde{h}^*(f)]_{t_0=0}}{S_n(f)} \exp(2\pi i f t_0). \tag{1.59}$$

$m(t_0)$  is decomposed into a linear combination of real and imaginary values  $m_{real}(t_0)$  and  $m_{imaginary}(t_0)$  evaluated at  $\phi_0 = 0$ ,

$$m(t_0) = m_{real}(t_0) \cos 2\phi_0 + m_{imaginary}(t_0) \sin 2\phi_0. \tag{1.60}$$

It follows that at the maximum value of  $\hat{\phi}_0$  that  $m^2(t_0)|_{\hat{\phi}_0} = m_{real}^2 + m_{imaginary}^2$  and  $2\hat{\phi}_0 = \arg(z(t)) = \arg(m_{real}(t) + im_{imaginary}(t))$ . This yields the following maximum match:

$$\max_{t_0, \phi_0} m(t_0) = |z(t_0)| = 4 \int_0^\infty df \frac{\tilde{x}(f) [\tilde{h}^*(f)]_{t_0=0, \phi_0=0}}{S_n(f)} \exp(2\pi i f t_0). \tag{1.61}$$

Other parameters like the component masses (or other so-called *intrinsic parameters*) must be explicitly maximized over. These intrinsic parameters we denote as  $\lambda_i$ <sup>34</sup>.

A *template bank* is a collection of waveforms  $\{h_I\}$  labeled by the index  $I$ . Template banks are used to match filter through the detector data for GW signals. Given a template bank, we would like to know how effective it is in recovering a given signal  $h$ . This is quantified in terms of a number, namely the *fitting-factor* (FF) [91] defined as,

$$FF(h, \{h_I\}) = \max_I \mu(\hat{h}, \hat{h}_I), \tag{1.62}$$

where

$$\mu(h, h_I) = \max_{t_0, \phi_0} (\hat{h}|\hat{h}_I(t_0, \phi_0)) \tag{1.63}$$

---

<sup>34</sup>I only consider binary systems with circular orbits in this thesis and I also do not consider any parameters associated with the internal structure of the neutron star EOS. Deviations from the assumption are expected to be small for the inspiral portion of the GWs.

is the *match* between  $h$  and  $h_I$ , and

$$\hat{h} = \frac{h}{\sqrt{\mu(h, h)}}. \quad (1.64)$$

$\mu(h, h_I)$  represents the fraction of the optimal SNR,  $\rho_{\text{optimal}} = |h|$ , of a signal  $h$  captured by the template  $h_I$ . The fitting factor depends on a particular template bank and a particular *target* waveform  $h$ . Since we will compute this for a fixed template bank, we usually drop its dependence on  $\{h_I\}$  and write  $FF(h)$ . The loss in SNR can be quantified by the match between a signal and the nearest template and can be formulated geometrically [206, 207]. The match between nearby points in parameter space can be approximated as

$$\mu(\hat{h}(\lambda), \hat{h}(\lambda + d\lambda)) = 1 - g_{ij} d\lambda^i d\lambda^j + \dots \quad (1.65)$$

with the metric

$$g_{ij} = -\frac{1}{2} \left. \frac{\partial^2 \mu(\hat{h}(\lambda), \hat{h}(\lambda'))}{\partial \lambda'_i \partial \lambda'_j} \right|_{\lambda'=\lambda}. \quad (1.66)$$

This metric<sup>35</sup> is useful in quantifying the density of templates. The higher the metric determinant, the higher the required template density for a fixed given allowed SNR loss (which corresponds to a given minimal match) (see Chapter 2).

A template bank's *effectualness* is determined by quantifying how well it can recover a set of injected signals. This procedure is the so-called *banksim* and is one of the primary tools used to test and compare the effectualness of template banks prior to be implemented in a search. To quantify the relative improvement of two or more template banks, the relative improvement in *detection volume* [88] is calculated. The detection volume,  $\mathcal{V}$ , is assumed to be proportional to the sum of the cube of the product of the optimal SNR of the injections,  $\rho_i$ , with the fitting factor,  $FF_i$ , obtained from attempting to recover a set of injected NSBH signals,

$$\mathcal{V} \propto \sum_i (FF_i \rho_i)^3. \quad (1.67)$$

By taking the ratio of the *detection volumes* of two template banks,  $\mathcal{V}_2$  vs  $\mathcal{V}_1$ , the *relative detection volume* is obtained providing another tool to determine which template bank will perform better in a search.

---

<sup>35</sup>For Gaussian stationary noise, one can show that the metric  $g_{ij}$  is equivalent to constructing the scalar product  $\frac{1}{2} \left( \frac{\partial \hat{h}}{\partial \lambda_i} \middle| \frac{\partial \hat{h}}{\partial \lambda_j} \right)$  and projecting out the parameters  $t_0$  and  $\phi_0$ .

### 1.3 Search pipeline

Assuming the background noise is approximately Gaussian, matched filtering is a powerful technique for finding a known signal. The detection of a statistically significant gravitational wave CBC inspiral event can be obtained by searching through multiple noise laden laser interferometer data streams via matched filtering (see Section 1.2) for a coincident wave signature in two or more laser interferometers [34, 255]<sup>36</sup>. The signals that a *search pipeline*, the computational procedure used to detect GW, attempts to detect are determined by generating a *template bank*, a targeted collection of GW signals (a.k.a. *templates*). There are currently three such pipelines that have been independently implemented to matched filter LIGO-Virgo [12, 29] data: PyCBC [88, 255, 196], GstLAL [69, 223, 180] and MBTA [30]. All these pipelines are capable of using the same template banks and they all follow the same basic procedure, differing slightly in how they remove GW candidates from consideration among other differences. For the purposes of simplicity I will summarize the mechanics PyCBC pipeline to illustrate how template banks are used to in GW searches.

Suppose  $M$  detectors produce  $M$  strain data streams, each will have different PSDs. These characteristic noise sensitivities are described by the  $S_N^{(M)}(f)$ . The PSDs from the different detectors are averaged over time and combined together into a *harmonic-mean-PSD*,  $\hat{S}_N^{(M)}(f)$ ,

$$S_n^{harmonic}(f_k) = M \left/ \sum_{i=1}^M \frac{1}{S_n^i(f_k)} \right. . \quad (1.68)$$

This harmonic mean PSD is instrumental in generating the template bank (see section 2) which in turn will be used to filter through the data streams<sup>37</sup>. The template bank must be regenerated if the PSDs of the individual detectors change significantly. More specifically the template bank is regenerated if a simulation of injected signals into the template bank (a *banksim*) results in more than 1% of the injected signals being recovered with a fitting factor under 97% [15]. Subsequent analysis of the parameters associated with a detection are complicated when multiple template banks are used in a search [15]. While it is possible to use other methods for averaging the PSDs from the different detectors, Eq. 1.68 has been demonstrated to be the most appropriate method for building template banks [255].

Each data stream is broken up into segments that avoid regions of the data stream that contain *non-stationary transients* and too noisy to search for signals. Regions of the data stream that contain transient noise (short duration loud events, *glitches*) are identified and *vetoed* from further consideration. The sources of all the possible glitches so far observed in LIGO-Virgo and other laser interferometers are currently not well known. However it is likely that some of the very short duration noise transients arise from instabilities in the detector’s control system [255]. It is important that these types of disturbances must be removed from consideration as they have a tendency to *ring* the impulse response of the detector making it difficult to distinguish potential signals from the noise. These removed segments are considered as *dead time*, hence any portion of a potential signal in these segments are lost. It is unlikely that these removed segments will arise in missing the detection of longer duration signals, since the duration of these glitches typically last seconds. However, it is possible that some of portions of potential signals can be lost as their signal interrupted resulting in a loss of SNR. For example, such a glitch occurred during the first BNS detection in the Livingston detection [25].

<sup>36</sup>Legal disclaimer: “The content and portions of the text presented in this section are taken from [34, 255] with minor paraphrasing. The use of this material is protected under ‘Fair Use’ (UrhG §24,70,63) and consistent with the requirements of § 6 Abs. 1 PromO.”

<sup>37</sup>There are many alternative ways of averaging PSDs from multiple detectors together. Including just choosing a PSD from one of the detectors. Or potentially constructing multiple template banks for each detector. While there is nothing theoretically incorrect with using other methods, injected signals have been shown to be recovered the best by PSDs constructed via Eq. 1.68 [255].

After removing glitches which can be explained by a well known non-astrophysical process, the surviving segments of the data stream are Fourier transformed. In the frequency domain, this transformed data is further refined by identifying any remaining *glitches* that were not eliminated previously in the time domain and removing them from further analysis. The surviving frequency domain data is then matched filtered against the two orthogonal phases,  $\{h_{\text{cos}}, h_{\text{sin}}\}$ , that correspond to the templates contained in the template bank in order to calculate an SNR for each detector,

$$\rho^2[t] = \frac{\langle s|h_{\text{cos}} \rangle^2 + \langle s|h_{\text{sin}} \rangle^2}{\langle h_{\text{cos}}|h_{\text{cos}} \rangle}. \quad (1.69)$$

This combination is chosen to maximize SNR over the coalescence phase [34]. The Fast Fourier Transform is a computationally efficient way to compute inner products as a function of coalescence time.

The  $\chi^2$  test is subsequently applied to these lists of triggers and a new re-weighted SNR is calculated for each trigger. This test is applied to eliminate non Gaussian noise sources that yield high SNRs that manage to slip by the earlier stages of glitch removal<sup>38</sup>. This test is conducted by taking the template that corresponds to each trigger with SNR  $\rho_i$  and splitting the segment matching up into  $p$  bins [34, 15]<sup>39</sup>. The  $\chi^2$  statistic measures the how the distribution of the measured power of the gravitational wave signal deviates from its expected value for each bin,

$$\chi^2 = p \sum_i^p [(\rho_{\text{cos}}^2/p - \rho_{\text{cos},i})^2 + (\rho_{\text{sin}}^2/p - \rho_{\text{sin},i})^2]. \quad (1.70)$$

In Eq. 1.70  $\rho_{\text{cos}}$  and  $\rho_{\text{sin}}$  are the SNRs obtained by individually matched filtering the two orthogonal waveform phases corresponding a template in the template bank. Larger values of  $\chi^2$  indicate that an actual signal matching the template is less likely.

The  $\chi^2$  statistic defines the creation of an *re-weighted SNR*,

$$\hat{\rho} = \begin{cases} \rho / [(1 + (\chi^2 / (2p - 1))^3) / 2]^{1/6}, & \text{if } \chi^2 > 1. \\ \rho, & \text{else.} \end{cases} \quad (1.71)$$

The root mean squared average of the re-weighted SNRs of events in each detector data stream is calculated into a combined re-weighted SNR,

$$\hat{\rho}_C = \sum_n^M (\hat{\rho}_n)^2. \quad (1.72)$$

Data segments with a combined re-weighted SNR under a threshold of 5.5 are removed from consideration. Segments that yield an re-weighted SNR above this limit are called *triggers* and are potential candidates for CBC GW signals.

A single GW signal can potentially match with multiple templates in the bank. These templates that are rung are not independent and must be grouped together, *clustered* together, for subsequent analysis [34, 255]. Data stream segments containing triggers from each detector are compared against all other data segments observed during the duration of the search,  $T_{\text{obs}}$ . It is not sufficient for a trigger has a high re-weighted SNR; a *coincidence* test and *time slides* study are used to quantify the significance of a detection and the background noise respectively. These test verify that events with high SNR appear in both detectors with the correct delay. In previous detection eras, the harmonic mean PSD was not used to standardize the template banks used in the various detectors. Instead the template banks were generated

<sup>38</sup>However, this test has a tendency to make it more difficult to detect highly modulated and short duration GWs like those produced by highly precessing CBC events.

<sup>39</sup>The number of bins varies with the choice of search pipeline and the component masses of the templates[15].

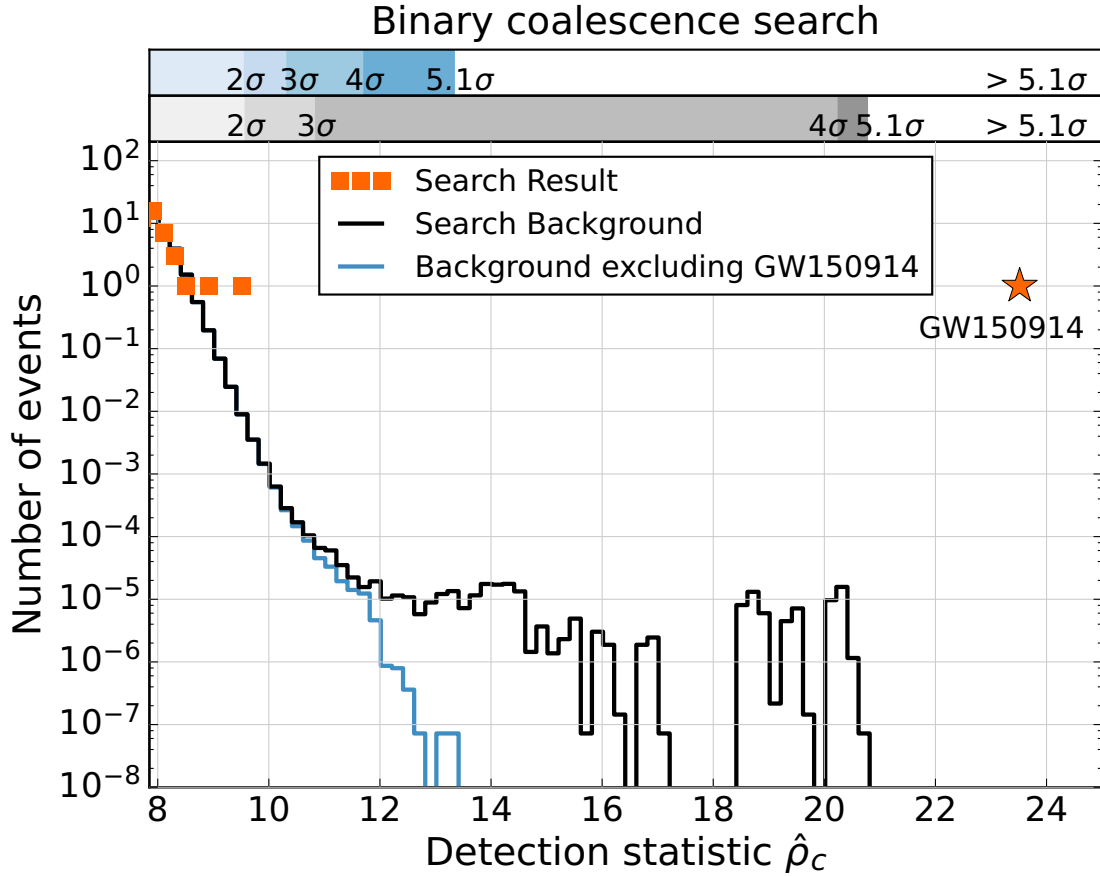


Figure 1.11: The PyCBC time-slide significance analysis of the observation run that led to the detection of GW150914. This  $5\sigma$  event was more significant than any of the background events, so strong in fact that the higher significance data is dominated by this event (as evident by measuring the background after removing the segment of the data stream containing the event). The image is taken from [14] and the caption is paraphrased from the same source.

independently according to the PSDs of the individual detectors. This made the coincident test more complicated as templates from two separate banks had to be reconciled in order to characterize coincident events. Fortunately in the O1 and O2 detection eras for LIGO-Virgo, the coincident test became trivial since one template bank is generated for both detectors.

The time slide test is designed to determine how often a non astrophysical coincident *false alarm* detection could be made. This is a necessary tool for estimating the background noise. The test takes two or more data streams and chops them up into segments and rearranges the order in time. Coincident events found when comparing the re-arranged data segments are deemed background noise since this procedure is independent of the original time delay. The total length of background data analyzed during this test is  $T_b = T_{obs}^2/\delta$ , where  $\delta$  is the characteristic length of the time-shift interval utilized during the coincidence test ( $\delta = 0.1s$  for O1 [15]). The minimum *False-Alarm-Rate* (FAR) will scale as  $T_{min} = \delta/T_{obs}$ .

The significance of a trigger is quantified by examining the histogram distribution of re-weighted SNR measurements by performing  $N_{slides}$  time slides. By binning the re-weighted SNR time slide measurements, it is possible to compare how likely the non-time-slide re-weighted SNR measurement is in the absence of a detection. The FAR is measured by taking the number of time slide re-weighted SNR measurements that occur in the same bin as the re-weighted SNR from the non-time-slide re-weighted SNR and computing the following detection rate given the

observation time duration of the data stream,  $T_{obs}$ ,

$$FAR = 1/(N_{slides}T_{obs}). \quad (1.73)$$

Triggers with a FAR above one false detection in 100 years are considered to be legitimate observations of gravitational waves [255].

To further quantify the significance of a trigger, a p-value can be assigned<sup>40</sup>. For a given trigger that is assumed to be noise, we can express the probability that there are  $n^*$  or fewer background events with an equal or higher re-weighted SNR,  $\hat{\rho}_C^*$ , where  $N_b$  is the total number of background events and  $N_e$  is the number of candidates being considered,

$$p(n_b \leq n^* | N_e = 1, N_b)_0 = \frac{1 + n^*}{1 + N_b}. \quad (1.74)$$

It follows that larger re-weighted SNR values,  $\hat{\rho}_C$  values correspond to a smaller number of background events,  $n_b$ , and the probability that a coincident noise event is above a particular  $\hat{\rho}_C$  threshold is as follows:

$$p(\hat{\rho}_C \geq \hat{\rho}_C^* | N_e = 1, N_b)_0 = \frac{1 + n_b(\hat{\rho}_C^*)}{1 + N_b}. \quad (1.75)$$

Similarly, the probability that there are no background candidates above a given re-weighted SNR threshold  $\hat{\rho}_C^*$  is as follows,

$$p(\text{none above } \hat{\rho}_C^* | N_e, N_b)_0 = \left(1 - \frac{1 + n_b(\hat{\rho}_C^*)}{1 + N_b}\right)^{N_e}. \quad (1.76)$$

If all candidate events are noise the probability that a least one of the  $N_e$  clustered candidate events is above the re-weighted SNR threshold,  $\hat{\rho}_C^*$  is as follows,

$$p(\geq 1 \text{ above } \hat{\rho}_C^* | N_e, N_b)_0 = 1 - \left(1 - \frac{1 + n_b(\hat{\rho}_C^*)}{1 + N_b}\right)^{N_e}. \quad (1.77)$$

Marginalizing Eq. 1.77 over  $N_e$  clustered candidate events obtains the following probability,

$$p(\geq 1 \text{ above } \hat{\rho}_C^* | N_b)_0 = \sum_{N_e} p(\geq 1 \text{ above } \hat{\rho}_C^* | N_e, N_b)_0 p(N_e | N_b). \quad (1.78)$$

The probability  $p(N_e | N_b)$  is calculated by approximating the coincident noise events obtained by the measurement of the time-shifted background events as a Poisson process,

$$p(N_e | N_b) \equiv p(N_e | \frac{N_b T}{T_b}) = \frac{N_b T}{T_b} \frac{\exp\left(-\frac{N_b T}{T_b}\right)}{N_e!}. \quad (1.79)$$

By plugging Eq. 1.79 into Eq. 1.78 and exploiting that for a Poisson process,

$$\sum_{N_e} \frac{N_b T}{T_b} \frac{\exp\left(-\frac{N_b T}{T_b}\right)}{N_e!} = 1, \quad (1.80)$$

---

<sup>40</sup>In O1, p-values were published for CBC GW detections. However it is worth noting that it can be shown that the p-value of a coincident event (unlike the FAR) will vary depending on the length of the observation period. In O2, p-values were no longer published in favor of the FAR, which is not susceptible to this ambiguity.



we obtain the following expression:

$$p(\geq 1 \text{ above } \hat{\rho}_C^* | N_b)_0 = 1 - \sum_{N_e} \left( \frac{N_b T}{T_b} \left[ 1 - \frac{1 + n_b(\hat{\rho}_C^*)}{N_b} \right] \right)^{N_e} \frac{\exp\left(\frac{N_b T}{T_b}\right)}{N_e!}. \quad (1.81)$$

Further exploiting the Poisson summation property used in the previous step simplifies the probability is as follows:

$$\begin{aligned} p(\geq 1 \text{ above } \hat{\rho}_C^* | N_b)_0 &= 1 - \sum_{N_e} \left( \frac{N_b T}{T_b} \left[ 1 - \frac{1 + n_b(\hat{\rho}_C^*)}{N_b} \right] \right)^{N_e} \\ &\times \frac{\exp\left[\frac{N_b T}{T_b} \left( 1 - \frac{1 + n_b(\hat{\rho}_C^*)}{N_b} \right)\right]}{N_e!} \exp\left[\frac{-\frac{N_b T}{T_b} (1 + n_b(\hat{\rho}_C^*))}{N_b}\right]. \end{aligned} \quad (1.82)$$

Simplifying Eq. 1.82 yields the desired closed form expression for quantifying the significance of an GW candidate event,

$$p(\geq 1 \text{ above } \hat{\rho}_C^* | N_b)_0 = 1 - \exp\left[\frac{-T(1 + n_b(\hat{\rho}_C^*))}{T_b}\right]. \quad (1.83)$$

After this analysis, an alert is sent to EM and neutrino observatories to determine if there were companion signals. It can take multiple coincident observations to triangulate the sky location of the source of the gravitational wave to a high enough precision for further observation of counterpart signals. However, this may not be enough to locate the precise sky location as the triangulation of the GW signals results in a large search region. Given that there is a short window (i.e. hours) to observe the higher energy components of the signal (like components of the signals in the  $\gamma$ -ray spectrum), luck is still an important factor in finding the counterpart signals.

## 1.4 Acknowledgments

I would like to thank Christoph Dreißigacker and Henning Fehrmann for assisting in the translation of the ‘‘Kurzzusammenfassung’’.



CBC template banks must be constructed efficiently, placing the minimum required template without compromising the final *coverage* and *effectualness* of recovering signals from the desired CBC parameter space. The more templates in the bank, the higher computational cost of performing a search. In the absence on an analytic expression governing the mismatch between CBC waveforms, stochastic and hybrid methods have been utilized to place templates. In this chapter, I provide a background for the template placement algorithms detailed in this thesis.

## 2.1 Geometric lattices

If a parameter space has a known analytic form of the mismatch metric, one can place templates in a *lattice* (a grid of points placed obeying some tessellated geometric pattern) according to that metric to ensure that the space is covered<sup>1</sup>. In lower dimensional spaces, this method of covering will always place templates in a more efficient manner than the stochastic method (see Section 2.2), which does not account for how close templates should be placed together [179]. Currently geometric banks are used exclusively for BNS systems in LIGO-Virgo searches, since these lower mass systems can be effectively modeled by inspiral only waveforms since ISCO of these systems exceeds the sensitivity the Earth based laser interferometers (more on this in Section 2.3).

This problem of efficiently placing templates is similar (but **not identical**) to the “sphere packing problem”, in which one must pack incompressible (i.e. non overlapping) spheres as tightly as possible into a confined space to minimize the gaps between spheres. For the purposes of detection of CBC waveforms, the confined space represents the CBC parameter space and the spheres (which represent the *template maximal mismatch isosurfaces* indicating regions of the bank that in which all signals can be recovered by a single template to a pre-specified maximal mismatch) can overlap, **unlike** the sphere packing problem, and must cover the entire space. For the sphere packing problem, Lord Kelvin’s conjecture suggests that for a three dimensional space that is *flat* (more specifically, a manifold that can be mapped to a flat space by a map that preserves the angles between adjacent points), a lattice of the centers of individual template isosurfaces built from truncated octahedrons minimize the space between adjacent cells. There are two distinct solutions for the three dimensional sphere packing problem, face-centered-cubic and hexagonal-close-packed lattices. Unlike the sphere packing problem, the coverage

---

<sup>1</sup>Legal disclaimer: “The content and portions of the text presented in this section are taken from [224, 179, 84, 230, 229, 62, 268] with minor paraphrasing. The use of these materials are protected under ‘Fair Use’ (UrHG §24,70,63) and consistent with the requirements of § 6 Abs. 1 PromO.”

problem has solutions that are  $A_N^*$  lattices. While in two dimensions, both the sphere packing problem and coverage solutions are hexagonal lattices ( $A_2^*$ ). In three dimensions, the coverage problem solution is a body-center-cubic lattice (i.e.  $A_3^*$ ). These kind of “ $A_N^*$  lattices” (a group describing a uniform symmetric n-dimensional grids generated by tessellating some fundamental regular polygonal structure) have been shown to adequately cover CBC parameter spaces for the purposes of template bank construction [224, 97, 206, 207, 45, 84, 62]. These lattices are generated by forming an additive group out of a set of discretized points,  $A_N^* = \{\nu_\zeta\}$ , that are linear combinations of the *basis* vectors,  $\{\mathbf{l}_i\}_{i=1}^n \in \mathbb{E}^N$  [224].

$$\{\nu_\zeta\} = \left\{ \sum_{i=1}^N \zeta^i \mathbf{l}_{(i)} \mid \zeta^i \in \mathbb{Z} \right\} \quad (2.1)$$

The *generator matrix* of this lattice is a  $M \times N$  object that contains  $M \geq N$  columns corresponding to the  $M$  components to the  $N$  basis vectors. This allows for the alternative representation of the lattice,  $A_N^*$ , as the following.

$$A_N^* = \{M\zeta \mid \zeta \in \mathbb{Z}^N\} \quad (2.2)$$

The positive definite symmetric *Gram matrix*,  $A$ , can be constructed as follows.

$$A := M^T M \quad (2.3)$$

It can be shown that the coefficient of the Gram matrix are the mutual scalar products of lattice basis vectors,  $A_{ij} = \mathbf{l}_i \mathbf{l}_j = \delta_{ab} l_i^a l_j^b$ . Different choices of basis will result in lattices with a specific *fundamental parallelotope* (FP).

$$\text{FP}(\{\mathbf{l}_i\}) := \{ \mathbf{x} \in \mathbb{E}^n \mid \mathbf{x} = \theta^i \mathbf{l}_i, 0 \leq \theta^i < 1 \} \quad (2.4)$$

The FP is the *fundamental region* that is tessellated to generate the lattice over an n-dimensional Euclidean space  $\mathbb{E}^n$ . The volume of this region is related to the Gram matrix,  $A$ .

$$\text{fundamental volume} = \sqrt{\det|A|} \quad (2.5)$$

For example, the *nearest-neighbor region* (also known as the *Wigner-Seitz cell* (WS)) can be defined as follows.

$$\text{WS}(A_N^*) := \{ \mathbf{x} \in \mathbb{E}^N \mid \|\mathbf{x} - \nu_0\| \leq \|\mathbf{x} - \nu_\zeta\| \} \quad (2.6)$$

The maximum distance between any two adjacent point in the lattice is called the *circumradius* of the lattice or the *covering radius* of the WS cell,  $R$  (see Fig. 2.1). In order to construct an effectual lattice of this form for a CBC template bank, a set of coordinates must be found in which the metric is constant in parametrization of the space such that the parameter space can be covered by templates that are (approximately) spherical or ellipsoidal. In these coordinates, the resulting template density, which is proportional to the inverse square root of the determinate of the mismatch metric, will be approximately uniform over the parameter space.

$$\text{number of templates} \propto \sqrt{\det|g_{ij}|}^{-1} \quad (2.7)$$

Early searches for CBC events in LIGO-Virgo data have implemented template banks constructed with  $A_2^*$  (hexagonal) lattices over  $\{\tau_0, \tau_3\}$  coordinates for 2 PN SPA waveforms (i.e. waveforms that consider the second order single phase approximation models). For higher PN orders and additional degrees of freedom for the system, building geometric lattices becomes problematic as finding flat coordinates and an analytic expression for the metric  $g_{ij}$  becomes tougher [97, 206, 207, 45, 84, 62, 70, 137].

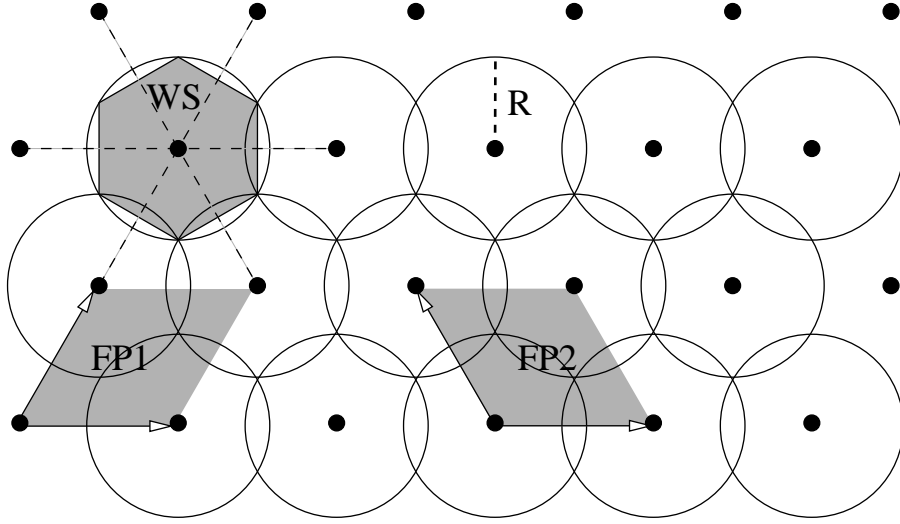


Figure 2.1: An  $A_2^*$  (i.e. hexagonal) lattice used to build a geometric bank.  $WS$  indicates a Wigner-Seitz cell. Image is taken from [224] and the caption is paraphrased from the same source.

$$\|h[\theta^\mu + d\theta^\mu] - h[\theta^\mu]\|^2 = \|h_\mu d\theta^\mu\|^2 = (h_\mu, h_\nu) d\theta^\mu d\theta^\nu = g_{\mu\nu} d\theta^\mu d\theta^\nu \quad (2.8)$$

As an example, the distances between adjacent templates along one axis of an  $A_2^*$  lattice is given by:

$$\{dx_i\} = \left\{ 2\sqrt{\frac{1 - MM}{g_{ii}}} \mid i = 0, 1, \dots, N - 1 \right\}. \quad (2.9)$$

This ensures that no one template has a mismatch with any other template in the bank greater than the *minimal match* (MM) threshold<sup>2</sup> [84]. One method for creating a  $A_2^*$  lattice is as follows.

1. A point in the parameter space is selected and given a unique *cell id*.
2. If the point is physical<sup>3</sup>, a metric is calculated and 6 connectors are drawn to neighboring points to form a hexagon according to Eq 2.9.
3. Of the neighboring points that are physical, additional points are spawned those points such that the same spacing as the original cell to expand the hexagonal lattice without duplication.
4. Lattice points that are in unphysical region of parameter space do not have templates placed.
5. The lattice grows until no more physical lattice points can be placed.

In three or more dimensions, generating  $A_N^*$  lattices efficiently is increasingly difficult particularly due to the shape of the borders of the physically relevant region of the parameter space.

<sup>2</sup>Establishing a “minimal match” is equivalent to establishing a “maximal mismatch” because, trivially, the minimal match = 1 - the maximal mismatch.

<sup>3</sup>Determining the physicality of a potential lattice point can be a computationally taxing procedure, particularly when there is no analytic expression for the boundaries of the parameter space.

A newer more computationally efficient  $n$ -dimensional algorithm overcomes this problem by taking advantage of the fact that the generator matrix (Eq. 2.2) can always be decomposed into the product of an  $m \times m$  orthogonal matrix,  $Q$ , and a lower  $m \times n$  triangular matrix,  $L$  [268]<sup>4</sup>. In this algorithm, the  $Q$  matrix can be considered as an overall rotation of the lattice and does not alter the lattice structure. On the other hand, the lower triangular matrix,  $L$ , is used directly to calculate the lattice vectors which determine the template bank distribution. The advantage of this lower triangular matrix, is that it allows for a hierarchical expression for the dependency of the borders of the higher dimensions on the lower dimensions.

To clarify, suppose each of the  $n$  dimensions,  $\lambda_i$ , has limits  $\lambda_i^{\min}, \lambda_i^{\max}$ . The borders in for  $\{\lambda_i | n - 1 > i > 0\}$  can be expressed as the following hierarchy of inequalities.

$$\begin{aligned} \lambda_0^{\min} &\leq \lambda_0 \leq \lambda_0^{\max} \\ \lambda_1^{\min}(\lambda_0) &\leq \lambda_1 \leq \lambda_1^{\max}(\lambda_0) \\ \lambda_2^{\min}(\lambda_0, \lambda_1) &\leq \lambda_2 \leq \lambda_2^{\max}(\lambda_0, \lambda_1) \\ &\dots \\ \lambda_{n-1}^{\min}(\lambda_0, \dots, \lambda_{n-2}) &\leq \lambda_{n-1} \leq \lambda_{n-1}^{\max}(\lambda_0, \dots, \lambda_{n-2}) \end{aligned} \quad (2.10)$$

Lattice placement is accomplished in a computationally efficient manner by using a sequence of parallelized loops to calculate the borders of each  $\lambda_i$  degree of freedom. In the outermost loop, templates are placed along the  $\lambda_0$  degree of freedom according to their associated lattice vectors. These outermost limits on  $\lambda_0$  are independent of all other degrees of freedom. In contrast, templates placed along the  $\lambda_{n-1}$  degree of freedom are placed by the innermost loop of the algorithm. Unlike the outermost limits, these innermost limits depend on all other degrees of freedom and must be recalculated for for each new cycle of iterations. Therefore, in order to generate templates in the subspace  $\lambda_{n-1}^{\min}(\lambda_0, \dots, \lambda_{n-2}) \leq \lambda_{n-1} \leq \lambda_{n-1}^{\max}(\lambda_0, \dots, \lambda_{n-2})$ , the limits  $\lambda_2^{\max}(\lambda_0, \dots, \lambda_{n-2}), \lambda_2^{\min}(\lambda_0, \dots, \lambda_{n-2})$  are recalculated when the values of  $\lambda_0, \dots, \lambda_{n-2}$  change. This algorithm differs with the two dimensional algorithm described earlier [84], because the borders for each of these degrees of freedom do not have to be recalculated for each lattice point (which is computationally inefficient).

## pycbc\_geom\_bank

In practice, geometric lattices are constructed via the PyCBC algorithms `lalapps_tmplbank`, `pycbc_geom_nonspinbank` and `pycbc_geom_aligned_bank` [233, 218, 46, 206, 207, 43, 84, 137, 62, 44, 197, 201, 138].

These algorithms place inspiral-only CBC templates into flat coordinates where the template isosurfaces are hyper-ellipsoids via the  $\xi$  coordinates [62] (see Figure 2.2). These coordinates are calculated as follows. First, the phase of the aligned spin inspiral waveform is expanded to 3.5 PN by way of the waveform phase PN coefficients  $\lambda_j^{(\mathbf{F}^2)}$  (see Section 1.1.4 Eqs. 1.18 and 1.19). Second, the fisher matrix as a function of the intrinsic parameters  $\theta$  for this template bank parameter space is calculated as follows.

$$g_{ij}(\theta) = \left( \frac{\partial h(\theta)}{\partial \theta^i} \middle| \frac{\partial h(\theta)}{\partial \theta^j} \right) \quad (2.11)$$

Third, the coalescence time and phase are maximized over (see Section 1.2), resulting in the lower dimensional metric  $\gamma$  that is a function of the of the PSD moments  $\mathcal{J}(\psi_\alpha)$ <sup>5</sup>.

$$g_{\alpha\beta} = \gamma_{\alpha\beta} - \frac{\gamma_{0\alpha}\gamma_{0\beta}}{\gamma_{00}} \quad (2.12)$$

<sup>4</sup>In this algorithm,  $m$  must be greater than or equal  $n$  (e.g. typically  $m = n + 1$ )

<sup>5</sup>If the upper a lower frequency cutoffs  $f_{0x_L}, f_{0x_U}$  do not depend on the masses and spins of the templates, these PSD moments do not vary over the parameter space. By default  $f_{0x_L} = 15\text{Hz}, f_{0x_U} = 2,000\text{ Hz}$ .

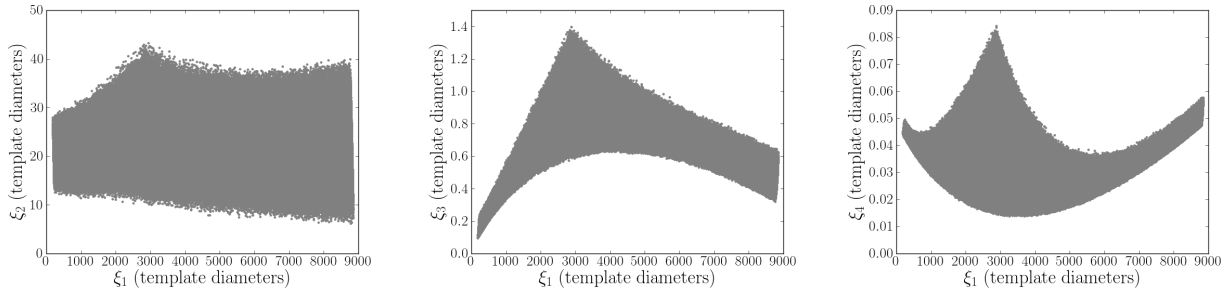


Figure 2.2: A plot of a BNS TaylorF2 template bank in  $\xi$  coordinates. All axes are in unit of *template diameters*, width of the projection of the template isosurfaces in the various  $\xi_i$  degrees of freedom. The left most panel compares the template bank distribution in the two most “thickest” degrees of freedom. The middle and right panels show the distribution in the less thick degrees of freedom. This shows that this coordinate system effectively “flattens” out the higher dimensions, which simplifies the placement of a geometric template bank. These images are copied from [62] the caption is paraphrased from the same source.

$$\gamma_{\alpha\beta} = \frac{1}{2} (\mathcal{J}(\psi_\alpha\psi_\beta) - \mathcal{J}(\psi_\alpha)\mathcal{J}(\psi_\beta)) \quad (2.13)$$

$$\mathcal{J}(a(x)) = \frac{1}{I(7)} \int_{x_L}^{x_U} dx \frac{a(x)x^{-7/3}}{S_N(xf_0)} \quad (2.14)$$

$$\mathcal{I}(q) = \int_{x_L}^{x_U} dx \frac{x^{-q/3}}{S_N(xf_0)} \quad (2.15)$$

$$\psi_0 = 2\pi f_0 x \quad (2.16)$$

$$\psi_i = x^{(i-5)/3} \quad (2.17)$$

$$\psi_{iL} = x^{(i-5)/3} \log(x) \quad (2.18)$$

Fourth, the eigenvalues  $E_i$  and eigenvectors  $V_i$  of  $g_{ij}$  are calculated and in order to rotate into an orthonormal coordinate system. In these new coordinates the space is Cartesian and the metric will trivially be the identity matrix.

$$\mu_i = \sum_j (V_i^j \sqrt{E_i}) \lambda_j^{(\mathbf{F}^2)} \quad (2.19)$$

Finally, the goal of this coordinate system is to construct a set of coordinates that flatten out the parameter space and to identify the most important degrees of freedom of the bank. By rotating the coordinates into an orthonormal eigenbasis of the original matrix, it becomes possible to calculate the most important degrees of freedom for template placement via a Principle Component Analysis (PCA) of a large number of possible values for  $\mu_i$ .

$$\xi_i = \sum_j C_{ij} \mu^j \quad (2.20)$$

Where  $C_{ij}$  is the covariance matrix of the eigenvectors  $V_{ij}$ . While these  $\xi_i$  coordinates are no longer Cartesian, but the template bank is now “thin” for higher values of  $i$ . Therefore it is sufficient to only use the dominant directions  $\xi_1, \xi_2, \xi_3$  to construct template bank lattices.

`pycbc_geom_aligned_bank` is capable of generating both two dimensional and three dimensional lattices utilizing  $\xi_1, \xi_2$  and  $\xi_1, \xi_2, \xi_3$  respectively. Currently, the procedure for generating  $A_2^*$  (hexagonal) lattices is similar to the steps outlined in [84]. In this method, brute force is required to check that the gravitational waveforms corresponding to each lattice point are valid.

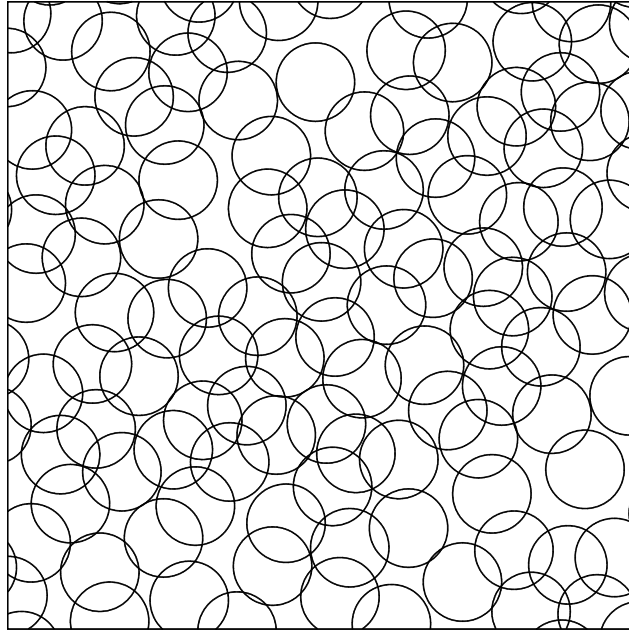


Figure 2.3: An example of a two dimensional stochastically generated distribution of templates. Each black circle corresponds to the region of parameter space covered by an individual template. This distribution is inefficient at recovering templates since these template isosurfaces overlap, and there are under-covered regions of the parameter space between template isosurfaces. This image is taken from [120].

Work is on going to replace this algorithm with the more computationally efficient method for generating lattices that I outlined earlier in this section [268]. In theory you could generate higher dimensional lattices using the remaining higher order  $\xi_i$ , but the template bank parameter space becomes increasingly thin in these higher dimensions and the gain would be negligible at the cost of increasing the complexity of the template bank placement algorithm (see Figure 2.2). For parameter spaces with more than 9 degrees of freedom  $A_N^*$  are no longer the most efficient method for template bank construction [179].

## 2.2 Stochastic placement algorithm

The stochastic bank placement algorithm is particularly useful for NSBH and BBH regions of the LIGO-Virgo template bank<sup>6</sup>. Higher mass systems have ISCOs that are under the Earth bound laser interferometer sensitivities, and inspiral-merger-ringdown models must be used to place these templates. Since there is currently no know analytic expression for the underlying metric for these waveforms, the geometric method (see Section 2.1) cannot be implemented.

The basic idea of the stochastic placement algorithm is to place templates from a random *proposal distribution* of signals such that one template has a mismatch above a threshold minimal match with any other template previously accepted into the bank. This method is generally applicable to arbitrary proposal distributions because it does not require prior knowledge of the underlying mismatch metric of the target parameter space. However, it is typically less efficient than geometric methods since stochastic banks require more templates to achieve the

---

<sup>6</sup>Legal disclaimer: “The content and text presented in this section are taken from [146, 137, 124, 33, 223] with minor paraphrasing and alterations. The use of these materials is protected under ‘Fair Use’ (UrhG §24,70,63) and consistent with the requirements of § 6 Abs. 1 PromO.”



same coverage of a geometric bank over the same parameter space (see Figure 2.3). As more parameters are required to describe the targeted signals, the efficiency of stochastic methods become competitive with that of geometric methods [179].

In general, stochastic template banks are populated using the following steps (however the terminating *convergence condition*, the point at which the placement terminates, varies depending on the application). The starting point for a stochastic placement could either be an empty template bank or an existing “seed” template bank [137, 45, 176].

1. Propose a physically viable point in parameter space  $p$  following some probability distribution (we call this distribution the *proposal distribution*). If we are starting with an empty bank, then the first proposed point will always be accepted.
2. Calculate the match of the waveform at  $p$  with all the waveforms previously accepted into the bank.
3. Append the candidate to the bank if all the matches are below some threshold, known as the *minimal match*. We shall take the minimal match to be  $MM=97\%$ .
4. Repeat the previous steps until a convergence condition is achieved. For example, a good convergence criteria could be based on the number of template candidates accepted per fixed batch of candidates: continue the process until, only 30 or fewer points have been accepted per batch of 1,000 candidates.

Upon reaching the convergence condition, the template bank is deemed *saturated* or equivalently that the template bank *covers* the targeted parameter space.

The rate of convergence of the stochastic method will depend on the proposal distribution. As long as the proposal distribution spans the entire parameter space, the stochastic placement algorithm is guaranteed to *converge* (achieve its *convergence condition*). In the worst case scenario for template banks with an arbitrarily high number of templates, the convergence of a stochastic placement is an  $N^2$  problem derived from the fact that each new template candidate must be compared with all previous templates placed in the bank.

$$\text{number of template candidates compared} \propto \lim_{N \rightarrow \infty} \sum_{i=0}^N i = \int_0^N x dx = \frac{N^2}{2} \quad (2.21)$$

If the proposal distribution is weighted to attempt to place less templates regions of the bank that require relatively more templates to be saturated, the stochastic method will take longer to converge. There could be regions of the parameter space which require more templates to describe less astrophysically likely CBC systems. Supplied with an *a priori* sufficiently reliable astrophysical estimate of the underlying CBC population it is possible to tailor the template bank proposal distribution in a more appropriate manner. However, in the absence of any such prior information, it is necessary to apply some other criteria for the proposal distribution. A well motivated choice to speed up the convergence of the stochastic method is to choose the proposal distribution according to the value of the determinant of the metric  $g_{ij}$  (this was the choice made in [179]).

## Sbank

The `lalapps_cbc_sbank` (Sbank) algorithm is a PyCBC and LALSuite [197, 124, 33, 223] parallelizable adaptation of the stochastic method. In each instance Sbank is applied, a CBC template bank is generated for a pre-specified range of aligned-spin, non-spinning, or precessing CBC parameters.

Sbank requires the user to specify the range of component masses, the range of component mass spins, the waveform approximant, the frequency cut-offs and the PSD to generate their template bank. Unless specified otherwise, all template placements require the explicit calculation of mismatches.

There is an option to use an analytic metric approximat [206, 207] (see Eq. 1.65) to speed up mismatch calculations between template candidates that have a large Mchirp,  $\mathcal{M}$ , difference. This approximant has been shown to be comparable to the actual mismatch value for aligned spin systems [207, 33, 223]. Figure 2.4, compares the values returned by the analytically calculated approximant of the match and the actual match (i.e. the *overlap*) between one million pairs of two arbitrarily chosen face-on precessing NSBH waveforms [upper row] and also a separate study of 10,000 pairs of aligned spin BNS waveforms [bottom row]. For small deviations in  $\mathcal{M}$  in the aligned spin parameter space, the metric approximant diverges parabolically, thus it will return unphysical values (i.e. negative match values) for pairs of waveforms that have an overlap less than 70%. For the face-on precessing parameter space, I found no instances where the approximat returned a higher value of the overlap when the overlap was greater than 97%, the typical minimal match threshold. While this approximant is not exact for arbitrary waveforms, the stochastic algorithm only needs to have accurate mismatch values that are near the user specified maximal mismatch. Since the use of the approximant is relegated to distant templates, its application will not result in under-saturating the template bank; the actual mismatch will still be calculated for signals that match above the approximant threshold. The stochastic algorithm is not sensitive to how much a signals match is under the MM, it will accept signals with fitting factors under the MM regardless of the exact value. Therefore, it is not necessary to explicitly calculate the overlap for each mismatch calculation which saves computational resources.

Sbank is particularly useful for generating template banks with large numbers of templates. In these cases, Sbank is called by the `pycbc_create_sbank_workflow` [197] to parallelize and speed up the template placement with the help of a high throughput scientific computing cluster (e.g. `Atlas` [9]). The Sbank workflow functions by first applying a *coarse* (an intentionally under covered) template placement over the entire bank. After the initial coarse placement, the bank placement is parallelized. These subsequent parallel placements are implemented in *cycles*. The user specifies how many parallel template banks are placed simultaneously per cycle over the subspaces of the parameter space divided in the chirp mass,  $\mathcal{M}$ , degree of freedom. The user must also specify how many template candidates are proposed and how many can be accepted before one of the subspace template placements terminates. Once all parallel placements terminate, the cycle finishes and the templates are combined into one bank file. This combined file is split up again to seed the next cycle of parallel template placements. The user specifies how many cycles are conducted, and on the last cycle, Sbank returns the final combined converged bank.

One consequence of parallelizing the stochastic algorithm is that it has a tendency to over-saturate the parameter space. The over-saturation arises because each individual placement does not consider the templates placed in neighboring placements. The result is that two or more neighboring templates will attempt to place the same template, when only one template would be needed if the algorithm was not parallelized. These templates tend to accumulate at the borders of each individual template placement forming dense regions called *gridlines* (see Chapter 3.2). The purpose of the coarse initial non parallelized placement in Sbank, is to mitigate the effect of these gridlines, however it does not eliminate them completely.

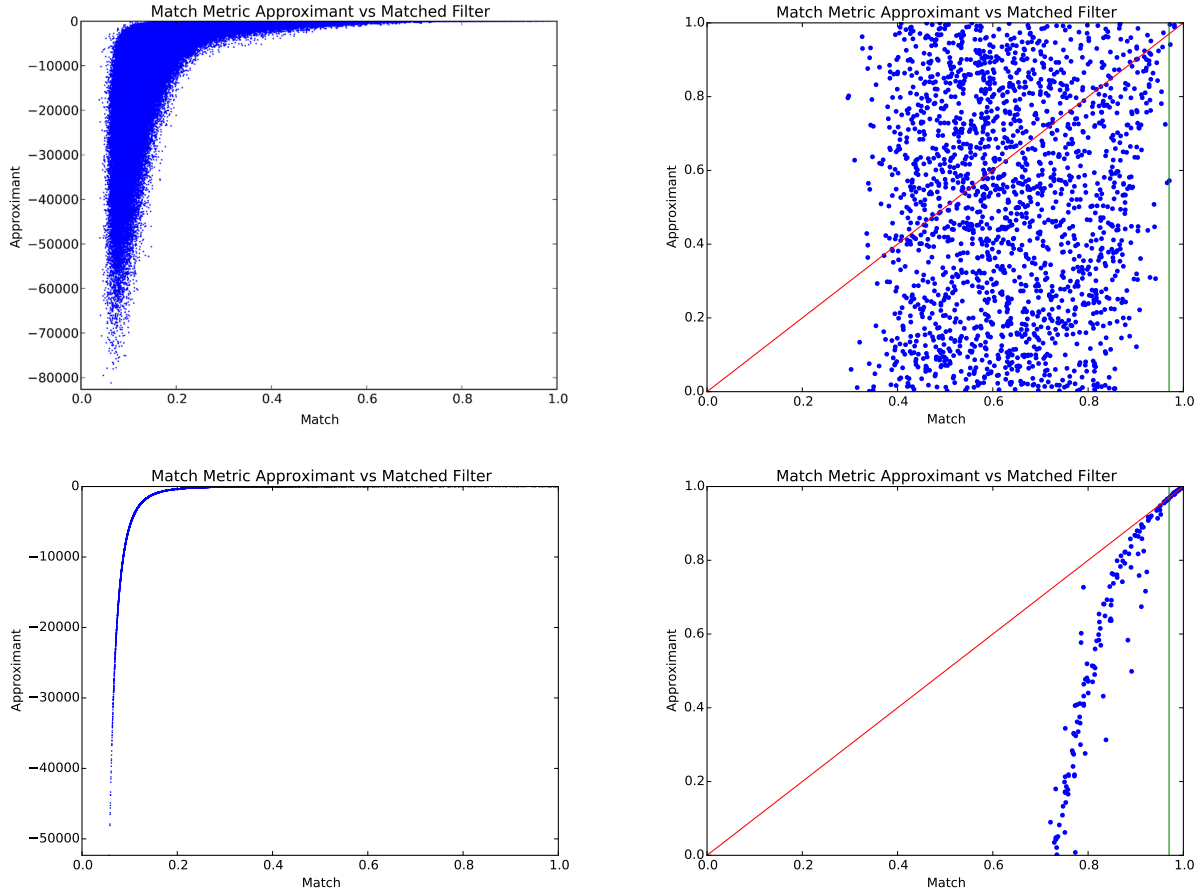


Figure 2.4: Comparison of the match metric approximant implemented in Sbank and the real match. The top row shows the correlation between the match value returned by the approximant vs. the actual match obtained by calculating the matched filter between one million pairs of randomly selected face-on precessing signals. The upper right panel, is a closeup of the regime of the top left panel where physical values for the approximant mismatch are returned. The bottom row shows the same regions as the top row for a different study of 10,000 waveform pairs in which I show that the approximant diverges parabolically for aligned spin BNS systems for small perturbations where only the component masses are allowed to vary. The red lines in the panels in the right column indicate where the approximant agrees with the actual match value. The region of the plots in the right column to the left of the green line indicate waveform comparisons where the actual matched filter value is above the minimal match threshold, but the approximate returns a lower value.

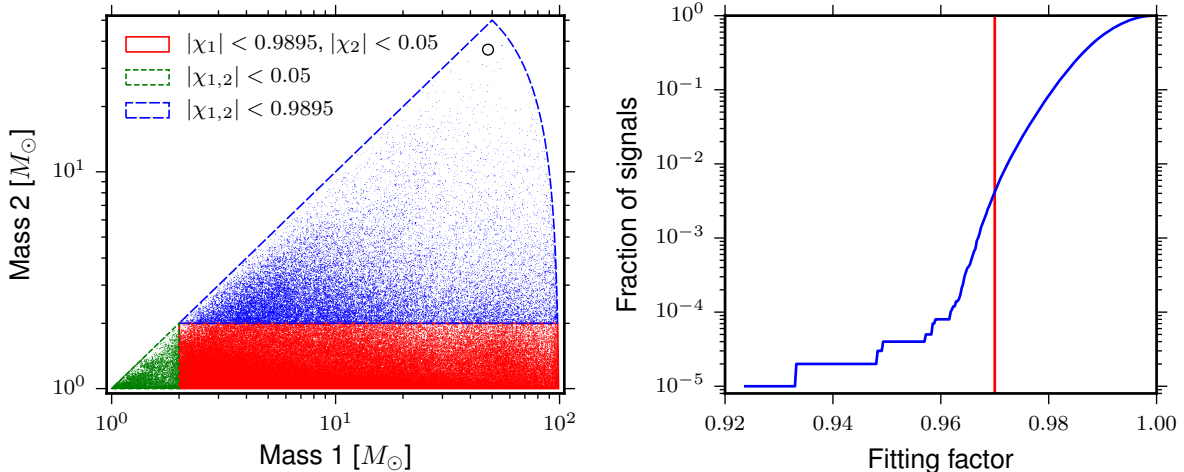


Figure 2.5: The left panel is a scatter plot of the component mass parameter space used in the construction of Uberbank, the template bank implemented in the first detection era of LIGO-Virgo. The blue region indicates the binary-black-hole region of the parameter space. The green region indicates the binary-neutron-star region of the parameter space. The red region indicates the neutron-star-black-hole region of the parameter space. The right panel is a plot of the recovered fitting factors obtained from a banksim of Uberbank with  $10^5$  injected signals. This demonstrates that less than 1% of injected signals had a matched-filter SNR loss greater than 3%. These images are taken from [15] and the captions are paraphrased from the same source.

## 2.3 Hybrid methods

In the first two LIGO-Virgo detection eras (O1 and O2), CBC template banks were constructed via a combination of stochastic and geometric placement algorithms<sup>7</sup>. In O1, two template banks were independently implemented in the PyCBC [197, 255] and GstLAL [69, 180] detection pipelines. The first O1 PyCBC template bank (the so-called *Uberbank* [15] plotted in Figure 2.5) totaled 250,000 templates and searched for aligned-spin BNS, NSBH, and BBH systems in the mass range  $M_{total} \in \{2M_{\odot}, 100M_{\odot}\}$  using a minimal match of 97%. A second template bank was constructed for the purposes of searching exclusively for aligned-spin BBH systems in the mass range  $M_{total} \in \{50M_{\odot}, 600M_{\odot}\}$ <sup>8</sup>. This bank over covered the low mass ratio region of the search parameter space where BBH had been found in O1. Thus the minimal match for the  $q < 3$  BBH region used a 98% minimal match, the BNS region used a 97% minimal match, and the remaining regions used a 96.5% minimal match slightly under covering this region of the bank in order to reduce the total templates in the template bank. Utilizing two template banks with an overlapping mass range proved to be problematic when estimating the statistical significance of GW triggers, therefore in O2 one PyCBC template bank (the so-called *Hyperbank* plotted and tested in Figures 2.6 and 2.7) was implemented that totaled 399,995 templates and covered the aligned-spin mass range  $M_{total} \in \{2M_{\odot}, 500M_{\odot}\}$  [89].

<sup>7</sup>Legal disclaimer: “The content and portions of the text presented in this section are taken from [70, 15, 89] with minor paraphrasing. The use of this material is protected under ‘Fair Use’ (UrhG §24,70,63) and consistent with the requirements of § 6 Abs. 1 PromO.”

<sup>8</sup>The justification for splitting up the search parameter space in this way was that at the time high mass CBC signals were not as well understood relative to the signals from lower mass signals and it was desirable to treat these signals separately.

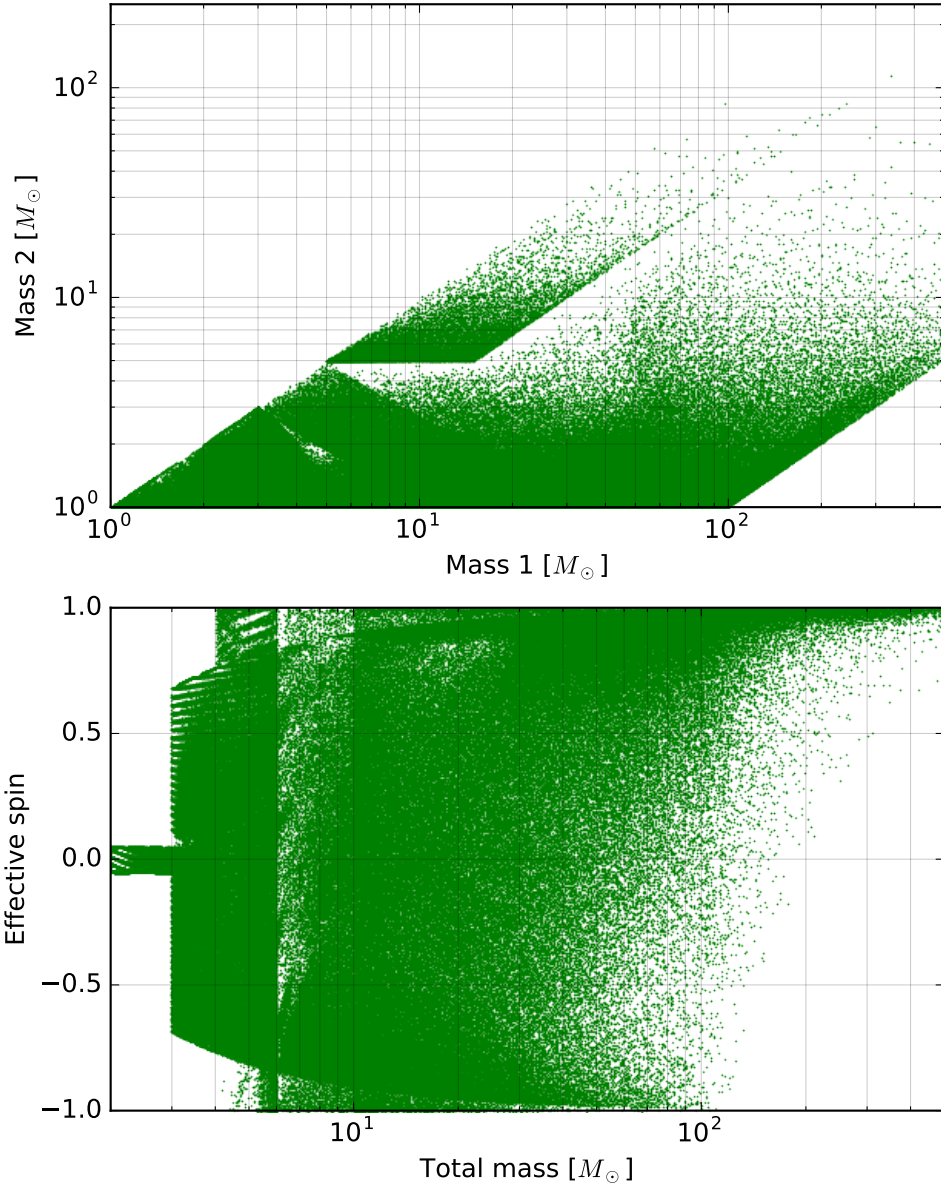


Figure 2.6: Two scatter plots of Hyperbank, the template bank implemented in the O2 search. Each green dot represents a single template in the bank. In the top panel, the component masses of the templates in the template bank are plotted. In the bottom panel, the effective spin and total mass associated with the templates in the template bank are plotted. Template banks constructed with hybrid methods like those use to make this bank are inefficient and have artificially uneven template distributions. Image is taken from [89] and the caption is paraphrased from the same source.

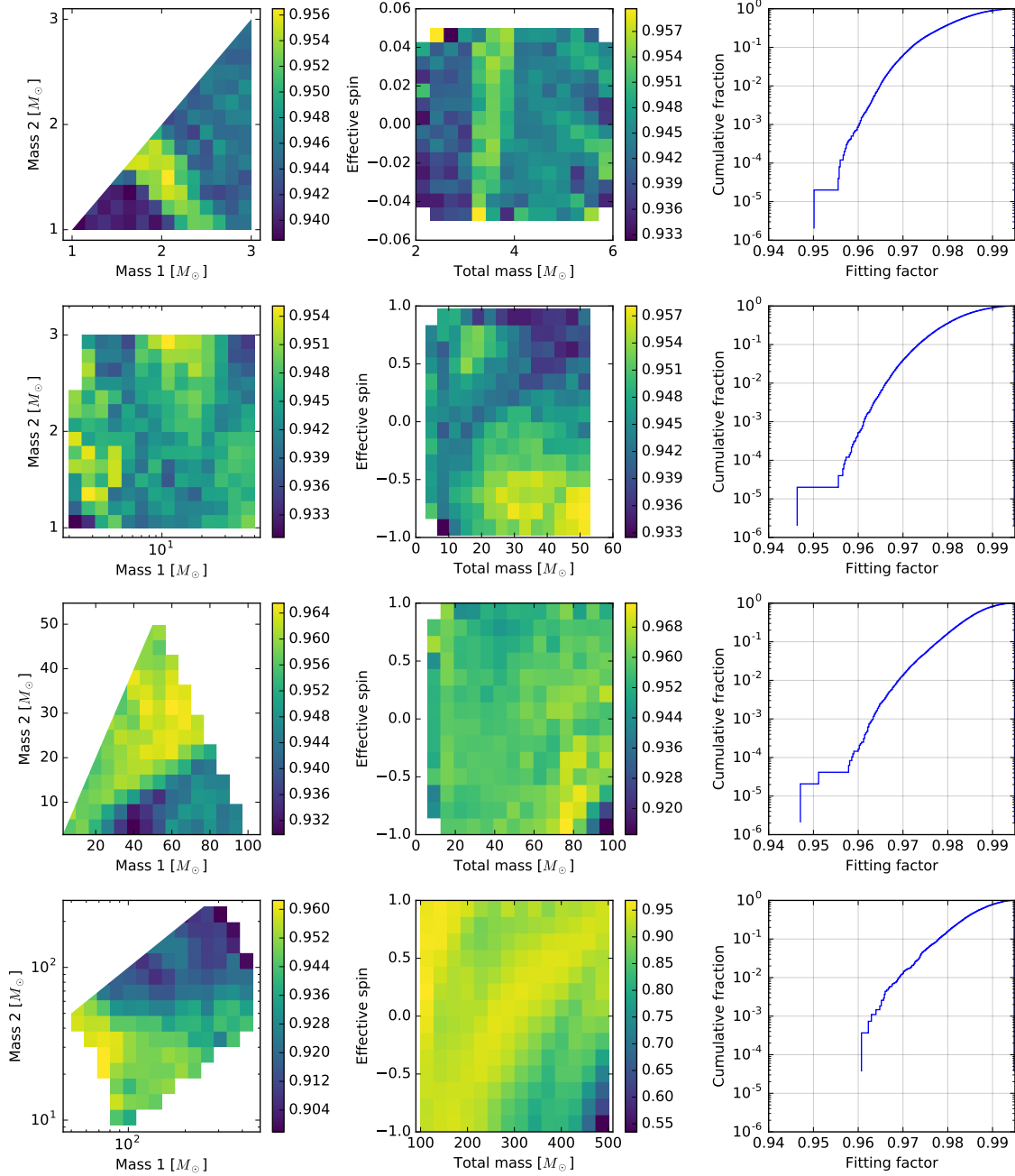


Figure 2.7: Plot of the recovered fitting factors obtained from several banksims of Hyperbank. Each row represents a single focused banksim study of  $5 \times 10^4$  injected signals on various subspaces of Hyperbank: BNS (top), NSBH (second row), low mass BBH (third row) and high mass BBH (bottom). The first two columns are heat maps indicating the distribution of fitting factors on the subspaces plotted in component masses and effective spin-total mass coordinates. The last column shows the cumulative histogram fitting factor distribution for the injected signals into each region. For the BNS region, an inspiral only PN model was used for injections. For all other regions an EOB model was used. Image is taken from [89] and the caption is paraphrased from the same source.

The following parameters differ between these banks:

1. the mass and spin range of the proposal distributions,
2. the detector PSD noise curve,
3. the gravitational waveform model for the CBC systems,
4. the effectualness, quantified by the maximum fractional loss in sensitivity range due to the discrete coverage of the search parameter space with a finite number of waveforms [91],
5. and finally the low frequency cutoff,  $f_{low}$ , for the matched filter.

In O1, the **TaylorF2** waveform model was implemented in the BNS region of the bank (more specifically systems with total mass under 6) since these longer duration signals have over 99% of the power radiated during the inspiral portion of the coalesces and the LIGO-Virgo detectors have poor sensitivity beyond the merger [89]. The **TaylorF2** waveforms terminated at ISCO<sup>9</sup> and included orbital terms up to 3.5 PN order and spin related corrections up to 2.5 PN order [40]. For all other regions **EOB** was used [249]. The starting frequency for all templates was set to 30 Hz.

In the O2 template bank, both the orbital and the spin correction terms for the **TaylorF2** waveforms were expanded to 3.5 PN order [58]. The starting frequency of templates were allowed to vary across the parameter space. Under 20 Hz, the PSD noise is too high to be worth searching for signals [89]. The expected signals from higher mass systems are shorter in duration and it makes sense to lower the frequency cutoff. The frequency cutoff is determined by comparing the match of a template against itself for a reference frequency 15 Hz under the lowest allowable frequency supported by the PSD. The idea is to compare the amount of signal lost relative to an idealized frequency range.  $f_{low}$  is selected such that only 0.5% of the signal can be lost relative to an ideal search at the lower frequency cutoff.

$$\frac{\int_{f_{low}}^{f_{high}} df \frac{|\tilde{h}(f)|^2}{S_n(f)}}{\int_{15 \text{ Hz}}^{f_{high}} df \frac{|\tilde{h}(f)|^2}{S_n(f)}} = 0.995 \quad (2.22)$$

Both hybrid banks were constructed by covering the BNS region of the bank with a geometric lattice constructed with the **TaylorF2** metric, and covering the entire mass range ( $2M_{\odot} < M < 100M_{\odot}$ ) stochastically [70]. This hybrid approach has previously been proven to reproduce the effectualness of a purely stochastically placed BBH bank in the mass range  $M_{total} \in \{50M_{\odot}, 600M_{\odot}\}$  with approximately 5% fewer templates [70]. The geometric **TaylorF2** lattice will cover most of these relatively lower mass systems even when searching for inspiral-merger-ringdown signals because the LIGO-Virgo detectors are not very sensitive to the strains produced by the merger-ringdown portion of BNS gravitational waves. This region is also the most densely populated region of the bank. Heavier BBH systems will have a merger-ringdown at lower frequencies therefore a geometric lattice built from inspiral only waveforms will be inaccurate. For these systems stochastic placement or a lattice built from a full inspiral-merger-ringdown metric is needed to cover the space.

The hybrid banks implemented in the O1 and O2 searches have a tendency to produce *gridlines* (artificially dense regions of over-coverage), or other discontinuities in template density which over-saturate the parameter space. The next three chapters 3 and 4 focus on studying how to remove these gridlines.

---

<sup>9</sup>It is worth noting that in GstLAL searches a cutoff frequency of 1024 Hz was used.

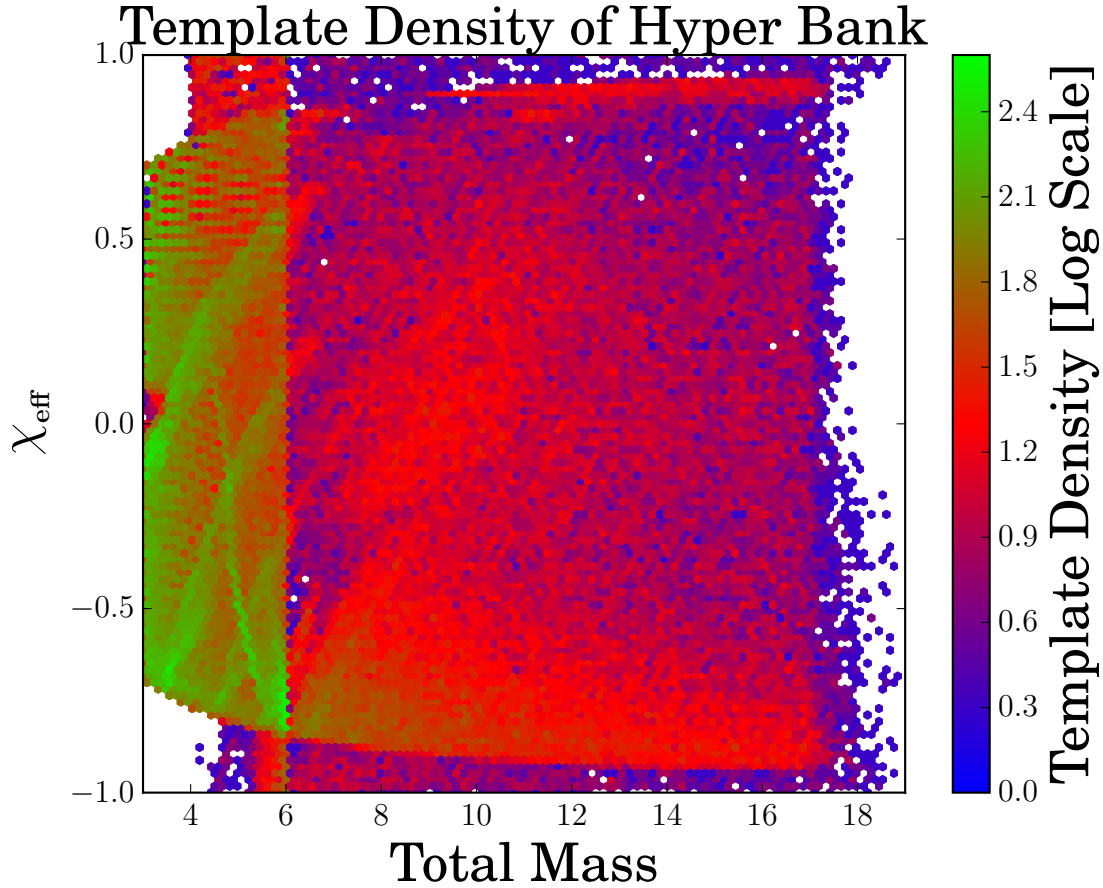


Figure 2.8: Density plot of the 234,259 templates in NSBH region ( $M_{BH} = 2 - 16M_{\odot}$  and  $M_{NS} = 1 - 3M_{\odot}$ ) of Hyperbank (out of a total number of 399,995), the template bank implemented in the O2 search. Template densities are color coded logarithmically according to the template density in each uniform cell unit. Each cell unit has dimensions  $\delta M = 0.16M_{\odot}$  and  $\delta\chi_{\text{eff}} = 0.02$ . The cells in the green lines (gridlines) are over 100 times denser than the blue cells. The data for this plot was taken from [89].



## Template Density of a Geometric Bank

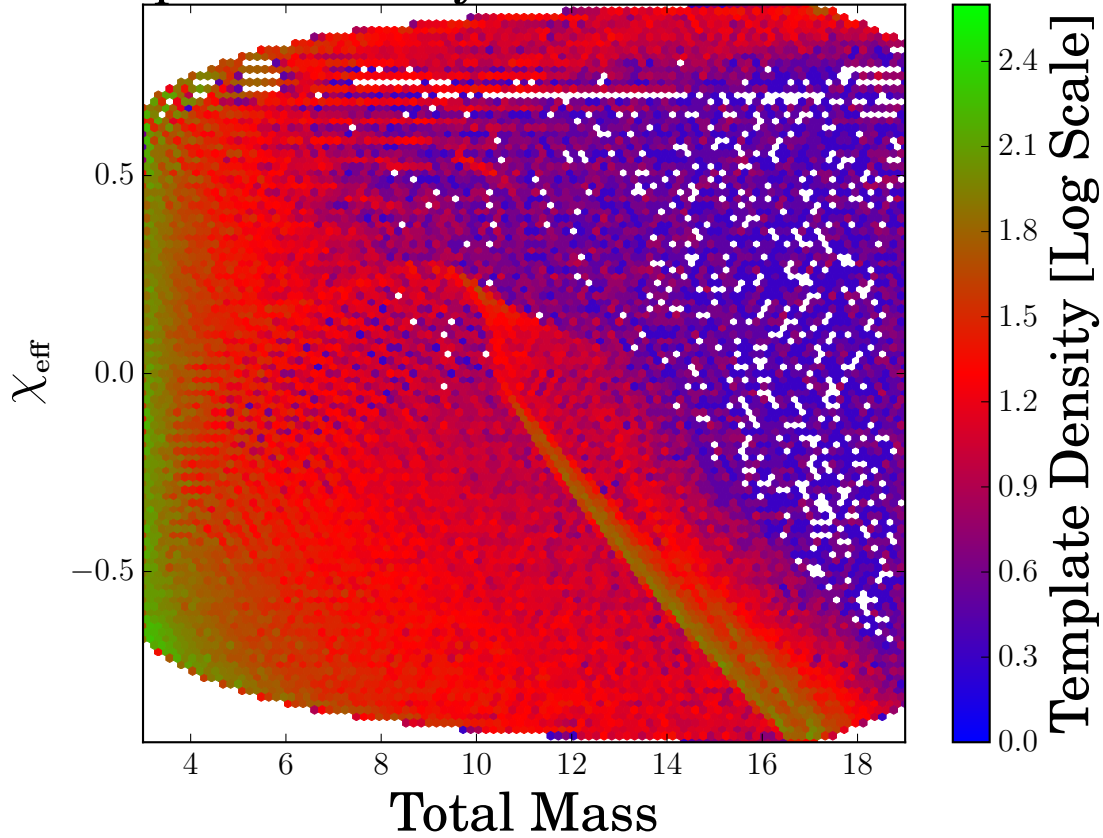


Figure 2.9: Density plot of the 174,000 templates required to generate a NSBH ( $M_{BH} = 2 - 16M_{\odot}$  and  $M_{NS} = 1 - 3M_{\odot}$ ) geometric bank utilizing the two dimensional geometric lattice setting of `pycbc.geom.bank`. Template densities are color coded logarithmically according to the template density in each uniform cell unit. Each cell unit has dimensions  $\delta M = 0.16M_{\odot}$  and  $\delta\chi_{\text{eff}} = 0.02$ . Unlike `Sbank` (see Figure 2.10), the template density does not vary monotonically suggesting that it is not the optimal template bank distribution for this parameter space. See Chapter 4 for details.

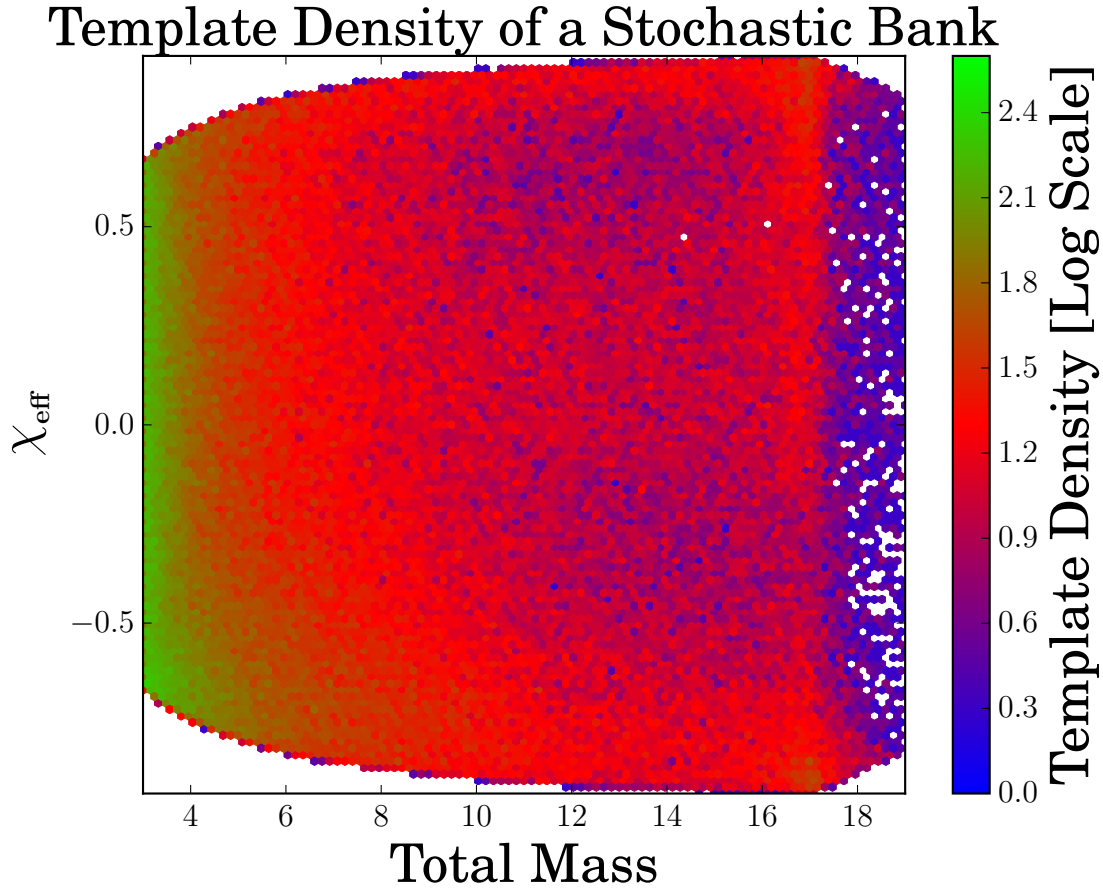


Figure 2.10: Density plot of the 220,000 templates required to generate a NSBH ( $M_{BH} = 2 - 16M_{\odot}$  and  $M_{NS} = 1 - 3M_{\odot}$ ) stochastic bank utilizing Sbank. Template densities are color coded logarithmically according to the template density in each uniform cell unit. Each cell unit has dimensions  $\delta M = 0.16M_{\odot}$  and  $\delta\chi_{\text{eff}} = 0.02$ . Unlike Hyperbank and the two dimensional geometric lattice (see Figures 2.8 and 2.9), the template density varies monotonically and there are no apparent gridlines. See Chapter 4 for more details.

## CHAPTER 3

# CONSTRUCTING A FACE-ON PRECESSING NSBH TEMPLATE BANK

Binary systems consisting of neutron-stars and black-holes are key targets for the present generation of gravitational wave detectors such as Advanced LIGO [12] and Advanced Virgo [29]<sup>1</sup>. The template bank implemented in the O1 and O2 detection eras for the LIGO Livingston and Hanford detectors were constructed over the parameter spaces containing compact binaries with aligned spin and total mass less than  $100M_{\odot}$ . This parameter space was approximated in [88, 90] to sufficiently cover the anticipated population of face-on precessing NSBH systems. Searches for these events *a priori* cover a wide range of masses and spin magnitudes, but use only waveforms for which the spins of the individual compact objects are assumed to be completely aligned or completely anti-aligned with the orbital angular momentum [15]. Misalignment between the spin and orbital angular momentum can the orientation of the orbital plane to evolve with time. This precession dynamic modulates the gravitational waveforms [38]. While follow-up studies for accurate parameter estimation do include precession [28, 27, 28], including these waveforms directly in the initial search pipelines is challenging; the dimensionality of the parameter space to be searched is increased, implying a significant increase in the total number of templates. To calculate how many templates would be required to cover the face-on precessing parameter space we utilized the stochastic placement algorithm to construct the bank.

Specifically, we focused on neutron-star–black-hole (NSBH) systems, but we expect that our method would apply to other source systems as well. We consider a subspace NSBH binaries with a black-hole of mass  $M_1$  and a neutron-star mass of  $M_2$  such that  $2M_{\odot} < M_1 < 16M_{\odot}$ , and  $M_{\odot} < M_2 < 3M_{\odot}$ <sup>2</sup> Since neutron-star spins are expected to be small we ignore them, but the black-hole spin will be allowed to take any magnitude which is meaningful in the Kerr metric [154, 193, 192] and any direction [171]. We used the frequency domain waveform model presented in [174]. This waveform model does not contain the merger and ringdown portions. For the sensitive frequency ranges of O1 and O2, the inspiral portion of the waveform in this CBC parameter subspace had the largest contribution to the signal-to-noise ratio. Thus, the

---

<sup>1</sup>Legal disclaimer: “The content and text presented in this chapter is copied with minor alterations (i.e. the addition of Figure 3.10) from a publication I wrote with co-authors Haris MK, Tito Dal Canton, Henning Fehrmann, Badri Krishnan, Andrew Lundgren, Alex B. Nielsen and Archana Pai [146]. The use of these materials is protected under ‘Fair Use’ (UrhG §24,70,63) and consistent with the requirements of § 6 Abs. 1 PromO.”

<sup>2</sup>While we know larger black-holes do exist, the additional degrees of freedom required to describe precession dramatically increase the size of the bank. In order to mitigate the computational cost for constructing the bank we chose this smaller NSBH subspace as a proof of concept for this new method of template bank construction.

merger and ringdown phases was not important for our purposes. However, the methods used in our study should be useful for higher mass systems, where merger effects are more important.

Within a previously implemented neutron-star–black-hole regime of the aligned-single-spin neutron-star–black-hole template bank, (a.k.a. the Aligned-Spin-Bank (ASB)), parameter space 150,000 binary inspiral templates were placed [88, 90]. The template placement in this ASB parameter space was split up utilizing the Sbank [137] algorithm (see Section 2.2), which at the time split the parameter space into parallel segments with regard to  $\mathcal{M}_C$  (see Eq. 1.22)<sup>3</sup>. Splitting in one dimension sufficiently reduced the computation time required to cover the three dimensional aligned-single-spin neutron-star–black-hole (NSBH) parameter space, however the construction of a five dimensional face-on precessing NSBH template bank was computational prohibitive utilizing the same cell splitting scheme for the ASB NSBH bank. Therefore we transformed the proposal distribution such that template candidates were uniformly selected in the two chirp time coordinates (see Section 1.1.5)  $\{\tau_0, \tau_3\}$  [88, 90, 63, 62, 137] that flatten out the ASB. We subsequently parallelized the over all template bank placement using uniform “cells” split along these two chirp time coordinates.

For searches based on matched filtering with modeled waveforms, the traditional method of constructing a template bank was to use the parameter space metric [207, 97] for determining the spacing between adjacent templates. This method has been successfully used to search for non-spinning systems [84] and has also been applied to aligned-spin systems [62, 138]. For precessing waveforms however, the parameter space metric has not yet been sufficiently well understood for it to be directly used to place templates. The main issue is that in order to place a lattice of templates, one needs a coordinate system on the parameter space where the metric is explicitly flat. As was discussed mentioned in Section 2.2, in situations where such geometric template placement methods are not available, stochastic methods are commonly employed [137, 45]. This also includes the most recent searches over the first Advanced LIGO observing run [15, 14].

The most effectual implementation of a stochastic NSBH template bank constructed to date [136] required approximately 1.6 million templates, assuming the detector to be in the “early Advanced LIGO” configuration [11]. This construction used a new detection statistic based on maximizing the signal-to-noise ratio (SNR) over source locations in the sky and required a minimal match criteria of 90% when comparing each proposed template with previously accepted ones, as opposed to the more conventional 97%. Using the conventional 97% value would lead to a much larger number of templates. Moreover, as the detector improves its low frequency sensitivity over the next few years, the number of templates increases further. The method used in this paper could be used to deal with both of the above issues. We used the conventional 97% minimal match value and, for simplicity, we used the conventional SNR rather than the detection statistic introduced in [136], but we expect that our method can be adapted to that detection statistic as well.

In this chapter, we discuss the methodology of how stochastic methods can be applied to cover the space of precessing waveforms. We chose to built our bank using face-on/off precessing signals because these systems will be, on the average, more luminous than edge-on systems and thus more likely to be detected [90] and the inspiral portion of the waveform produced by this subspace of CBC systems can be modeled by the computationally efficient frequency domain **SpinTaylorF2** model [174, 168](see Section 1.1.4). The main computational problem we faced was that for every proposed template, one typically compares it with *all* previously accepted templates to decide whether or not it should be accepted. We saw that with an appropriate choice of coordinates, it is possible to break up the parameter space into smaller regions, and treat each region independently.

---

<sup>3</sup>This bank utilized **TaylorF2** waveforms with 3.5 PN non-spinning phase corrections [55, 53] and 2.5 PN spinning phase corrections [87, 40, 156, 52] (see Section 1.1.4).

### 3.1 Cell splitting methodology

Building a template bank for arbitrary orientations of total angular momentum was too computationally expensive for our algorithm to build at the time. Therefore we started with the assumption that the binary system was face-on, i.e.  $\mathbf{J}$  was pointing either directly towards or directly away from the detector and we fixed the sky-location to be directly overhead the detector (see Section 1.1.6). With these assumptions, we were left with a five dimensional problem: the two masses  $M_1$  and  $M_2$ , and the three components of the black-hole spin  $\mathbf{S}$ .

Even with these assumptions, constructing this face-on precessing template bank was a significant computational challenge. An important issue was that the stochastic placement algorithm was not easy to parallelize. Imagine trying to divide the full parameter space into smaller sub-regions (“cells”) and applying the stochastic template placement procedure outlined in Section 2.2 (reproduced below) in each of these sub-regions.

1. Propose a physically viable point in parameter space  $p$  following some probability distribution (we call this distribution the *proposal distribution*). If we are starting with an empty bank, then the first proposed point will always be accepted.
2. Calculate the match of the waveform at  $p$  with all the waveforms previously accepted into the bank.
3. Append the candidate to the bank if all the matches are below some threshold, known as the *minimal match*. We shall take the minimal match to be  $\text{MM}=97\%$ .
4. Repeat the previous steps until a convergence condition is achieved. For example, a good convergence criteria could be based on the number of template candidates accepted per fixed batch of candidates: continue the process until, only 30 or fewer points have been accepted per batch of 1,000 candidates.

Note that stochastic placement algorithm requires checking the match of a new waveform with *all* of the previously accepted waveforms in the template bank. Thus, in principle, each sub-region need to be aware of the points that have been accepted in the other sub-regions. Dealing with each sub-region independently could have led to a significant over-coverage, i.e. accepting many more points than necessary.

If we found sub-regions which were uncorrelated from each other (by a suitable choice of coordinates) and if the sub-regions were sufficiently large, then the parallelization would be close to optimal. While we did not have the optimal coordinates for this purpose, it turns out that a simplified version of the so-called *chirp times* ( $\tau_0, \tau_3$ ) [237, 88] are a good approximation:

$$\tau_0 = \mathcal{M}^{-5/3} \tag{3.1}$$

$$\tau_3 = \mathcal{M}^{-2/3}(\nu(1 - \nu))^{-3/5}(4\pi - \beta_C) \tag{3.2}$$

where<sup>4</sup>

$$\beta_C = \frac{1}{12}(38\nu^2 + 75\nu)\chi^\parallel. \tag{3.3}$$

The chirp time was first introduced in [233] as the time taken for the gravitational wave signal to reach coalescence starting from some initial frequency. Chirp times were also the coordinates typically used in geometric methods for template placement [84] and were also the coordinates where the parameter space metric for binary inspiral systems was most easily understood (see e.g. [152]).

---

<sup>4</sup> $\beta_C$  should not to be confused with the opening cone angle (see Eq. 1.34).

We wanted to cover the  $(\tau_0, \tau_3)$  space uniformly. In particular, while constructing the template bank for a particular rectangular region, we wanted to ensure that we generated templates only for that rectangular region. If we were to pick values of  $M_1, M_2, \mathbf{S}$  directly, this would not be guaranteed. We therefore followed these steps (the notation in this section was first introduced in Section 1.1.6).

1. Generate values of  $\tau_0$  and  $\tau_3$  randomly within the rectangular region under consideration following a uniform distribution.
2. The value of  $\tau_0$  determines the chirp mass  $\mathcal{M}$ , but  $\tau_3$  depends on both  $\nu$  and  $\chi^\parallel$ . Our strategy was to then pick a value of  $q$  which, along with the chosen value of  $\tau_3$  determined  $\chi^\parallel$ . The value of  $\nu$  was chosen randomly assuming that  $M_1$  and  $M_2$  were uniformly distributed in their allowed ranges. In practice, we drew random values of  $M_1$  and  $M_2$  from uniform distributions, which determined  $\nu$ . Given  $q$  and  $\tau_3$ , we solved Eq. (3.2) for  $\chi^\parallel$ .
3. To fix the component of  $\mathbf{S}$  perpendicular to  $\hat{\mathbf{L}}$ , we note that the total spin magnitude  $\chi$  was bounded below by  $\chi^\parallel$ . We picked a value of  $\chi^\perp$ , such that  $|\chi|$  was uniformly distributed between  $\chi^\parallel$  and 1.
4. Finally, we chose an azimuthal black-hole spin angle  $\alpha_0$  uniformly between 0 and  $2\pi$ .

This procedure ensured that the proposal distribution covered all possible precessing binary configurations. Lower values of  $\tau_3$  were mapped to the more aligned systems, i.e. larger values of  $\chi^\parallel$ , while lower values of  $\tau_0$  were mapped to systems with higher total mass,  $M$ . While the resulting distribution of points in the physical parameters  $(M_1, M_2, \chi^\parallel, \chi^\perp, \alpha_0)$  were not completely physical, our final results were not very sensitive to this choice of distribution.

## 3.2 The precessing face-on template bank (FOB)

The total range of chirp times corresponding to our parameter space was broken up into 938 smaller “chirp time cells”. A stochastic template bank was constructed for each cell independently and the 938 template banks were then concatenated. Parallelizing the stochastic placement is computationally advantageous, because the stochastic placement algorithm’s efficiency scales with the square of the number of templates placed [62, 138]. By splitting up these regions, we limited the number of comparisons needed for each stochastic template bank candidate to decide whether it should be accepted or not. However, speeding up the algorithm came at the cost of over-coverage between neighboring cells which we shall discuss towards the end of this section.

The parameter space metric discussed earlier also plays a role in reducing the computational cost, and in particular we used the metric for the space of *aligned-spin* waveforms [138]. The goal was to minimize the number of times that we needed to calculate the match. For a proposed parameter space point, we considered only those waveforms which have a match of better than 70% with the proposed waveform as computed by the aligned spin metric. The full match was computed only for the waveforms in the template bank which exceeded this threshold. The 70% threshold was found by trial and error and is low enough that we did not miss any templates close to the proposed waveform. Fig. 3.1 shows the convergence of the match for three particular cells in  $(\tau_0, \tau_3)$  space.

Before presenting the result of the above procedure and discussing some properties of the precessing face on template bank (FOB), we briefly describe an aligned-spin bank (ASB) which we used as a reference for comparison. Such a bank covered the same space of masses and

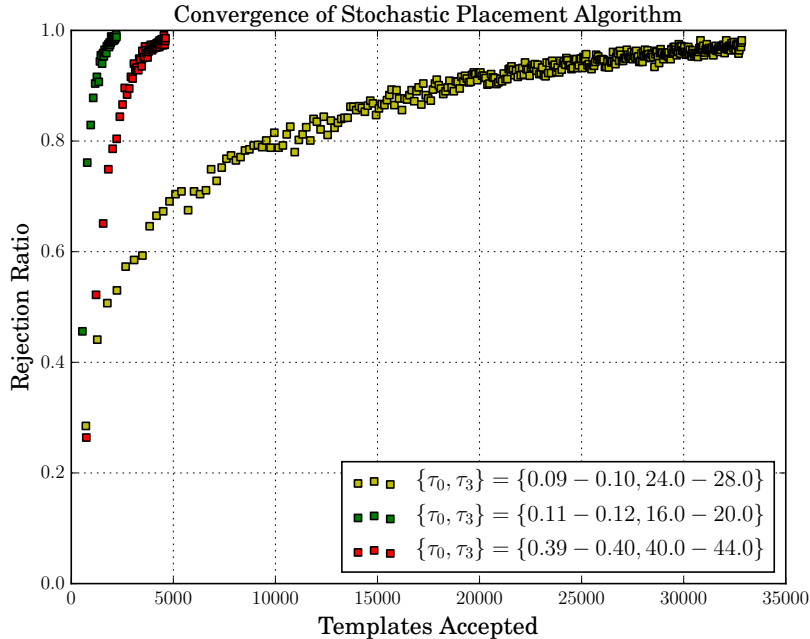


Figure 3.1: Convergence curves of three different cells used to construct the FOB. The figure and caption are copied from [146].

aligned spin components, but ignored precession. It was constructed via stochastic placement using non-precessing, inspiral-only post-Newtonian templates (namely the **TaylorF2** model in LALSimulation [168], see Section 1.1.4) and contains 130,646 templates. The template density is shown in Figure 3.2 in chirp time coordinates  $(\tau_0, \tau_3)$  and in such coordinates it is approximately constant. The ability of a similar bank at detecting aligned-spin and precessing NSBH systems has been characterized in previous studies [88, 90]. In contrast, the template bank for precessing face-on systems is shown in Figure 3.3. It contains 6,908,681 templates – a dramatic increase compared to the ASB. The densest parts are in the *high mass ratio, and highly anti-aligned spin* ( $\kappa < -0.5$ ) region of the bank. More than half of the total number of templates were placed in this region. Figure 3.4 shows the distribution of the mass ratio in the FOB and ASB, thereby demonstrating that the vast majority of points in the FOB consist of asymmetric systems (with mass-ratio  $q > 4$ ) in contrast to the ASB which is dominated by more symmetric systems.

Figures 3.5, 3.6, 3.7 and 3.8 display the precessing template bank in different slices of the parameter space. Figure 3.6 shows the template bank density in the  $(q, \chi^{\parallel})$  plane. Figure 3.7 shows the distribution of templates in the  $(\chi^{\perp}, \chi^{\parallel})$  plane. Finally Figure 3.8 gives the template bank distribution in the  $(q, \beta)$  plane. In Figure 3.7, we note that, higher template densities occur in the higher values of spin-orbit misalignment, which in-turn indicates higher precession.

As a result of breaking up the parameter space into independent cells, it was to be expected that the algorithm will place more templates than necessary at the borders between adjacent cells. This created so-called “gridlines” in the bank which are clearly visible in Figure 3.3. These were an artifact of splitting up the parameter space into independent regions. It resulted in having a larger number of templates than necessary. However, we saw that this is not a large effect for the chirp time cells that we have chosen (see Figures 3.9, 3.10).

The gridlines were most pronounced at the edges of the cells along the vertical direction, which implies that there is a degeneracy along the  $\tau_3$  direction. The gridlines along the  $\tau_0$  direction are much less pronounced. This was not surprising since  $\tau_0$  was determined entirely

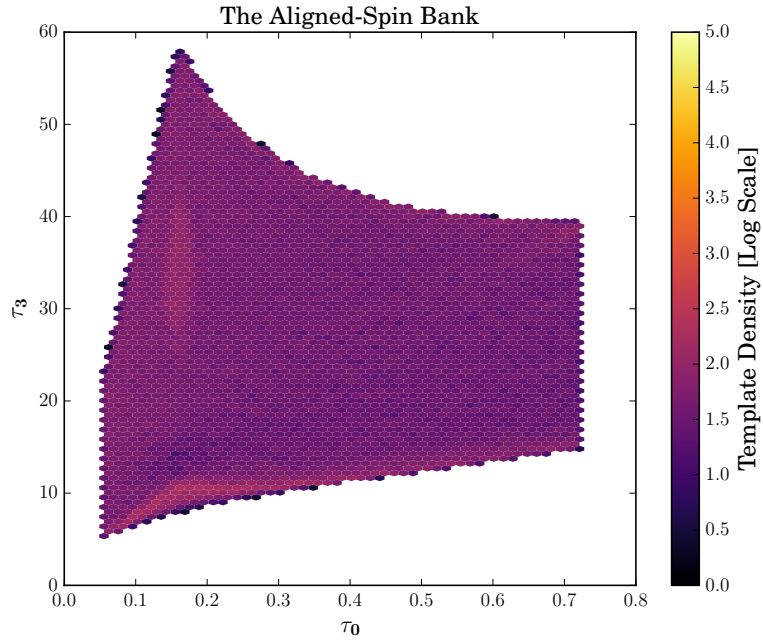


Figure 3.2: The aligned spin bank (ASB) in chirp time coordinates. The color bar density scale is the same as in Figure 3.3 for ease of comparison. Each hexbin has dimensions  $\{\Delta\tau_0 = 0.014, \Delta\tau_3 = 1.0\}$ . The image and caption are copied from [146].

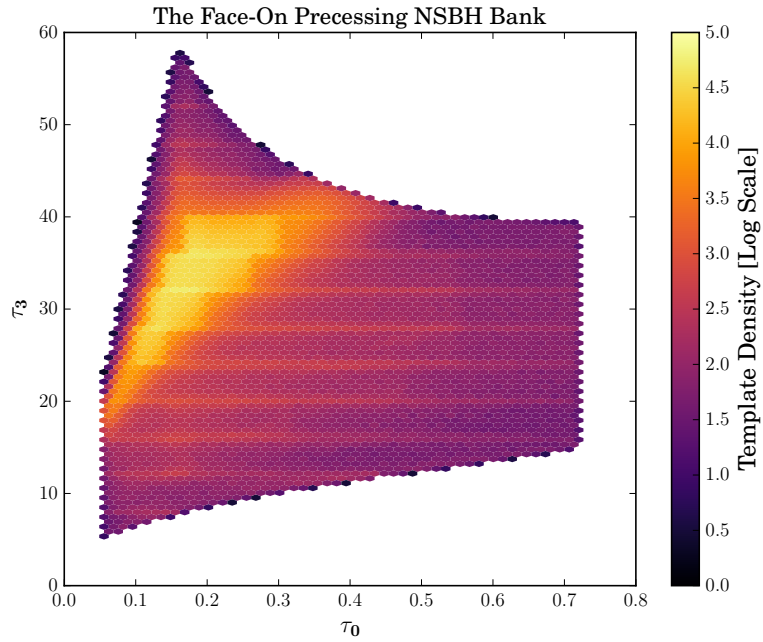


Figure 3.3: The FOB in chirp time coordinates. Each hexbin has dimensions  $\{\Delta\tau_0 = 0.014, \Delta\tau_3 = 1.0\}$ . The image and caption are copied from [146].



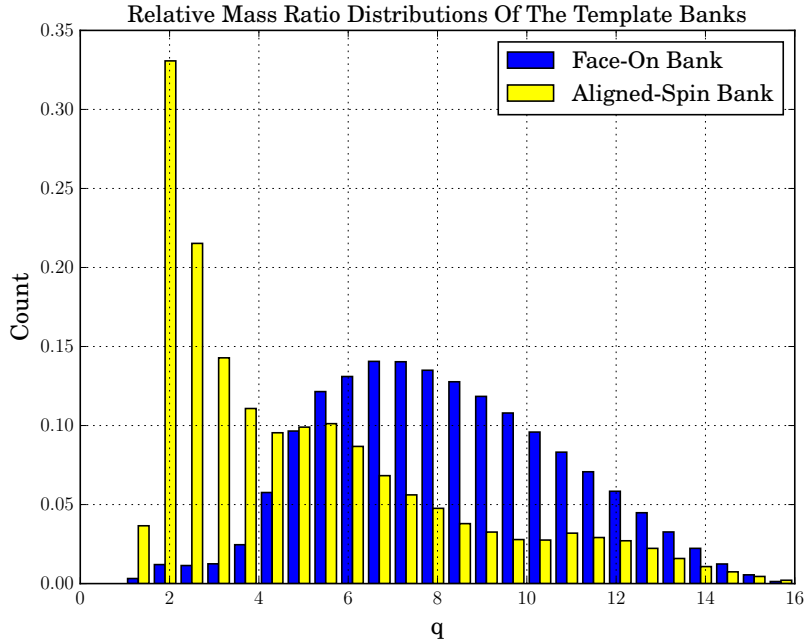


Figure 3.4: Normalized distribution of the mass-ratio  $q$  for the face-on precessing template and ASB. The image and caption are copied from [146].

by the chirp mass  $\mathcal{M}_C$ , and it is well known that  $\mathcal{M}_C$  is the parameter best determined from the inspiral phase [201].

This suggested that it should be possible to replace  $\tau_3$  by a better coordinate leading to fewer correlations. Regardless, we quantified the correlations between adjacent cells in the  $\tau_3$  and  $\tau_0$  directions respectively. Also, in order to optimize the size of the chirp time cells, it was crucial to estimate how far these gridlines overlapped into adjacent cells. To study this issue, we looked at two adjacent cells in  $\tau_3$  and  $\tau_0$ . By taking points in the one cell and calculating the overlap with every point in the adjacent cell, we determined the extent of the over-coverage in these two degrees of freedom. Figures 3.9 and 3.10 display the templates in adjacent cells which have an overlap greater than 95% with templates in the adjacent cell. The extent of these templates extends to about 25% of the cell in the  $\tau_3$  direction and 10% of the cell in the  $\tau_0$  direction. However, the number of such templates is only about 7% of the total number of templates in the upper cell and 1% of the lower cell for the horizontal gridline in Figure 3.9; 1% of the left cell and 1% of the right cell for the vertical gridline shown in Figure 3.10 .

To conclude this section, we validate the distributions obtained above by a numerical calculation of the Fisher matrix. If one were able to carry out a geometric template placement procedure, the density of templates would be proportional to the invariant volume element, i.e. to the square root of the determinant of  $g_{ij}$  (see Section 2.1). The same is generally true for probabilistic methods of template placement. We computed  $g_{ij}$  and its determinant directly by numerically computing the overlap between the derivatives of neighboring waveforms and compared this with the actual distribution of templates obtained in the template bank. Figure 3.11 shows the contour plot of  $\log \sqrt{|g|}$  for the  $\{15M_\odot, 1.4M_\odot\}$  case. Also shown are the points in the template bank whose masses are within 1% of these mass values demonstrating qualitative agreement between the two entirely different calculations. Similar results were obtained for other values of the masses and other slices of the parameter space. This agreement between the two independent calculations provided a sanity check and indicated that the great increase in the number of templates was a real feature of the space of precessing CBC waveforms. Using

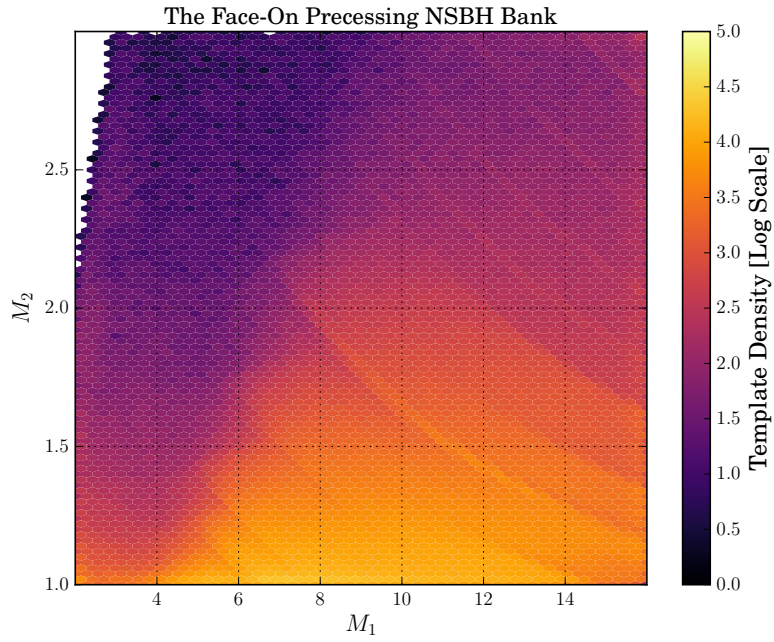


Figure 3.5: The FOB in solar mass ( $M_1, M_2$ ) coordinates. As before, the color bar is scaled with respect to the density of templates per bin  $\{\Delta M_1 = 0.28, \Delta M_2 = 0.02\}$ . The image and caption are copied from [146].

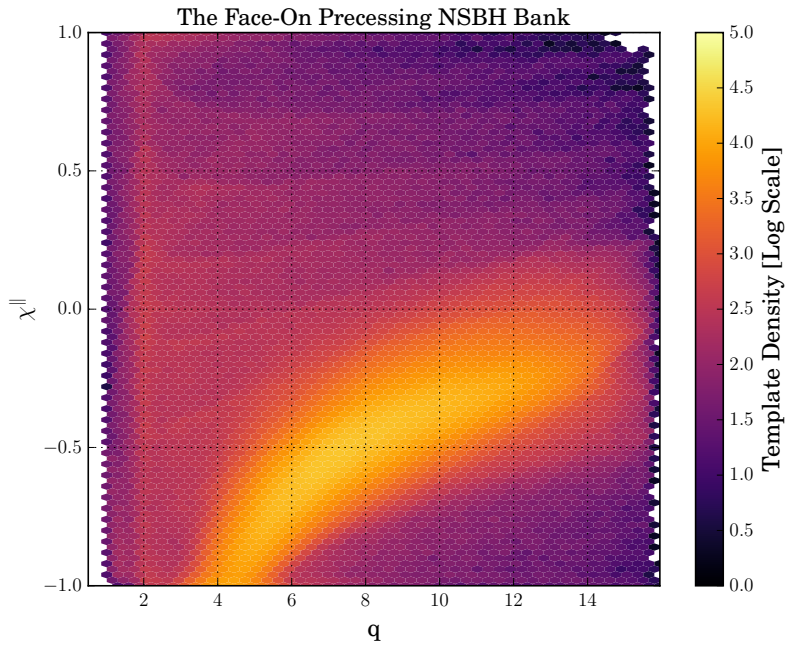


Figure 3.6: The FOB plotted in  $(q, \chi^{\parallel})$  coordinates. As before, the color bar is scaled with respect to the density of templates per hexbin  $\{\Delta q = 0.3, \Delta \chi^{\parallel} = 0.04\}$ . The image and caption are copied from [146].

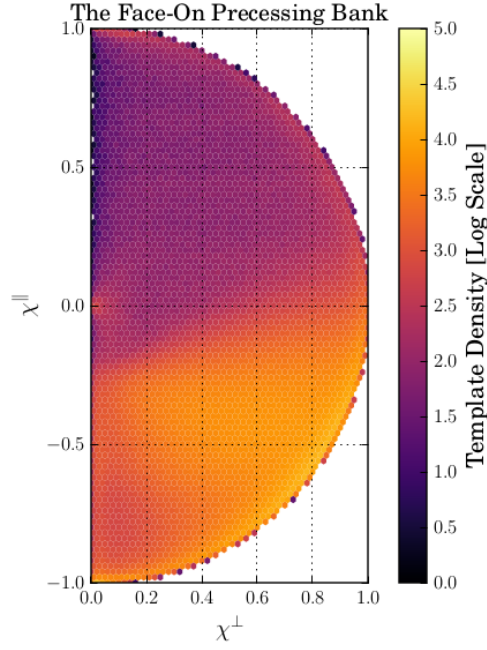


Figure 3.7: The spin distribution of the FOB. The y-axis is the component of spin parallel to the orbital angular momentum  $\mathbf{L}$  and the x-axis is the component of the spin perpendicular to  $\mathbf{L}$ . Each hexbin has dimensions  $\{\Delta\chi^\parallel = 0.04, \Delta\chi^\perp = 0.02\}$ . The image and caption are copied from [146].

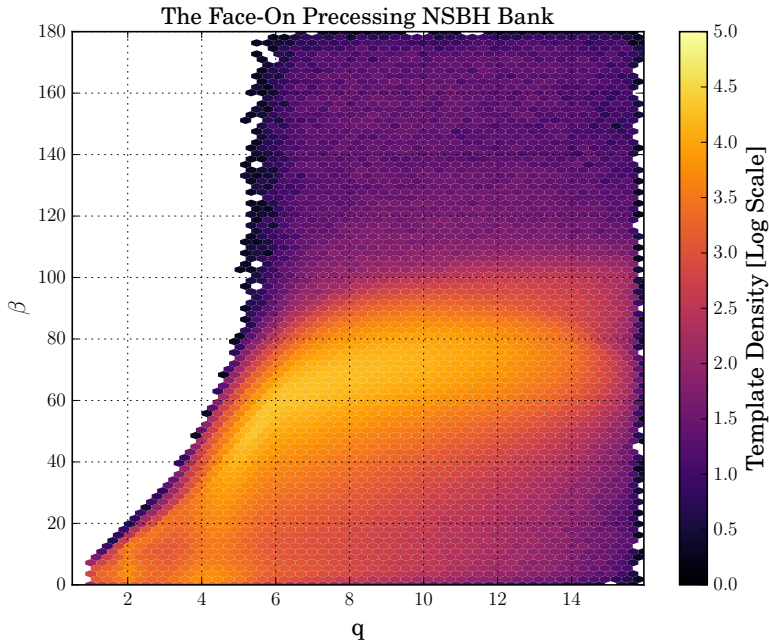


Figure 3.8: The precession cone,  $\beta$  and mass ratio,  $q$ , distribution of the FOB. Each hexbin has dimensions  $\{\Delta q = 0.3, \Delta\beta = 4^\circ\}$ . The image and caption are copied from [146].

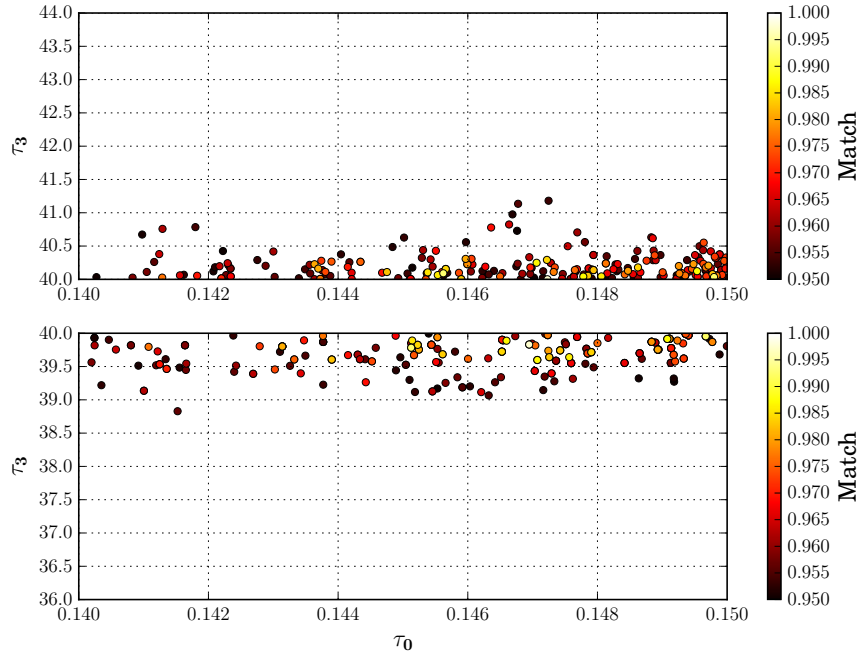


Figure 3.9: Plot of the templates in the cell  $(\tau_0, \tau_3) = (0.14 - 0.15, 40 - 44)$  that had an overlap greater than 95% with templates placed in the cell,  $(\tau_0, \tau_3) = (0.14 - 0.15, 36 - 40)$ . The dimensions of the two cells were chosen to span the entire cell, even though the edges were only affected by the gridlines. This caption is copied with minor paraphrasing from [146] and the image is reproduced using data from the same source with minor aesthetic alterations.

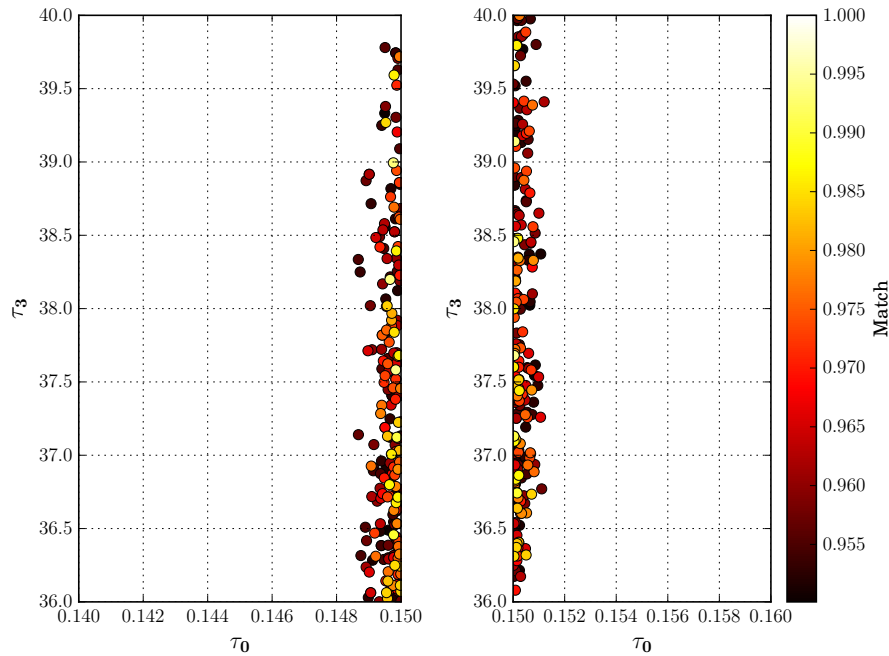


Figure 3.10: Plot of the templates in the cell  $(\tau_0, \tau_3) = (0.14 - 0.15, 36 - 40)$  that had an overlap greater than 95% with templates placed in the cell,  $(\tau_0, \tau_3) = (0.15 - 0.16, 36 - 40)$ . The dimensions of the two cells were chosen to span the entire cell, even though the edges were only affected by the gridlines.

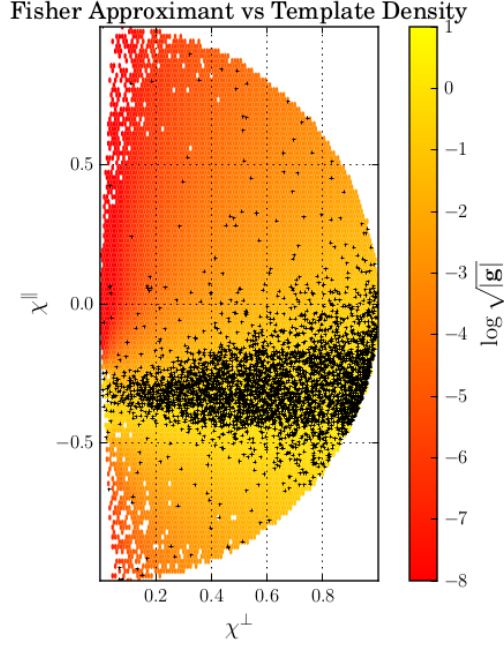


Figure 3.11: Comparison of the stochastic bank and the metric approximant  $\chi$  distributions for fixed masses  $\{15M_\odot, 1.4M_\odot\}$ . The color map represents  $\log \sqrt{|g|}$  and the scattered points denote the templates in the stochastic bank with masses within 1% of  $\{15M_\odot, 1.4M_\odot\}$ . Each hexbin has dimensions  $\{\Delta\chi^\parallel = 0.04, \Delta\chi^\perp = 0.02\}$ . The image and caption are copied from [146].

a different detection statistic as in [136] helps ameliorate the problem somewhat, but does not eliminate it.

### 3.3 Effectualness of the template bank

In this section we estimated the effectualness (see Section 1.2) of the FOB for different populations of NSBH systems and compared it with the ASB. When calculating matches, all simulations used a lower frequency cutoff of 30 Hz and an upper cut-off of  $4400/(M_1 + M_2)$  Hz, which is an approximant for the frequency corresponding to the innermost stable circular orbit of a Schwarzschild black-hole with mass equal to  $M_1 + M_2$ .

First, we wanted to consider the waveforms which were used to construct the FOB, namely the **SpinTaylorF2** waveforms and we wanted to compare the ASB with the FOB for precessing waveforms. In order for a bank to recover signals effectively, the bank must be able to recover NSBH systems over a range of mass and spin values and orientations of  $\hat{\mathbf{J}}$ . We considered two cases: i) by constraining the injections to be face-on NSBH systems, we looked at how well the FOB and ASB could recover **SpinTaylorF2** injections from the same proposal distribution used to construct the FOB, and ii) for arbitrary orientations of the total angular momentum (i.e.  $0^\circ < \theta_J < 180^\circ$ ). In both cases, we considered injections over the same  $\{M_1, M_2\}$  parameter space as before, i.e.  $2M_\odot < M_1 < 16M_\odot$  and  $1M_\odot < M_2 < 3M_\odot$ . The component masses of the injections were distributed uniformly within their respective ranges, the black-hole spins of the injections,  $\chi_{BH}$ , were distributed isotropically over the unit sphere. For the injection set “ii” we distributed the orientation of  $\hat{\mathbf{J}}$  isotropically over the unit sphere.

Figs. 3.12 and 3.13 show the recovered  $\hat{\mathbf{J}}$  fitting factors for the ASB and FOB banks for these two cases. Figure 3.12 shows the case when the injections are face-on. This is what the FOB

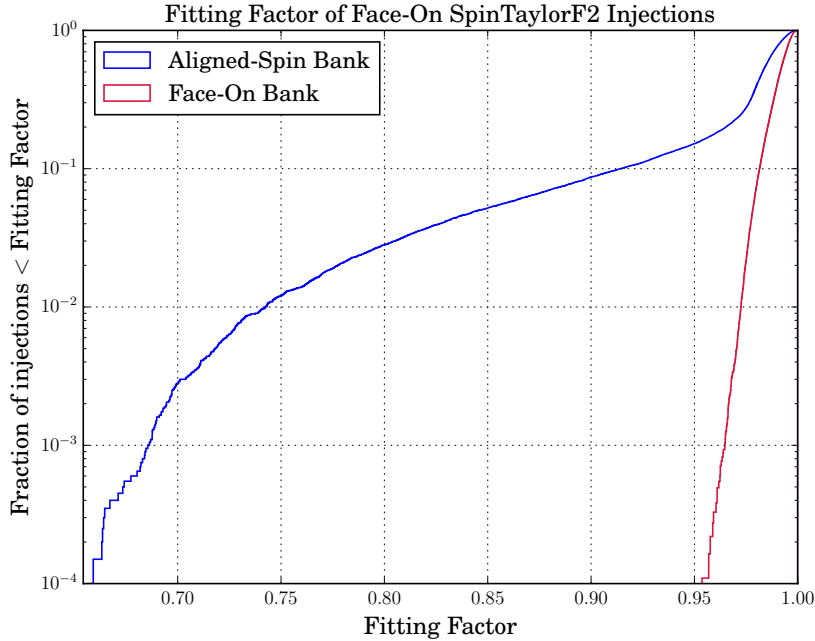


Figure 3.12: Cumulative histogram showing the recovered fitting factor of the face-on-precessing and aligned spin template banks for face-on **SpinTaylorF2** injections. The image and caption are copied from [146].

was built for and indeed, the plot shows that the FOB greatly outperforms the ASB. The fitting factors are worse than 97% for no more than 1% of the injections. Figure 3.13 shows the corresponding result when the injections are not constrained to be face-on. The recovered matches are reduced, but the FOB still outperforms the ASB over the full mass range.

To further investigate the differences between the FOB and ASB template banks, we now calculate the difference between the fitting factor obtained for the FOB and the ASB (we compute  $FF_{FOB} - FF_{ASB}$ ) and plot the result over different slices of the parameter space. These plots break up the relative performance of the two banks over different portions of the parameter space. Figs. 3.14 and 3.15 plot the difference in the fitting factors over  $(\tau_0, \tau_3)$  space. Figs. 3.16 and 3.17 show the difference in the fitting factor in  $q, \chi^{\parallel}$  coordinates for face-on and arbitrary injections respectively. Here, in Figure 3.16, as expected, we see that the FOB always performs better. Further, in the regions where the metric has highest density (see. Figure 3.6), the FOB shows the most improvement. Finally, Figure 3.18 shows the fitting factors for the FOB in the space of  $\theta_J$  and the precession cone opening angle  $\beta$ . We quote the value of  $\beta$  at a reference frequency of 100 Hz. While in principle  $\beta$  evolves in time and thus has a frequency dependence, it was shown in [63] that it is roughly constant over the inspiral regime for the frequency range of interest for ground based detectors. Figure 3.18 shows a clear correlation between the spin orientation and the opening angle. To a good approximation, the figure shows a circle in the  $\theta_J, \beta$  plane i.e. a cone around the  $\beta = 90^\circ$  direction. This relation was found analytically in [63].

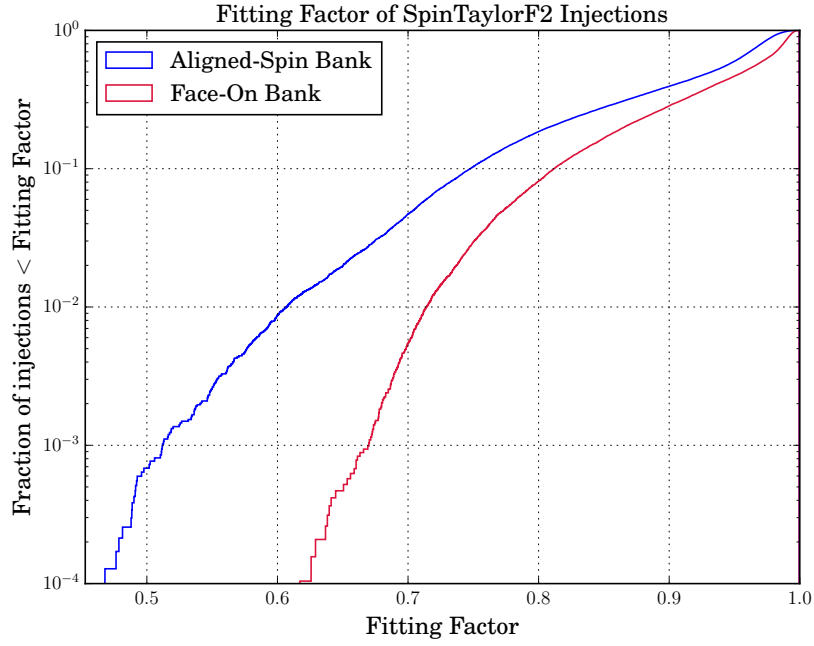


Figure 3.13: Cumulative histogram showing the recovered fitting factor of the face-on-precessing and aligned spin template banks for **SpinTaylorF2** injections with the component masses distributed uniformly within their respective ranges, spins distributed uniformly in  $\kappa$ , and  $\hat{\mathbf{J}}$  distributed uniformly over the sphere. Image and caption are copied from [146].

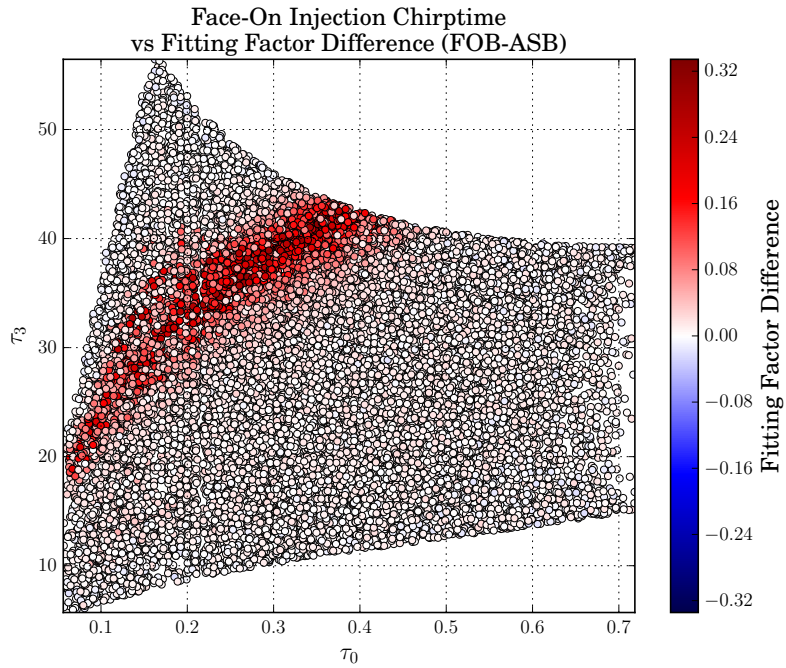


Figure 3.14: A plot of the difference in the recovered fitting factor between the precessing and aligned template banks over the  $\{\tau_0, \tau_3\}$  parameter space for face-on **SpinTaylorF2** injections. Image and caption are copied from [146].

Table 3.1: Table of the improvement in the relative detection volumes calculated from each injection set. The values in the third row represent injections with the component masses distributed uniformly within their respective ranges, black-hole spins were distributed isotropically over the unit sphere, and  $\hat{\mathbf{J}}$  distributed uniformly over the unit sphere. Results are grouped into three different regions  $\{All, HP, High\beta\}$ . *All* is the entire NSBH parameter space spanned by the injection set. *High* $\beta$  is defined as the region of parameter space that contains recovered injections with  $\beta \in \{60^\circ, 120^\circ\}$ . *HP* is the “High Precession” region of parameter space examined by [90] that contains recovered injections with  $\|\chi\| > 0.7$  and  $45^\circ < \theta_J < 135^\circ$ . Table and caption are copied from [146].

Injected Waveform	$\theta_J$	Mass Range $M_\odot$	$\frac{\mathcal{V}_{\text{FOB}}^{\text{All}}}{\mathcal{V}_{\text{ASB}}^{\text{All}}} - 1$	$\frac{\mathcal{V}_{\text{FOB}}^{\text{HP}}}{\mathcal{V}_{\text{ASB}}^{\text{HP}}} - 1$	$\frac{\mathcal{V}_{\text{FOB}}^{\text{High}\beta}}{\mathcal{V}_{\text{ASB}}^{\text{High}\beta}} - 1$
SpinTaylorF2	$0^\circ$	$\{2 - 16, 1 - 3\}$	3.26%	3.41%	14.2%
SpinTaylorF2	$0^\circ$	$\{15, 1.4\}$	6.42%	4.66%	23.9%
SpinTaylorF2	$0 - 180^\circ$	$\{2 - 16, 1 - 3\}$	23.7%	9.88%	134%
SpinTaylorF2	$0 - 180^\circ$	$\{15, 1.4\}$	11.3%	3.22%	14.4%

To quantify the improvement that a precessing face-on bank would bring to a Compact Binary Coalescence (CBC) search, we calculated the relative improvement in detection volume [88] of the FOB and ASB banks (see Section 1.2 Eq. 1.67). In the absence of any prior astrophysical likelihood distribution of NSBH systems, the detector volume,  $\mathcal{V}$ , is proportional to the sum of the cube of the product of the optimal SNR of the injections,  $\rho_i$ , with the fitting factor,  $m_i$ , obtained from attempting to recover a set of injected NSBH signals into the bank,

$$\mathcal{V} \propto \sum_i (m_i \rho_i)^3. \quad (3.4)$$

By taking the ratio of the detection volumes of the FOB and ASB,  $\mathcal{V}_{\text{FOB}}$  vs  $\mathcal{V}_{\text{ASB}}$ , we get a measure of the relative improvement the FOB could bring to the search. Results are shown in Table 3.1.



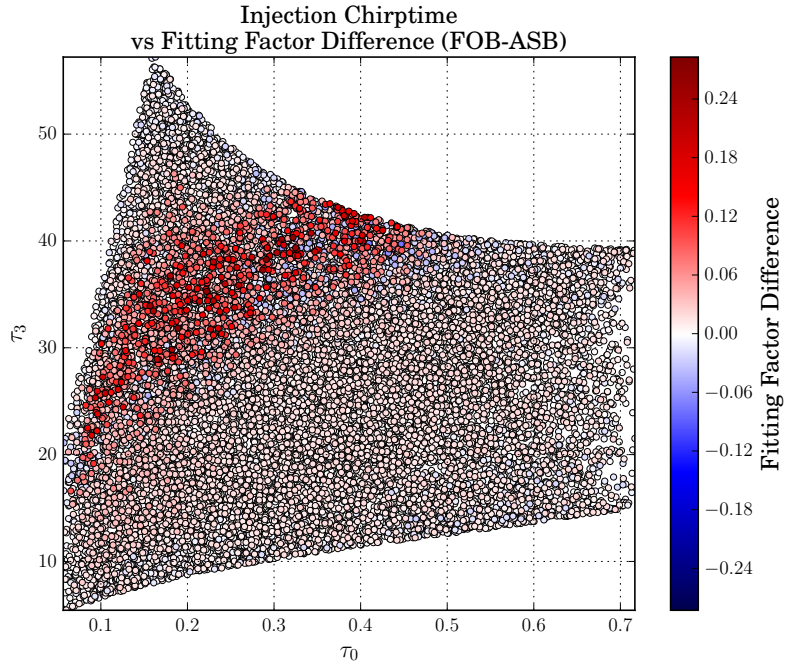


Figure 3.15: A plot of the difference in the recovered fitting factor between the precessing and aligned template banks over the  $\{\tau_0, \tau_3\}$  parameter space for **SpinTaylorF2** injections that are distributed uniformly in chirp time,  $\{\tau_0, \tau_3\}$ , with  $\hat{\mathbf{J}}$  distributed uniformly over the sphere. Image and caption are copied from [146].

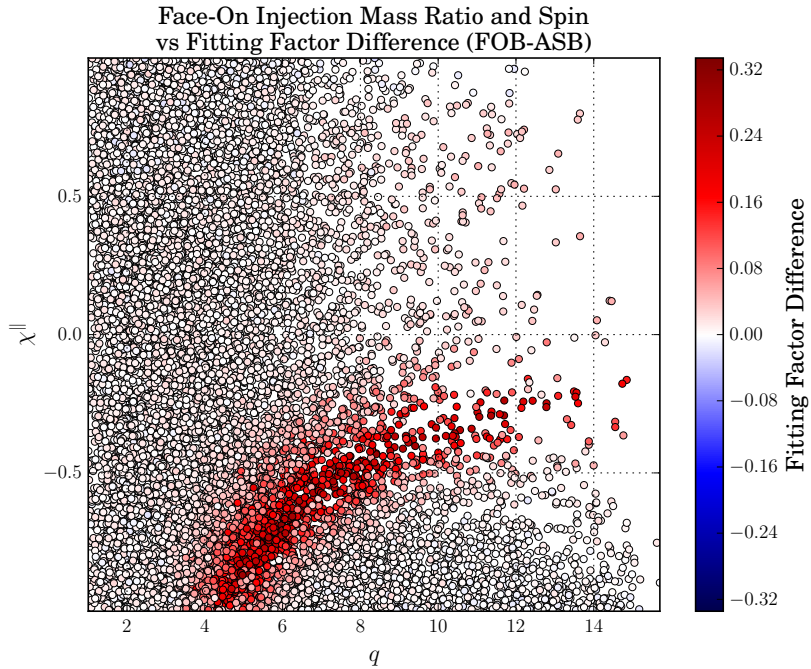


Figure 3.16: A plot of the difference in the recovered fitting factor between the precessing and aligned template banks over the  $\{q, \chi_{\parallel}\}$  parameter space for face-on **SpinTaylorF2** injections. Image and caption are copied from [146].

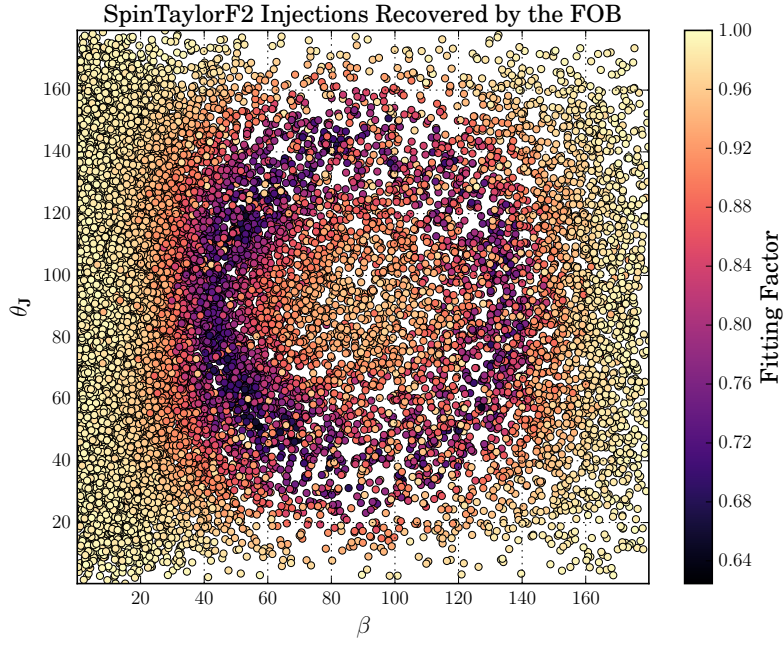


Figure 3.18: Recovered fitting factor of the precessing template bank over the  $\{\theta_J, \beta\}$  parameter space with **SpinTaylorF2** injections that are distributed uniformly in chirp time,  $\{\tau_0, \tau_3\}$ , with  $\hat{\mathbf{J}}$  distributed uniformly over the sphere.

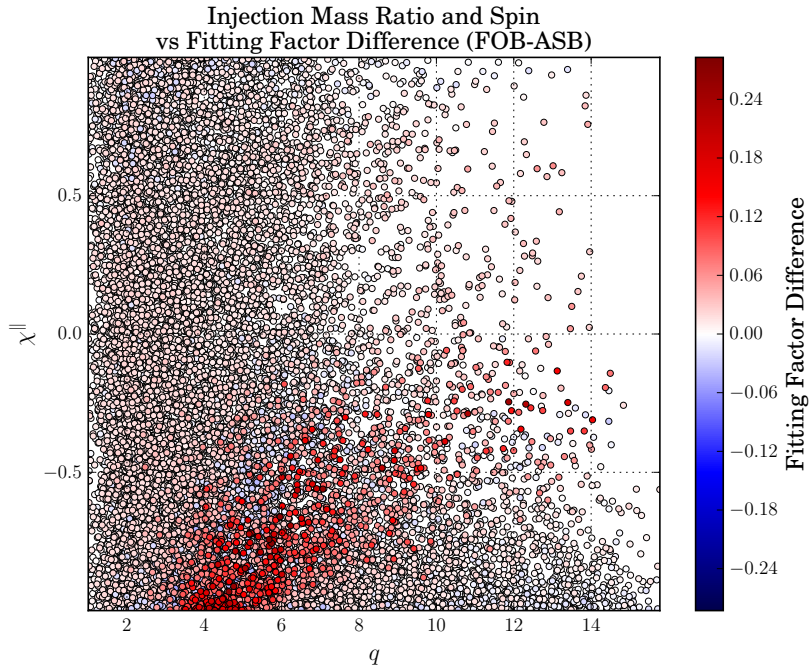


Figure 3.17: A plot of the difference in the recovered fitting factor between the precessing and aligned template banks over the  $\{q, \chi_{\parallel}\}$  parameter space for **SpinTaylorF2** injections that are distributed uniformly in chirp time,  $\{\tau_0, \tau_3\}$ , with  $\hat{\mathbf{J}}$  distributed uniformly over the sphere. The image and caption are copied from [146].

## 3.4 Conclusions

In this section we have presented a template bank for gravitational wave searches for precessing NSBH systems. The template bank assumed that the total angular momentum vector is pointing directly towards or away from the detectors. It covered the mass ranges  $2M_{\odot} < M_1 < 16M_{\odot}$ ,  $1M_{\odot} < M_2 < 3M_{\odot}$  and the black-hole spin vector was allowed to have an arbitrary orientation. The template bank ends up having 6,908,681 templates assuming the early Advanced LIGO noise curve. We demonstrated that the sensitive volume for systems with large spin misalignments (i.e. large precession cone angles) for this template bank was roughly twice as large as for the aligned spin bank (see third row of Table 3.1).

We used the frequency domain, inspiral-only, **SpinTaylorF2** waveform for our study. The aligned spin template bank over the same mass range has only 130,646 templates and this great increase in the number of templates is validated by an independent numerical evaluation of the determinant of the parameter space metric. Despite this large increase in the number of templates, we show that stochastic methods can still be implemented. It required us to break up the parameter space into smaller, approximately independent regions and we found that the chirp times provide a suitable coordinate choice with which to do this. The template bank could be pruned by removing templates near the boundaries of the chirp time cells but this would only reduce the number of templates by about 5-10%. Using a different detection statistic as in [136] should further help in decreasing the number of templates somewhat, but it is still an open issue whether the 97% minimal match condition should be kept as gravitational wave detectors improve their low frequency sensitivity. In either case, working in chirp time coordinates should allow us to deal with the computational problem.

A large fraction of the templates of our bank were in the anti-aligned part of parameter space (with  $\kappa < -0.5$ ). If one believes that such systems are disfavored astrophysically, it is straightforward to construct a precessing template bank for restricted values of  $\kappa$ . Depending on how restricted we would like the black-hole spin orientation to be, this might provide a useful compromise between computational cost and astrophysical priors. It would also be desirable to be able to apply traditional geometric methods and to place a lattice of templates, but this requires us to find suitable coordinates for the space of precessing signals.

## 3.5 Acknowledgments

The text presented in this chapter was originally written collaboratively by K Haris, Badri Krishnan, Archana Pai, Alex B. Nielsen, Tito Dal Canton, Andrew Lundgren, and myself. The Face-On Bank was constructed by Tito Dal Canton, Henning Fehrmann, Andrew Lundgren and myself. The Fisher matrix approximant was developed by K Haris and Archana Pai. The GPU implementation of **SpinTaylorF2** was developed by Haris K. For part of the project, T. D. C. was supported by an appointment to the NASA Postdoctoral Program at the Goddard Space Flight Center, administered by Universities Space Research Association under contract with NASA. K.H. acknowledges DST-MPG Max Planck Partner Group at IISER TVM for the travel support for the visit to the Albert Einstein Institute during which part of the work was carried out. The original paper has LIGO document number LIGO-P1600330.



Efficient multi-dimensional template placement is crucial in computationally intensive matched-filtering searches for gravitational waves<sup>1</sup>. In chapter 3, we implemented a parallelized stochastic placement routine in a template bank in a high dimensional parameter space and found that the final template bank had artificially dense gridlines (see Figures 3.3, 3.10 and 3.9). In Section 2.2, I mentioned that the presence of gridlines in the Sbank algorithm could be mitigated by implementing an initial coarse stochastic placement or seeding the template bank with a geometric lattice as is done in hybrid bank construction algorithms. However, this does not remove gridlines from the bank entirely. As evident in Figures 2.8 and 2.6, these artificially dense regions are prevalent in the hybrid construction methods used to build CBC template banks for use in LIGO-Virgo searches. These features arise because the stochastic and hybrid methods for template placement do not explicitly place templates according to the regions covered by individual templates, the so called template isosurfaces. Even geometric lattices can produce artificially dense or under-dense regions as illustrated in Figure 2.9. In this chapter I introduce a new algorithm for CBC template placement, *template nudging algorithm*, that repositions templates according to their isosurfaces [145].

The template nudging algorithm is a metric-agnostic implementation of the *Neighboring Cell Algorithm* (NCA), which was first successfully applied for a binary millisecond pulsar search in data from the Fermi satellite, to the CBC parameter space [216]. It repositions templates from over-dense regions to under-dense regions and reduces the number of templates that would have been required by a stochastic method to achieve the same detection volume (see Section 1.2).

It was shown in [120] that for the Fermi  $\gamma$ -ray binary pulsar search, using these methods leads to a reduction in the number of distance computations in three dimensions by about five orders of magnitude compared to other standard stochastic template bank algorithms. In this chapter we applied this method to the aligned-single-spin neutron-star-black-hole binary coalescence inspiral-merger-ringdown gravitational wave parameter space (see Section 1.1.4). Specifically, we focused on neutron-star-black-hole (NSBH) systems since they make up 60% of the templates placed in the last LIGO-Virgo observation period [15, 89] (see Section 2.3). The component masses for this range are black-hole of masses  $M_{BH}$  such that  $2M_{\odot} < M_{BH} < 16M_{\odot}$ , and neutron-star masses  $M_{NS}$  such that  $1M_{\odot} < M_{NS} < 3M_{\odot}$ . As a proof of concept for applying this new template construction method to CBC searches, we used the inspiral-merger-ringdown-phenomenological waveform model (**IMRPhenomD**) [232, 135, 155] to approximate

---

<sup>1</sup>Legal disclaimer: “The content and text presented in this chapter is copied with minor alterations from a publication I wrote with co-authors Henning Fehrmann, Alex B. Nielsen, Badri Krishnan, and Franz Harke [145]. The use of these materials is protected under ‘Fair Use’ (UrhG §24,70,63) and consistent with the requirements of § 6 Abs. 1 PromO.”

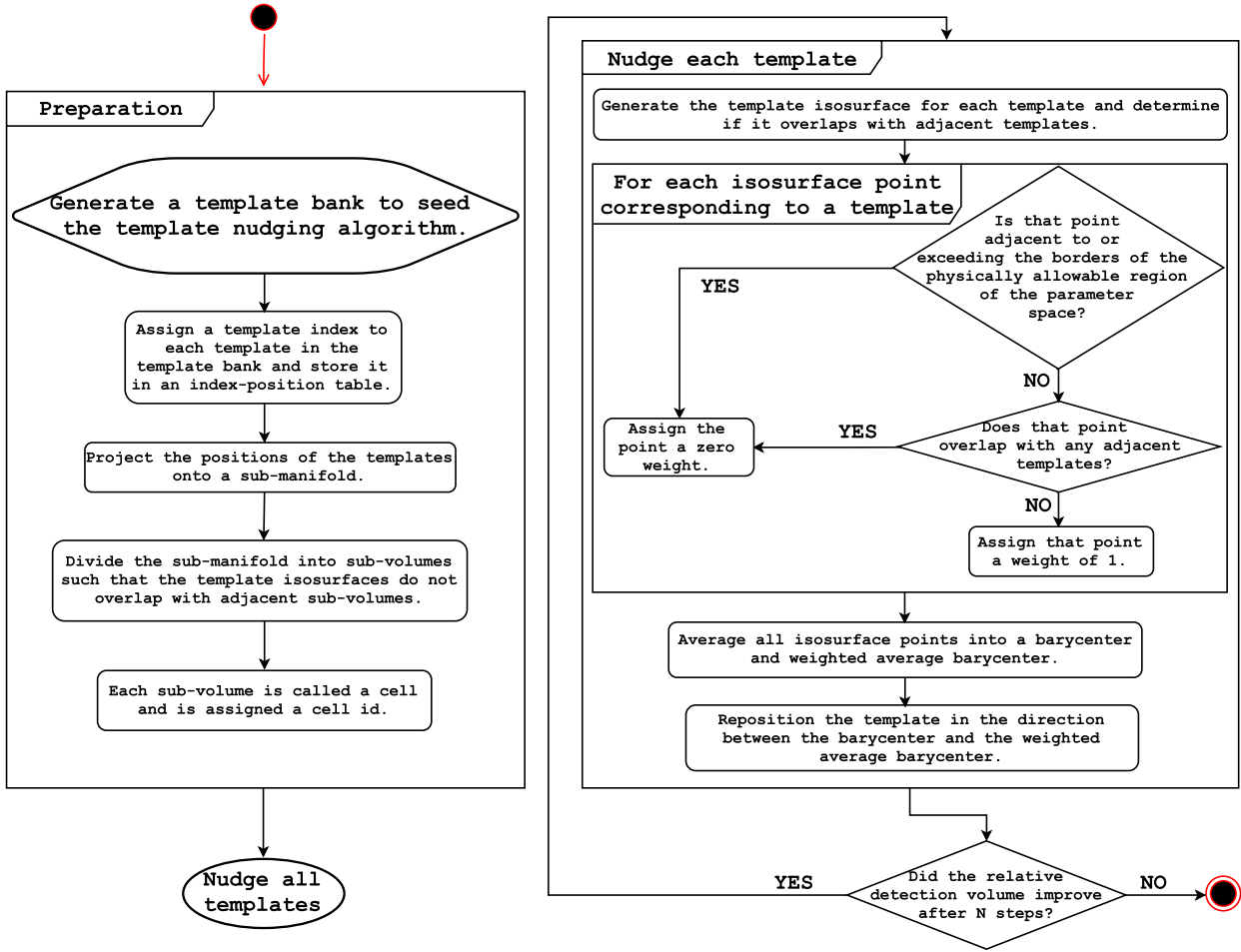


Figure 4.1: Flowchart of the template nudging algorithm procedure. Preparation steps are listed in the frame on the left and the template nudging procedure is listed in the frame on the right. In Section 4.3 we set “N” = 100 for the termination condition shown in the diamond on the lower right. Image and caption are copied from [145].

the underlying coalescence NSBH gravitational wave signal.

Contrasting with the binary pulsar search parameter space, at the time there was no known analytic expression for this CBC waveform mismatch metric. Therefore, our implementation of the NCA method required additional steps to construct the template isosurfaces agnostic to the underlying metric. This flexibility makes our method readily generalizable to other CBC parameter spaces as well as other template bank construction problems outside of gravitational wave detection.

## 4.1 Template nudging algorithm

A stochastic placement algorithm is unlikely to place templates optimally and will place more templates than are necessary to achieve the same effectualness [137] (see Section 2.2). We therefore employed an algorithm (see Figure 4.1) to move templates slightly, *template nudging* (see Figure 4.2), facilitating the re-arrangement of templates in a template bank into a configuration that improves the template bank’s effectualness and detection volume without the addition of more templates.

In Section 4.2 we applied the template nudging algorithm to the CBC parameter space by adapting a version of the *Neighboring Cell Algorithm* (NCA) method [120] that does not

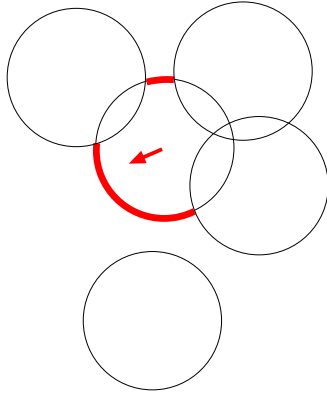


Figure 4.2: Diagram of a simplified example displaying how template are repositioned in the NCA/template nudging algorithm. The template isosurfaces are indicated by the red and black circles. The black regions of the circle in the center of the diagram indicate the regions of that template isosurface that overlap with the adjacent templates. The red regions of that central template in that same circle indicate the portions of that isosurface that do not overlap with adjacent template isosurfaces. The nudging mechanism repositions templates in the direction where the template isosurfaces do not overlap. This image is copied from [120], the caption is paraphrased from the same source.

require an analytic expression of the metric and will work in parameter spaces where numeric approximations of the generalized metric are ill-conditioned. In our application of the method, the surfaces of the three dimensional regions covered by individual templates, template *isosurfaces*, within a pre-specified maximal mismatch (i.e. 3%) must be determined numerically. The following list outlines the procedure for nudging a template bank in the absence of a metric.

1. Select a template  $T$ .
2. Find a set of points that are uniformly distributed distributed on the boundary of  $T$ 's isosurface.
3. Check whether each of these points is inside a neighboring template's isosurface. If there is overlap, the considered boundary point gets zero *weight*. If not, it gets unit weight (i.e. the template will not be nudged toward the adjacent overlapping template isosurface).
4. If a boundary point is outside of the considered parameter space this point also gets zero weight.
5. The boundary points are averaged together using these *weights* into a *barycenter*.
6. The template is nudged (i.e. coordinates are perturbed) in a direction determined by the barycenter offset relative to the unweighted barycenter of the boundary points and a maximum relative amount,  $\epsilon$  (the pre-specified *template nudge factor*, the fractional distance between the original template center and the closest isosurface point beyond which templates cannot be repositioned).

This algorithm could be applied to any under-covered bank regardless of the method used to create that template bank (e.g. geometric, stochastic, or hybrid template bank placement methods which place templates with geometric and stochastic methods) and will improve the effectualness and detection volume. This provides a convenient way of enhancing any existing template bank construction method.

### 4.1.1 Neighboring cell algorithm

In order to efficiently cover the parameter space with non-overlapping cells, the cells should be approximately the same size as the area of the chirp time volume covered by an individual template, as determined by the desired maximal mismatch between neighboring templates (3%)<sup>2</sup>. In the simplest example these could be hyper spheres with a regular stacking in any choice of coordinates. To produce a list of the nearest neighboring templates we implemented the following procedure.

1. Each cell is uniquely indexed.
2. Given a cell index, the indices of neighboring cells can be computed easily or can be stored in a table. Two cells are neighboring if they share at least one common boundary point.
3. Given a position of a template, the index of a cell can easily be computed by any kind of hash algorithm or a binary search. In Euclidean space and with a hyper-cubic cell lattice this can be achieved by using rounding or truncating operations on the position values of the templates.
4. A second table stores template indices and template parameters in memory.
5. Given a template, one finds all templates in the vicinity by collecting the templates in the corresponding cell and all neighboring cells. Therefore relatively few mismatches have to be computed when placing a template as opposed to other stochastic placement algorithms.

## 4.2 Application to the CBC aligned-spin NSBH template bank

### 4.2.1 Isosurface geometry in chirp time coordinates

Template placement efficiency is largely dependent on the geometry of the regions covered by individual templates, (i.e. the template *isosurfaces*). Using the physical parameters of the aligned-spin NSBH parameter space (see Section 1.1.6)  $\{M_{BH}, M_{NS}, \chi_{BH}\}$ , these template isosurfaces are non-uniform (their geometries vary across the parameter space). An ideal coordinate system for template placement would yield isosurfaces that are uniformly spherical at any point in the proposal distribution. Isosurfaces that have curved or sharp edges are computationally challenging to model, and as was discussed in Section 2.1, they tend to create *holes* (insufficiently populated regions in the template bank).

Since we were unable *a priori* to determine an ideal coordinate system for the placement of NSBH **IMRPhenomD** templates (see Section 1.1.4), we choose three chirp time coordinates  $\{\tau_0, \tau_2, \tau_3\}$  [233, 237] (see Section 1.1.5) that have been demonstrated to flatten out the **TaylorF2** template bank [88, 62]. These chirp times (see Eqs. 1.31, reproduced below) are defined with the following conventions where  $f_0$  denotes a reference frequency, here chosen as 30Hz:

$$\tau_0 = \frac{5}{256} \frac{(\pi f_0)^{-\frac{8}{3}} (M_{BH} + M_{NS})^{\frac{1}{3}}}{M_{BH} M_{NS}} \quad (4.1)$$

---

<sup>2</sup>The efficiency of the template nudging algorithm improves the smaller these cells are. However, it is important that these cells are not too small. Subsequent fitting factor calculations (see Section 1.2) will be inaccurate if the cell dimensions are specified such that template isosurfaces extend beyond nearest-neighboring cells.



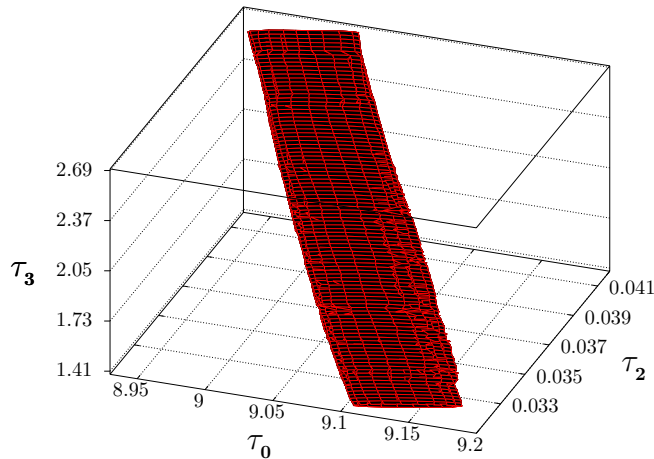


Figure 4.3: Template isosurface corresponding to  $\{M_{BH} = 10M_{\odot}, M_{NS} = 1.4M_{\odot}, \chi_{BH} = 0.5\}$  plotted in chirp time coordinates  $\{\tau_0, \tau_2, \tau_3\}$ . The isosurface gets truncated as it hits the border of the physically allowable region of the parameter space. Image and caption are copied from [145].

$$\tau_2 = \frac{5}{256} \frac{M_{BH} + M_{NS}}{M_{BH}M_{NS}} (\pi f_0)^{-\frac{8}{3}} \times \left[ \frac{743}{336} + \frac{11}{4} \frac{M_{BH}M_{NS}}{(M_{BH} + M_{NS})^2} \right] \quad (4.2)$$

$$\tau_3 = \frac{(\pi f_0)^{-\frac{5}{3}}}{128} (M_{BH} + M_{NS})^{\frac{32}{15}} (M_{BH}M_{NS})^{-\frac{7}{5}} \times \left[ 16\pi - \frac{\chi_{BH}}{6} \left( \frac{19M_{BH}M_{NS}}{(M_{BH} + M_{NS})^2} + \frac{113M_{BH}}{M_{BH} + M_{NS}} + 94 \right) \right] \quad (4.3)$$

## 4.2.2 Template isosurfaces

In these three chirp time coordinates,  $\{\tau_0, \tau_2, \tau_3\}$ , the regions of the parameter space covered by individual templates are non-ellipsoidal, concave, thin and therefore difficult to model analytically (see Figure 4.3 and 4.4).

However, we observed that the **IMRPhenomD** waveform is least sensitive to perturbations in the  $\tau_2$  degree of freedom. We found that individual cross-sections of these isosurfaces in the remaining two degrees of freedom could be modeled by two dimensional ellipsoids. We compensated for the lack of a three dimensional isosurface metric by modeling the three dimensional isosurface at a select number of cross-sections where the two dimensional projection of the isosurface is easier to model.

A further computational challenge is determining the scope of individual ellipsoid isosurface cross-section in the fewest computations possible. These ellipsoids are often very stretched out in these coordinates, therefore we implemented the following method to select points.

The three dimensional mismatch isosurface can be obtained by computing the mismatch isosurface of individual cross-sections by keeping  $\tau_2$  constant for each cross-section. The isosurface is hence a ring on the two dimensional sub-manifold parametrized by  $\tau_0$  and  $\tau_3$ . In the first step we find the point on this plane which has the smallest mismatch with our considered template by applying a simplex amoeba gradient-free-downhill method [191]. The routine starts

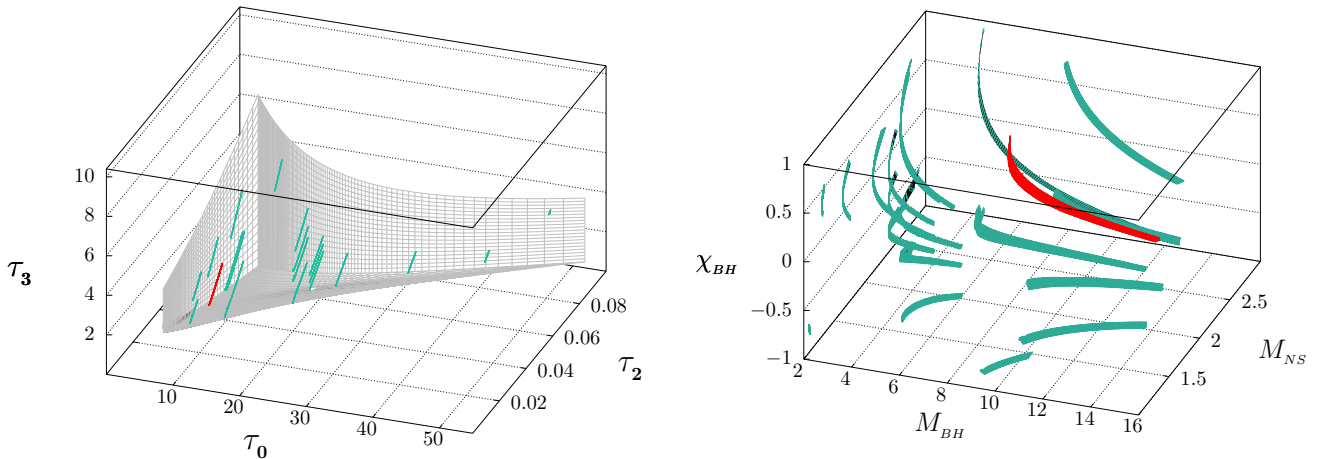


Figure 4.4: Examples of template isosurfaces (dark green) within the borders of the physical allowable regions of the CBC single-spin NSBH parameter space. The top panel is plotted in chirp time coordinates  $\{\tau_0, \tau_2, \tau_3\}$  (the gray mesh) and the bottom panel in physical coordinates  $\{M_{BH}, M_{NS}, \chi_{BH}\}$ . The template isosurface corresponding to  $\{M_{BH} = 10M_\odot, M_{NS} = 1.4M_\odot, \chi_{BH} = 0.5\}$  plotted in Figure 4.3 is highlighted in red. Images and caption are copied from [145].

by finding a point on the sub-manifold which is in the allowed parameter space. The downhill method starts from there. Since the template volume ranges in the  $\tau_2$  direction from one end to the other we always find a set of points on our considered  $\tau_2$  plane which have mismatches with our template smaller than the allowed critical mismatch of 3%. These points are enveloped by the template isosurface and are described by:

$$P \equiv \{\vec{p}_i | mm(\vec{p}_i, \vec{t}) \leq 3\%\}, \quad (4.4)$$

where  $\vec{t}$  is the vector of the template in the parameter space. Usually we found 12 to 25 points by using the simplex amoeba gradient-free-downhill method. We used these “inside” points to obtain a local approximation of the metric on this surface describing the distance between the point of the maximal mismatch to the points found by the simplex method. The description by a metric is not quite correct since the mismatch of the minimal point is much smaller than 3% but not zero. If this mismatch becomes significantly larger, then one might think about adding a constant to Eq. 4.5. However, for deriving the isosurfaces the following method worked sufficiently well. We expanded the metric starting with quadratic terms:

$$\tilde{m} = \sum_{p=2}^{\infty} \sum_{i_1 \geq i_2 \geq \dots \geq i_p}^D \gamma_p(i_1, i_2, \dots, i_p) \prod_{l=1}^p d_l, \quad (4.5)$$

$D$  is the dimension of our manifold, in our case  $D = 2$  and  $d_l$  are the components of the distance vectors. In the following we restricted ourselves to the second order expansion. For each point in the set,  $P$  has a real mismatch  $m_k$  and the mismatch is approximated by the metric  $\tilde{m}_k$ . We choose the metric components  $\gamma_2(i, j)$  such that the quantity  $\chi^2 = \sum_k (m_k - \tilde{m}_k)^2$  was minimized.

The component  $d_k^i$  is the  $i$ th component of the  $k$ th distance vector towards our minimal point  $p_0$  on the plane. We minimize the  $\chi^2$  with respect to the metric components:

$$\frac{\partial \chi^2}{\partial \gamma_2(o, p)} = \sum_k [m_k - \quad (4.6)$$

$$\sum_{i_1 \geq i_2}^D \gamma_2(i_1, i_2) d_{i_1}^k d_{i_2}^k ] d_o^k d_p^k \quad (4.7)$$

$$= 0. \quad (4.8)$$

This set of equations can be described by

$$\Rightarrow \sum_k \underbrace{\begin{pmatrix} \mathcal{D}_0^k \mathcal{D}_0^k & \mathcal{D}_0^k \mathcal{D}_1^k & \mathcal{D}_0^k \mathcal{D}_2^k \\ \mathcal{D}_1^k \mathcal{D}_0^k & \mathcal{D}_1^k \mathcal{D}_1^k & \mathcal{D}_1^k \mathcal{D}_2^k \\ \mathcal{D}_2^k \mathcal{D}_0^k & \mathcal{D}_2^k \mathcal{D}_1^k & \mathcal{D}_2^k \mathcal{D}_2^k \end{pmatrix}}_{=\mathcal{D}} \begin{pmatrix} \gamma_2(1, 1) \\ \gamma_2(2, 1) \\ \gamma_2(2, 2) \end{pmatrix} \quad (4.9)$$

$$= \sum_k m_k \begin{pmatrix} \mathcal{D}_0^k \\ \mathcal{D}_1^k \\ \mathcal{D}_2^k \end{pmatrix}, \quad (4.10)$$

where  $\mathcal{D}_i^k = (d_1^k)^{2-i} (d_2^k)^i$ . We inverted  $\mathcal{D}$  and obtained the second order expansion values for the metric  $\gamma_2(i, j)$ . This procedure can be expanded to arbitrarily high orders of the metric expansion. We approximated the metric in a quadratic form:

$$g = \begin{pmatrix} \gamma_2(1, 1) & \frac{1}{2}\gamma_2(2, 1) \\ \frac{1}{2}\gamma_2(2, 1) & \gamma_2(2, 2) \end{pmatrix}. \quad (4.11)$$

We computed eigenvalues  $v_i$  and eigenvectors  $\vec{e}_i$  of this metric and computed a set of  $N$  points approximately in the vicinity of the isosurface.  $I = \vec{p}_i$  with  $\vec{p}_i = \sin(2\pi i/N)\vec{e}_1\sqrt{0.03/v_1} + \cos(2\pi i/N)\vec{e}_2\sqrt{0.03/v_2}$ . These points were not equidistant but sufficiently well distributed for our purposes.

We shifted the points in the radial direction with respect to the center point such that the points have a mismatch of exactly 3% using the Newton-Raphson method.

We computed the barycenter of our shifted set of points and repeated the metric approximation method and the shifting to get an even better set of points.

The scheme was applied for all distinct  $\tau_2$  planes.

### 4.2.3 Cell Structure

In order to apply the NCA method, we provided an appropriate cell structure with the following properties:

- the cells were sufficiently small
- templates within a cell can reached the neighboring cells, but not next-nearest neighboring cells
- a cell index could be easily and quickly computed knowing the template parameter space points.

Since each template spanned the entire parameter space in the  $\tau_2$  direction, splitting the parameter space in this direction was not possible. On the other hand, the templates had a very small size in the  $\tau_0$  direction so we could safely split the parameter space in this direction. We divided the parameter space in the  $\tau_0$  direction into 300 slices. We mapped the  $\tau_0$  coordinates into a unit length parameter space  $x = (\tau_0 - 4)/50$ . The templates were curved in the  $\tau_3$  direction, thus further splitting was not directly feasible. To get the templates in a compact form we applied an *ad hoc* transformation  $y = ((\tau_3/\tau_2 - 20 + 2.5/\tau_2)\tau_0 - 480)/2500$ . The new

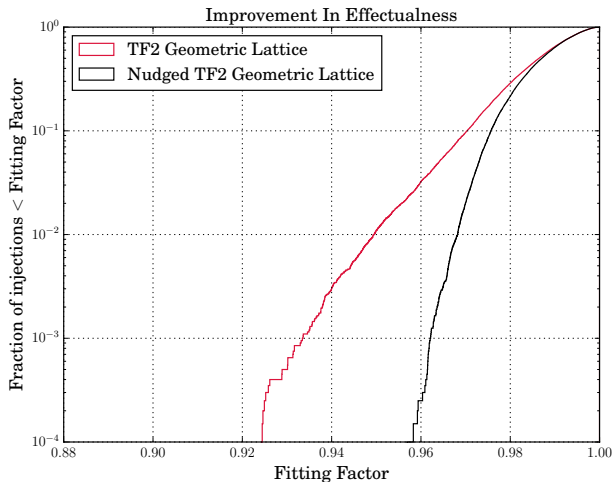


Figure 4.5: The improvement in template bank effectualness from applying the template nudging algorithm to a **TaylorF2** (**TF2**) geometric lattice. This used 20,000 **IMRPhenomD** injections drawn from a uniform component mass and aligned BH spin distribution. The maximum fitting factors of the lowest 0.1% of injections improved from approximately 0.93 to 0.96. Image and caption are copied from [145].

coordinate  $y$  was normalized and ranged from 0 to 1. We divided the parameter space into 40 slices in this direction and obtained a rectangular grid in the  $x$ - $y$  plane with 12,000 cells.

We tested this setup with a set of randomly distributed points. In the limit of having only one cell we compute all mismatches smaller than 3% correctly. If the cells became too small, some of mismatches smaller than 3% will not be detected. This happened if the cells were so small that overlapping templates were not in neighboring cells anymore, but, for instance, in next-nearest neighboring cells.

### 4.3 Results

To test the template nudging algorithm we seeded it with a geometric lattice **TF2** template bank containing 174,000 templates. Both the initial seed bank and the nudged bank were then tested against a set of 20,000 random **IMRPhenomD** injections. For the nudged bank only 3% of injections had a fitting factor less than 97%, compared to 10% for the original seed geometric bank (see Figure 4.5). For comparison, building a stochastic bank targeting 97% *minimal match* (i.e. 1-maximal mismatch), required 220,000 templates, with only 0.1% of templates having a fitting factor less than 97% for the same injection set.

For this comparison, matches were calculated between 30–1024Hz using a PSD [3] built from the harmonic mean of the Hanford and Livingston PSDs (see Section 1.3) taken within a few days of GW150914 and thus comparable to what shown in [18]. The stochastic bank was generated using `lalapps_cbc_sbank` [197, 33, 70, 89, 5], using with a convergence criteria of rejecting 97% trial templates. The stochastic algorithm is able to use **IMRPhenomD** templates directly to calculate matches. The **TaylorF2** lattice was generated using `pycbc_geom_aligned_bank` [197, 62, 70, 89], constructed with a two dimensional lattice such that each lattice point had a maximal mismatch no larger than 3%. As can be seen in Figure 4.5, this target was not attained for the **IMRPhenomD** test signals. A known metric is required to determine the geometric lattice. Since no metric is known for the **IMRPhenomD** templates we used **TaylorF2** 3.5PN waveforms [40, 58, 5] for which an analytical metric can be calculated. Although the lattice

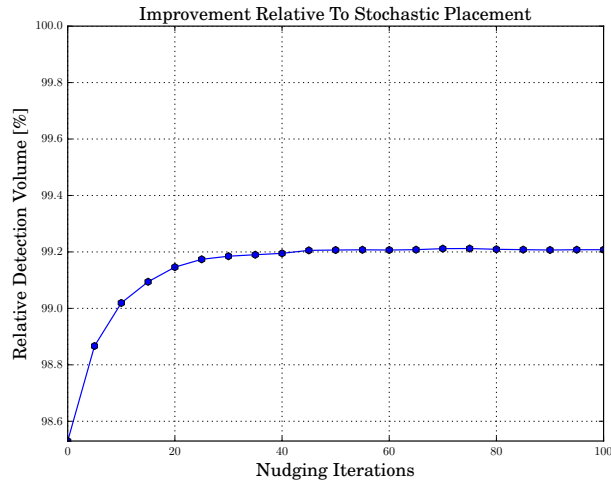


Figure 4.6: The relative detection volume of the nudged bank versus the stochastic bank,  $100\% * V_{nudged}/V_{stochastic}$ , was tracked every five iterations of the template nudging algorithm using the same set of 20,000 **IMRPhenomD** injections drawn from a uniform component mass and aligned BH spin distribution. The improvement settles to a constant value after approximately 40 iterations. Image and caption are copied from [145].

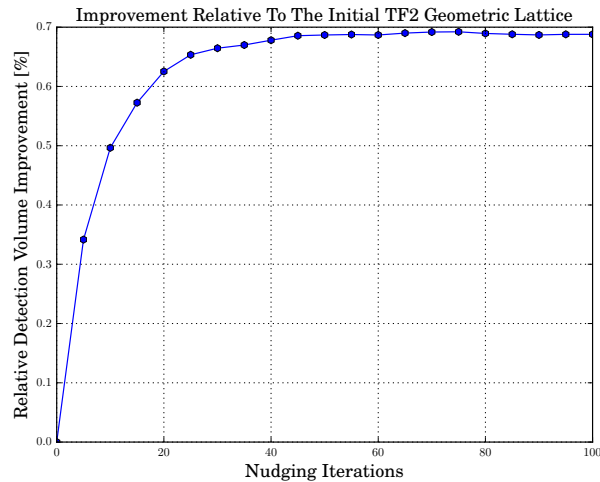


Figure 4.7: The relative detection volume improvement of the nudged bank versus the original **TaylorF2 (TF2)** geometric lattice bank,  $100\% * (V_{nudged}/V_{original} - 1)$ , was tracked every five iterations of the template nudging algorithm using the same 20,000 **IMRPhenomD** injections drawn from a uniform component mass and aligned BH spin distribution. Image and caption are copied from [145].

locations were calculated using **TaylorF2** waveforms, these were subsequently swapped out with **IMRPhenomD** templates when testing the effectualness and this results in a loss of effectualness.

The template nudging algorithm was applied for 100 iterations using one cross-section with at least 16 surface points to approximate individual template isosurfaces for the nudging calculations. The effectualness and improvement in the relative detection volume between successive intermediate nudges was quantified by recovering a set of 20,000 **IMRPhenomD** injections drawn from a uniform component mass and BH spin distribution (see Figures 4.6 and 4.7).

Within each iteration, templates were nudged in parallel for the purposes of reducing computation time. Studying the effect of the template nudge factor on the convergence of the method revealed that a template nudge factor of 5% produced the largest improvements in the template bank’s effectualness in the first iteration relative to template nudge factor of 1% or 0.05%. However, in later iterations the variance of the improvement of the recovered fitting factors was also higher and a poorer fitting factor was recovered in the anti-aligned high mass regions of the bank relative to those produced by template nudge factor of 1%. We used a composite approach to improve the convergence of the method, wedding the advantages of using a bigger template nudge factor in the first iterations to the advantages of the greater precision of smaller template nudge factors in later iterations. Hence, we applied the template nudge algorithm in two batches of 50 iterations per template nudge factors: 5% and 1%. After 100 nudging iterations, the coverage had improved by 3% and the relative detection volume had increased by 0.69%.

In order to extract an additional 1% of coverage and an additional 0.80% relative detection volume beyond what is achieved with the nudging, we *polished* the nudged template bank by adding 20,000 templates via a final stochastic placement to fill in any remaining holes. This produced a bank with overall fitting factors comparable to the stochastic bank, but with only 194,000 templates compared to the 220,000 templates required via the `lalapps_cbc_sbank` algorithm. Therefore it is possible to achieve equivalent template bank effectualness and detection volume with 26,000 fewer templates than would be required by the purely stochastic method.

Figure 4.8 compares the result of injecting 40,000 **IMRPhenomD** signals into the nudged **TF2** geometric lattice and the original **TF2** geometric lattice. The nudged **TF2** geometric lattice has a more even distribution of recovered fitting factors. The template nudging algorithm improves regions with poor fitting factors by repositioning templates from over-covered regions. In principle this allows the attainment of a desired minimum fitting factor across the entire parameter space with fewer templates. However, the template nudging algorithm as currently conceived does not remove templates from the bank. In some cases the nudging can result in templates from over-covered regions being nudged to nearby boundaries and piling up there. An example of this is shown in the lower right panel of Figure 4.8. This highly anti-aligned spin region of the NSBH parameter space, indicated by the yellow boxes in the other panels, is over-covered by the original **TF2** geometric lattice, obtaining recovered fitting factors close to  $\sim 100\%$ . In this region the excess templates are nudged to the boundaries and build up there, without reducing the fitting factors.

## 4.4 Conclusions

We have shown how the number of gravitational wave templates needed to search a region of parameter space can be reduced by repositioning templates. In particular, we successfully implemented a method to reduce the number of templates required by the algorithm `lalapps_cbc_sbank` to cover an NSBH single-aligned spin parameter space. This resulted in a 12% reduction in the number of templates. For comparison, the hybrid method (utilized to

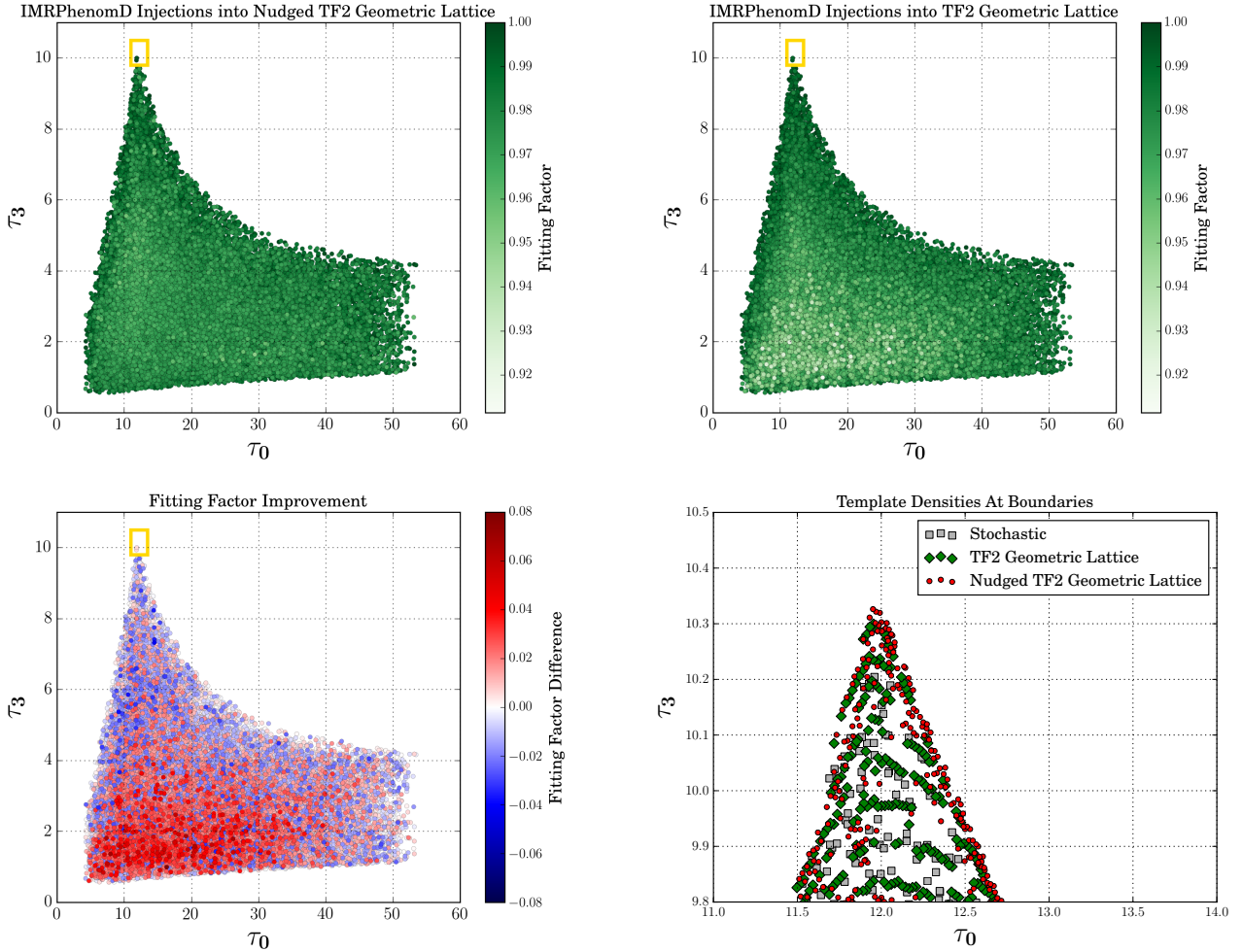


Figure 4.8: Comparison of fitting factors for the template nudging algorithm. Coordinates are the chirp times given in Section 4.2.1. The top row shows the fitting factors for the nudged **TF2** geometric lattice (left) and the original **TF2** geometric lattice (right). The fitting factors are seen to be more uniform across the nudged bank. The difference in fitting factor is displayed in the bottom left panel. The regions of improvement (in red) are seen to correspond largely with the regions of insufficient fitting factor in the original geometric lattice. The lower right panel shows the template locations for three different template distributions in the highly anti-aligned spin region denoted by the yellow box in the other panels. In this region the nudging pushes templates to nearby boundaries and does not reduce the number of templates in a region that is over-saturated by the geometric lattice. Images and caption are copied from [145].

build the O1 bank [15] and the O2 bank [89]) required 5% fewer templates than the stochastic method when used to build a binary-black-hole bank [70]. Given that 60% of the templates in the O2 CBC template bank are in the NSBH mass range considered in this chapter, applying the template nudging algorithm in this subspace alone would already reduce the size of the bank placed on the entire mass range by 7% without sacrificing effectualness. Assuming that the percentage reduction in the number of templates is uniform across the parameter space, then we could expect an overall reduction of approximately 50,000 templates from the 399,995 template O2 bank.

The template nudging is seen to be most effective at repositioning templates from over-covered regions to under-covered regions. This is less effective in regions very close to boundaries of the desired parameter space. In some cases the shifted templates can accumulate near the boundaries as seen in the lower right panel of Figure 4.8. Once a template is nudged such that one or more of its isosurface points exceeds the border of the bank, there is currently no mechanism to nudge the template away from that border or to remove it entirely.

For the nudging the template bank is split into two-dimensional planes and the nudging takes place within each plane. The algorithm does not nudge templates between the planes and thus if there is a hole in one of the planes the method is not able to fill it with excess templates from another plane. Such banks may require additional templates after nudging in order to match the effectualness and detection volume that can be produced by a stochastic method. In our example, this would occur specifically when these holes are in regions of the bank which require nudging the  $\tau_2$  coordinate since this version of the template nudging algorithm only nudges templates on the  $\tau_0 - \tau_3$  plane. It is non-trivial to remove this restriction since the template isosurface cross-sections in the  $\tau_0 - \tau_2$  and the  $\tau_2 - \tau_3$  planes are non-ellipsoidal and would require modifying how the algorithm samples the isosurface boundary points.

Further work is needed to adapt this method to the entire aligned-spin CBC parameter space. Currently the algorithm only places templates in the NSBH and Binary Neutron Star (BNS) mass range. Extending this region would require readdressing the following two points: 1) defining the borders of the targeted chirp-time parameter space and 2) obtaining a uniform transformation across the targeted chirp-time parameter space to the two dimensional grid needed to apply our modified NCA method. In the example considered in this chapter, these two issues were solved *ad hoc*, but we believe the method is readily adaptable to other parameter regions.

An additional computational challenge is scaling the algorithm to nudge template banks with millions of templates. The preliminary application of the template nudging algorithm to the aligned-spin CBC parameter space required the use of a high-throughput computing cluster and 150,000 CPU hours. Generating the template isosurface cross-sections in the absence of a general mismatch metric (analytic or otherwise) is particularly computationally expensive. The template nudging algorithm is considerably faster if there is a reliable (and computationally efficient) way to calculate the metric. By nudging purely BNS banks (where there is a known analytic expression of the metric), we were able to nudge an under-saturated stochastic bank on a single Lenovo Thinkpad T450s Ultrabook laptop. Similarly, the template banks used for Fermi  $\gamma$ -ray binary pulsar searches in [216] (which contained tens of millions of templates) could be constructed by the NCA method in a few hours on one HUAWEI RH1288 v3 Server with two 14 core CPUs since there is an analytic expression for the metric. Therefore, it is highly desirable to obtain a computationally efficient way to calculate the metric in order to apply the template nudging algorithm to larger CBC parameter spaces, or detectors with improved sensitivities.

The so-called  $\theta$  coordinates produce a computationally efficient method for calculating the numeric approximation of the CBC mismatch metric [207, 248, 33, 230]. These coordinates are only dependent on the masses and effective spin and may produce more uniform template



isosurfaces, better suited to the template nudging algorithm. Running the template nudging algorithm with these flatter coordinates may lower the computational cost and further reduce the final number of required templates for the CBC template bank.

While our current implementations of the metric agnostic template nudging algorithm are computationally inefficient, they are still a lot more flexible than the original metric dependent NCA method [120]. As long as there is a coordinate system in which cross-sections of individual template isosurfaces can be reduced to a collection of two dimensional ellipsoids, this bootstrap metric construction method is completely generalizable to any current or future CBC template bank parameter space. This makes it a potentially versatile option for building higher dimensional template banks that include the effects of precession, tidal deformation, eccentric orbits, and higher order modes.

## 4.5 Acknowledgments

The text presented in this chapter I wrote collaboratively with Henning Fehrmann, Badri Krishnan, Alex B. Nielsen. The template nudging algorithm I developed with Henning Fehrmann and Franz Harke. The neighboring cell algorithm was originally developed by Henning Fehrmann and Holger J. Pletsch. Additional feedback on the original manuscript was provided by Tito Dal Canton, Sebastian Khan and Hirotaka Yuzurihara. The original paper has LIGO document number LIGO-P1700427.



## CHAPTER 5

# METHOD FOR FLATTENING CBC PARAMETER SPACES

As shown in Chapters 2, 3 and 4, the choice of coordinates for the parameter space has a dramatic impact on the efficiency of template bank construction<sup>1</sup>. Ideally these coordinates should be flat, such that the template isosurfaces are hyper-spheres or hyper-ellipsoids. Flat coordinates are also a prerequisite for the construction of geometric lattice template banks (see Section 2.1). And this is partly the reason why a stochastic template placement had to be used in Chapter 3. The  $\xi$  coordinates (Eq. 2.20 in Section 2.1[63]) flattened the aligned spin **TaylorF2** 3.5 PN CBC parameter space via a principle component analysis. This method is powerful, however the solution requires expensive numerical monte carlo simulations every time the boundaries of the parameter space change[63].

In this chapter we present preliminary work on a new alternative analytic method for flattening CBC coordinate spaces that does not require principle component analysis (see Eq. 2.20 or [201, 152]). We demonstrate this method on a **TaylorF2** 2.5 PN non-spinning BNS template bank parameter space, to obtain three *Gaussian Normal Coordinates*; solutions to the geodesic equation (Eq. 5.5). However, the method is generalizable to higher dimensional CBC parameter spaces like the precessing NSBH parameter space (e.g. Chapter 3).

The outline of this chapter is as follows. The first section (5.1) provides a background on Gaussian normal coordinates. The second section (5.2) derives a set of Gaussian normal coordinates for a subspace of the 2.5 PN **TaylorF2** non-spinning parameter space. The final section (5.3), summarizes the results of the previous sections and outlines the subsequent analysis that must be made to apply this coordinate flattening method to higher dimensional parameter spaces like the precessing NSBH inspiral-merger-ringdown parameter space.

## 5.1 Gaussian normal coordinates

A geodesic  $x_\mu(\lambda)$  described by an *affine parameter*  $\lambda$ , on a point,  $p$ , on a curved Riemannian manifold,  $M$ , described by the coordinate system  $\{x_i\}$ , is the straightest line possible that can be drawn at that point in the manifold<sup>2</sup>. Moreover,  $x^\mu(\lambda)$  is defined to curve such that its tangent vectors  $T^\mu = \frac{dx^\mu}{d\lambda}$  are parallel propagated against itself the satisfying the following condition:

$$T^\mu \nabla_\mu T^\nu = 0. \quad (5.1)$$

---

<sup>1</sup>This chapter is a summary of the work I have done with Badri Krishnan to develop a method for finding flat coordinates to describe CBC systems. We are expecting to publish our results shortly after submitting this thesis.

<sup>2</sup>Legal disclaimer: “This section is paraphrased from [258]. The use of these materials is protected under ‘Fair Use’ (UrhG §24,70,63) and consistent with the requirements of § 6 Abs. 1 PromO”.

A vector  $v^\nu$  is said to be *parallel transported* along  $T^\mu$  if the following condition is true

$$T^\mu \nabla_\mu v^\nu = 0. \quad (5.2)$$

In Eqs. 5.1 and 5.2,  $\nabla_\mu$  denotes the *covariant derivative* which determines the derivative along a tangent vector of a manifold. The covariant derivative of the tangent vector  $\nabla_\mu T^\nu$  can be expressed as a combination of via the partial derivative  $\partial_\mu$  and the *Christoffel symbols*,  $\Gamma_{\sigma\kappa}^\nu$ , which describe the *metric connection* (i.e. how vectors expressed in a given set of coordinates rotate for different points of the manifold),

$$\nabla_\kappa T^\nu = \partial_\kappa T^\nu + \Gamma_{\sigma\kappa}^\nu T^\sigma \quad (5.3)$$

$$\Gamma_{\sigma\kappa}^\nu = \frac{1}{2} g^{\nu\alpha} (\partial_\sigma g_{\kappa\alpha} + \partial_\kappa g_{\sigma\alpha} - \partial_\alpha g_{\sigma\kappa}). \quad (5.4)$$

A parametrization of  $T^\mu$  that satisfies Eq. 5.1 is called an *affine parametrization*. The geodesic  $x^\mu(\lambda)$  can be described as a solution to the following equation,

$$\frac{d^2 x^\nu}{d\lambda^2} + \Gamma_{\sigma\kappa}^\nu \frac{dx^\sigma}{d\lambda} \frac{dx^\kappa}{d\lambda} = 0. \quad (5.5)$$

It can be shown that a particle at point  $p$  with a velocity  $v^\mu$  in a manifold  $M$  will have a unique geodesic.

Geodesics provide a convenient way to choose coordinates that locally flatten out a parameter space. Suppose there is a point  $p$  on the  $n$  dimensional Riemannian manifold  $M$ . The geodesic  $x^\mu(p)$  that intersects  $p$  has the tangent vector  $T^\mu \in V$ , where  $V$  denotes the tangent space of  $M$  at  $p$ . We can also parallel transport (see Eq. 5.2) the orthonormal basis  $\{e_i^\mu | e_i^\mu e_j^\nu = \delta_{ij}\}$  at  $p$  along the geodesic to obtain basis at all points in a neighborhood of  $p$ .

For the purposes of defining a new local coordinate system for point  $p$  using these geodesics, we define the *exponential map*  $E : V \rightarrow M$ ,

$$\begin{aligned} E: \quad V &\mapsto M \\ T^\mu(p) = c^i e_i^\mu(p) &\mapsto q = x(p|\lambda = 1). \end{aligned} \quad (5.6)$$

This transformation takes a tangent vector  $T^\mu(p) \in V$  of a point  $p \in M$  and maps it to the point  $q \in M$  that is unit affine parameter ( $\lambda = 1$ ) away from  $p$  along the geodesic  $x(p)$  that goes through  $p$ . If  $T^\mu(p)$  is multiplied by a scalar  $a$ , then  $E(T^\mu(p))$  will transform that vector to the point  $q'$  that is  $\lambda = a$  away on the geodesic. In other words, suppose the original tangent vector  $T^\mu(p)$  can be decomposed into a sum of components  $\{c_i\} \in \mathbb{R}^n$  on an orthonormal basis  $\{e_i^\mu(p)\} \in V$  ( $T^\mu(p) = c^i e_i^\mu(p)$ ). The mapping  $E(T^\mu(p))$  takes the components  $\{c_i\}$  and transforms them into a new point in the manifold  $q \in M$ . Therefore the mechanics of this map takes the components of the tangent vector and transforms them to a set of coordinates representing the point  $q$ . These coordinates are only valid locally for when the geodesics don't intersect.

This transformation is useful because it allows us to walk along the geodesic. We need this map in order to build our new coordinates. In this chapter we will derive a variant of these ‘‘Gaussian normal coordinates’’ starting with a hypersurface of constant chirp mass which is the best measured quantity for GW produced by BNS systems [201, 152].

Rather than a point suppose there is an  $n - 1$  dimensional hypersurface  $S$  imbedded in the  $n$  dimensional manifold  $M$ , with normal surface vector,  $n_\mu$ . Then we can construct the geodesic starting at every point of  $S$  starting initially orthogonal to  $S$ . This will yield a coordinate system  $x_\mu$  in a neighborhood of  $S$ .

## 5.2 Flattening CBC parameter spaces

We would like to apply this method for the purposes of constructing CBC template banks. In this parameter space manifold for describing CBC systems, the tradition parameters used to describe CBC signals (e.g.  $\{M, \eta\}$ ) are not oriented along the geodesics which results in non-uniform template densities. The chirp time coordinates  $\tau_0, \tau_3$  (see Eq. 1.31) have been shown to approximately flatten out the BNS parameter space (see Section 1.1.5). However the template densities in these coordinates are still uneven for higher mass CBC template banks, particularly for precessing CBC template banks (see Chapter 3) [146].

A flat set of Gaussian normal coordinates  $\{x_i\}$  of a mismatch metric,  $g_{ij}$ , can be found as solutions to the geodesic equation. In practice solving Eq. 5.5 can be very difficult, particularly if the metric  $g_{ij}$  is not diagonalized. Hence brute force attempts at solving the geodesic equation can often be futile. The problem becomes more tractable when using coordinates that already approximately diagonalize the matrix. It has been shown that for the BNS aligned spin bank, template densities are approximately uniform along curves of constant chirp mass  $\mathcal{M}$  (see Eq. 1.22) [201, 152]. Therefore in this proof of concept we examine the frequency domain diagonalizable mismatch metric describing 2.5 PN **TaylorF2** aligned spin inspiral BNS systems [248], setting the spin of the component masses to zero (see Eq. 5.21).

$h(f)$  depends on the intrinsic parameters for describing these systems are the component masses  $M_1, M_2$  and their individual spins  $S_1, S_2$ ,

$$\tilde{h}(f) = \tilde{h}_C(f) \cos \phi_0 + \tilde{h}_S(f) \sin \phi_0 \quad (5.7)$$

$$\tilde{h}_C(f) = i\tilde{h}_S(f) = \mathcal{N} f^{-7/6} \exp i [\psi_{\theta^{2.5}}(f) + t_C f]. \quad (5.8)$$

The quantity  $\mathcal{N}$  is a normalization constant calculated such that  $\langle h|h \rangle = 1$  (see Eq. 1.56).

As a proof of concept for our method we calculate Gaussian normal coordinates utilizing the  $\theta^{(2.5)}$  coordinates [248]<sup>3</sup> (where the spin of the component masses is set to zero) as the basis for our Christoffel symbol calculations,

$$\psi_{\theta^{(2.5)}}(f) = \sum_i \theta_i^{(2.5)} \psi^i(f) \quad (5.9)$$

$$\psi_1(f) = f^{-5/3} \quad (5.10)$$

$$\psi_2(f) = f^{-1} \quad (5.11)$$

$$\psi_3(f) = f^{-2/3} \quad (5.12)$$

$$\psi_4(f) = f^{-1/3} \quad (5.13)$$

$$\psi_5(f) = \log f \quad (5.14)$$

$$\theta_1^{(2.5)} = \frac{3}{128\eta} (\pi M)^{-5/3} \quad (5.15)$$

$$\theta_2^{(2.5)} = \frac{1}{384\eta} \left( \frac{3715}{84} - 55\eta \right) (\pi M)^{-1} \quad (5.16)$$

$$\theta_3^{(2.5)} = \frac{1}{128\eta} \left[ (113 - 86\eta) \chi_S + 113\chi_a \frac{M_2 - M_1}{M} - 48\pi \right] (\pi M)^{-2/3} \quad (5.17)$$

$$\theta_4^{(2.5)} = \frac{\pi}{128\eta} \left[ \frac{15293365}{508032} + \frac{27145}{504}\eta + \frac{3085}{72}\eta^2 \right]$$

<sup>3</sup>In more sophisticated examples we will apply our method to higher order PN approximates that were discussed earlier in the thesis.

$$+ \left( 30 + \frac{275}{4}\eta \right) (\chi_S^2 - \chi_a^2) \Big] (\pi M)^{-1/3} \quad (5.18)$$

$$\theta_5^{(2.5)} = \frac{\pi}{128\eta} \left( \frac{38645}{252} + 5\eta \right). \quad (5.19)$$

The quantities  $M$  and  $\eta$  are the total mass and dimensionless mass ratio of the BNS system. The individual component mass spins are recombined into the *symmetric* and *anti-symmetric* spins  $\{\chi_S, \chi_a\}$ ,

$$\chi_S = \frac{1}{2} \left( \frac{S_1}{M_1^2} + \frac{S_2}{M_2^2} \right) \quad (5.20)$$

$$\chi_a = \frac{1}{2} \left( \frac{S_1}{M_1^2} - \frac{S_2}{M_2^2} \right). \quad (5.21)$$

As a proof of concept for our method for flattening CBC parameter space we express our mismatch metric in these  $\theta^{(2.5)}$  coordinates which is expressed in terms of the PSD moments  $\mathcal{J}$ , and the waveform phase PN coefficients  $\{\psi_\alpha\}$  (see Eqs. 2.18<sup>4</sup>) [206]. To filter signals, we also project out the coalescence time  $t_C$  (the zeroth index) out of the matrix  $\gamma_{\alpha\beta}$  to obtain the matrix  $G_{\alpha\beta}$  (see Section 1.2),

$$G_{\alpha\beta} = \gamma_{\alpha\beta} - \frac{\gamma_{0\alpha}\gamma_{0\beta}}{\gamma_{00}} \quad (5.22)$$

$$\gamma_{\alpha\beta} = \frac{1}{2} (\mathcal{J}(\psi_\alpha\psi_\beta) - \mathcal{J}(\psi_\alpha)\mathcal{J}(\psi_\beta)) \quad (5.23)$$

$$\mathcal{J}(a(x)) = \frac{1}{I(7)} \int_{x_L}^{x_U} dx \frac{a(x)x^{-7/3}}{S_N(xf_0)} \quad (5.24)$$

$$\mathcal{I}(q) = \int_{x_L}^{x_U} dx \frac{x^{-q/3}}{S_N(xf_0)}. \quad (5.25)$$

Here  $x_U * f_0$  and  $x_L * f_0$  specify the maximum and minimum frequencies that define the sensitive bandwidth of the detector.

Suppose we choose the  $(n - 1 = 2)$  dimensional hypersurface  $S$  mentioned in Section 5.1 to be an hypersurface of constant  $\mathcal{M}$ . A constant  $\mathcal{M}$  in these  $\theta^{(2.5)}$  coordinates [248] is a two dimensional hypersurface in these coordinates. However, these hypersurfaces are one dimensional in  $\{\mathcal{M}, \eta\}$  coordinates. The first two  $\theta^{(2.5)}$  coordinates  $\{\theta_1^{(2.5)}, \theta_2^{(2.5)}\}$  are independent of the spin of the component masses. This makes  $\{\theta_1^{(2.5)}, \theta_2^{(2.5)}\}$  suitable candidates to form the orthonormal coordinates for the two dimensional hypersurface  $S$ .

As a proof of concept of our coordinate construction method, we shall look at the subspace  $\{\theta_1^{(2.5)}, \theta_2^{(2.5)}, \theta_3^{(2.5)}\}$ . In this subspace, the metric  $g_{ij}$  is a  $(3 \times 3)$  matrix. However as mentioned previously, there are only two intrinsic coordinates  $\{\mathcal{M}, \eta\}$ . Therefore we can project  $g_{ij}$  onto the  $(2 \times 2)$  physical subspace  $\{\mathcal{M}, \eta\}$ . This  $(3 \times 3)$  matrix  $g_{ij}$  can be orthonormalized via the eigenvalues  $e_k$  and associated eigenvectors  $P_i^k$  of the  $(2 \times 2)$  matrix subspace  $\{\theta_1^{(2.5)}, \theta_2^{(2.5)}\}$ . This procedure will ultimately yield the Gaussian normal coordinates  $x_i = \{x_1, x_2\}$ ,

$$g_{ij}^{2 \times 2} = \sum_{\alpha=1}^2 e_k P_i^k P_j^k. \quad (5.26)$$

Metrics are by definition symmetric, therefore the eigenvalues will take the following form where  $e_- = e_1$  and  $e_+ = e_2$ ,

$$e_{\mp} = \frac{1}{2} \left( g_{11} + g_{22} \mp \sqrt{(g_{11} - g_{22})^2 + 4g_{12}^2} \right). \quad (5.27)$$

---

<sup>4</sup>The use of these previous definitions is the same modulo some constant factors that are different relative to this previous definition.

The diagonal representation of this  $2 \times 2$  metric in its eigenbasis is a diagonal matrix containing these eigenvalues  $e_i$ .

This diagonalization of the matrix allows us to approximate the metric  $g_{ij}$  as the sum of the identity matrix  $\delta_{ij}$  and  $K_{ij}$  because as was shown in [248, 201, 152],  $g_{ij}$  is approximately flat and therefore  $K_{ij}$  will be small,

$$g_{ij} = \delta_{ij} + K_{ij}. \quad (5.28)$$

The inverse metric,  $g^{ij}$  can be expressed as  $\delta^{ij} - K^{ij}$ . As will be shown in Eq. 5.38, this linear approximation dramatically simplifies the calculation of Eq 5.4.

Suppose we would like to develop three coordinates for this parameter space and we choose  $\{\theta_1^{(2.5)}, \theta_2^{(2.5)}, \theta'\}$ . We diagonalize the subspace spanned by  $\{\theta_1^{(2.5)}, \theta_2^{(2.5)}\}$  using  $\{x_1, x_2\}$ . This yields the metric in the following form:

$$ds^2 = dx_1^2 + dx_2^2 + \alpha(d\theta')^2 + 2\beta_i dx_i d\theta' \quad (5.29)$$

$$d\theta' = \frac{\partial\theta'}{\partial x_1} dx_1 + \frac{\partial\theta'}{\partial x_2} dx_2, \quad (5.30)$$

$$g'_{ij} = \begin{matrix} & \begin{matrix} x_1 & x_2 & \theta' \end{matrix} \\ \begin{matrix} x_1 \\ x_2 \\ \theta' \end{matrix} & \begin{bmatrix} 1 & 0 & \beta_0 \\ 0 & 1 & \beta_1 \\ \beta_0 & \beta_1 & \alpha \end{bmatrix} \end{matrix}. \quad (5.31)$$

For notational convenience we define the quantities  $\Xi_i$ ,

$$\Xi^i = \frac{d\theta'}{dx_i} \quad (5.32)$$

$$\partial^j \Xi^i = \frac{d^2\theta'}{dx_i dx_j}. \quad (5.33)$$

Combining Eqs. 5.30 and 5.35 allows us to project  $\theta'$  into the  $\{x_1, x_2\}$  plane,

$$\begin{aligned} ds^2 &= dx_1^2 + dx_2^2 + \alpha (\Xi_1 dx_1 + \Xi_2 dx_2)^2 + 2\beta_i dx_i (\Xi_1 dx_1 + \Xi_2 dx_2) \\ &= dx_1^2 + dx_2^2 + \alpha (\Xi_1 dx_1 + \Xi_2 dx_2)^2 + 2(\beta_1 dx_1 + \beta_2 dx_2) (\Xi_1 dx_1 + \Xi_2 dx_2) \\ &= dx_1^2 + dx_2^2 + (\alpha \Xi_1^2 + 2\beta_1 \Xi_1) dx_1^2 + (\alpha \Xi_2^2 + 2\beta_2 \Xi_2) dx_2^2 \\ &\quad + (2\Xi_1 \Xi_2 + 2\beta_1 \Xi_2 + 2\beta_2 \Xi_1) dx_1 dx_2. \end{aligned} \quad (5.34)$$

Therefore we can express the small perturbation matrix  $K_{ij}$  in the following way:

$$K_{ij} = \begin{matrix} & \begin{matrix} x_1 & x_2 \end{matrix} \\ \begin{matrix} x_1 \\ x_2 \end{matrix} & \begin{bmatrix} (\alpha \Xi_1^2 + 2\beta_1 \Xi_1) & (\Xi_1 \Xi_2 + \beta_1 \Xi_2 + \beta_2 \Xi_1) \\ (\Xi_1 \Xi_2 + \beta_1 \Xi_2 + \beta_2 \Xi_1) & (\alpha \Xi_2^2 + 2\beta_2 \Xi_2) \end{bmatrix} \end{matrix}. \quad (5.35)$$

Let us now turn to the Christoffel symbols. Note that in Eq. 5.4, since the derivatives of the metric are all linear in  $K$ , we can approximate the inverse metric simply as  $\delta^{ij}$ . This is an important technical simplification since it allows us to avoid calculating the inverse metric. The nonzero Christoffel symbols for  $g_{ij}$  are as follows:

$$\Gamma_{11}^i \approx \frac{1}{2} \delta^{i\alpha} (\partial_1 K_{1\alpha} + \partial_1 K_{1\alpha} - \partial_\alpha K_{11}) \quad (5.36)$$

$$= \frac{1}{2} \delta^{i1} \partial_1 K_{11} + \frac{1}{2} \delta^{i2} (2\partial_1 K_{12} - \partial_2 K_{11}) \quad (5.37)$$

$$\begin{aligned} &= \delta^{i1} (\alpha \Xi_1 \partial_1 \Xi_1 + \beta_1 \partial_1 \Xi_1) \\ &\quad + \delta^{i2} (\partial_1 \Xi_1 (-\alpha \Xi_1 / 2 - \beta_1 / 2 + \Xi_2^2 + \beta_1) + \partial_1 \Xi_2 (2\Xi_1 \Xi_2 + \beta_1)). \end{aligned} \quad (5.38)$$

Now we solve the geodesic equation with the initial conditions,

$$\frac{\partial x^i}{\partial \lambda}(\lambda = 0) = (0, 1), \quad x^i = (0, 0), \quad (5.39)$$

where the geodesics are approximately oriented along  $x_1$  and  $x_2$ ,

$$\begin{aligned} \frac{d^2 x^i}{d\lambda^2} &= -\Gamma_{jk}^i \frac{dx^j}{d\lambda} \frac{dx^k}{d\lambda} \\ \frac{d^2 x^i}{d\lambda^2} \Big|_{\lambda=0} &= -\Gamma_{11}^i \frac{(dx^1)^2}{d\lambda^2}. \end{aligned} \quad (5.40)$$

Now we obtain the following system of differential equations to linear order in  $\lambda$  that describe the dependence of  $\theta'$  on  $\{x_1, x_2\}$

$$\begin{aligned} \frac{dx^1}{d\lambda} &= -(\alpha \Xi_1 \partial_1 \Xi_1 + \beta_1 \partial_1 \Xi_1) \lambda + \mathcal{O}(\lambda^2) \\ \frac{dx^2}{d\lambda} &= 1 - (\partial_1 \Xi_1 (-\alpha \Xi_1 / 2 - \beta_1 / 2 + \Xi_2^2 + \beta_2) + \partial_1 \Xi_2 (2\Xi_1 \Xi_2 + \beta_1)) \lambda + \mathcal{O}(\lambda^2). \end{aligned} \quad (5.41)$$

As a final step, we must integrate Eqs. 5.41 and solve for  $\{x_1(\lambda), x_2(\lambda)\}$  this system numerically necessary to obtain an expression for  $\theta'$  as a function of  $\{x_1, x_2\}$ . Once solved, these Gaussian normal coordinates  $\{x_1, x_2\}$  must be compared to the coordinates that are derived in [63, 201, 152]. We must also verify that the template isosurfaces in  $\{x_1, x_2\}$  are ellipses and do not have curved features, which will be key for the optimal placement of geometric lattices and the implementation of the template nudging algorithm (see Chapter 4).

### 5.3 Conclusions

This was an illustration of this method on a simple example CBC parameter space. To apply this method to higher dimensional parameter spaces, we can repeat this procedure with three or higher dimensional imbedded hypersurfaces. This could be as simple as considering the higher order  $\theta^{(2.5)}$  coordinates [248] that were not considered in the previous section, or we could add additional degrees of freedom to the parameter space like the component mass spins. The flexibility of this semi-analytic method also allows us to apply this procedure to parameter spaces that include higher order PN corrections and precessing parameters (see Section 1.1.6).

This is still a work in progress and we still need to test how the coordinates obtained from this method compares against the  $\xi$  coordinates used to build a 3.5 PN **TaylorF2** geometric lattice (see Section 2.1) or the coordinates developed in [201, 152]. We must verify that the maximal mismatch isosurfaces in these Gaussian normal coordinates are ellipsoidal and lack the concave features like those that can be seen in chirp time coordinates (see Figures 4.3 and 4.4). To compare these coordinate construction methods we will place geometric lattices in these the different coordinate systems and compare the template densities and effectualness of the resulting template bank distributions. While currently our coordinates are not entirely analytic (see Eq. 5.41), these coordinates are potentially more flexible for higher dimensional parameter spaces while minimizing computational costs.



I have contributed to the field of study of compact binary coalescences by improving methodology that is used to construct template banks.

Previously, there were no stochastic template banks that could detect face-on precessing compact binary coalescence systems to an adequate maximal mismatch threshold. Building such a bank required modifying the stochastic method for compact binary coalescence template placement to handle extremely dense template bank parameter spaces in order to place the millions of templates necessary to saturate the face-on precessing neutron-star–black-hole parameter space. I accomplished this by innovating the way the stochastic template placements parallelized on the computing cluster. This required studying how to mitigate the effects of template bank gridlines, the artificially dense bank placement artifacts in subspaces of the parameter space.

Ultimately, I found that these gridlines could be removed if a different bank placement algorithm was applied, template nudging. By adapting the Neighboring Cell Algorithm that was previously developed for Fermi  $\gamma$ -ray pulsar searches to the compact binary coalescence parameter space, I demonstrated that the effectualness of a compact binary coalescence template bank could be improved without placing additional templates. By repositioning templates from over-saturated regions of the template bank to under-saturated regions, the template nudging algorithm has the ability to eliminate gridlines from stochastic, geometric, or hybrid template banks. One of the main challenges of this work was to abstract the Neighboring Cell Algorithm method to work in a parameter space where there is no known analytic expression for the waveform mismatch metric, and generic numerical approximations of that metric are ill-conditioned. I overcame this challenge by reducing the aligned spin neutron-star–black-hole parameter space to a series of two dimensional planes. As long as a coordinate system for the targeted compact binary coalescence parameter space can be conceived such that cross-sections of the template isosurface volume are ellipsoidal, the template nudging algorithm method can be adapted to improve the effectualness and detection volume of the template bank.

Both the work in constructing the face-on precessing template bank, and developing the template nudging algorithm revealed a problem in the coordinates used for the template placement. Without a flat parameter space for generic compact binary coalescence systems, placing template banks over the entire LIGO-Virgo search parameter space can be prohibitively computationally expensive and may over-saturate the targeted template bank parameter space. Furthermore, searches using these immense template banks will be even more computationally expensive. Therefore, I worked to develop a methodology for finding flat coordinates for non-spinning binary-neutron-star systems which can be readily abstracted to generic precessing compact binary coalescence systems.

Equipped with these three developments, the next step is to construct a generic precessing compact binary coalescence template bank to cover the binary-neutron-star, neutron-star-black-hole and binary-black-hole regions of the compact binary coalescence search parameter space for LIGO-Virgo. As a starting point, it would be wise to first restrict the problem to a subspace of neutron-star-black-hole systems since they have not been detected yet and the signal-to-noise-ratio of these waveforms are dominated by the late-inspiral, merger and ring-down portions of the CBC evolution. After applying the correct coordinates to the target waveform parameter space, it would be straightforward to place a uniform lattice and apply the template nudging algorithm to ensure the template bank reaches the required maximal mismatch threshold. Alternatively a generically precessing binary-neutron-star template bank could be constructed in a similar fashion with the added help of a known analytic expression for the metric.

For either targeted space, these template banks would have to be tested in a search pipeline like PyCBC. By injecting simulated compact binary coalescence signals into the detector data stream, the false alarm rates of these precessing template banks can be quantified. Assuming that these template banks recover these simulated injected signals sufficiently with adequate signal to noise ratios and low false alarm rates, that would mean it would be possible to search for real precessing compact binary coalescence systems in a meaningful way. These banks would likely contain tens of millions of templates or more, and a compact binary coalescence search of this scale has never been attempted. The work presented in this thesis added new tools building high dimensional compact binary coalescence template banks and improved upon the previously implemented stochastic and hybrid bank construction methods used to construct LIGO-Virgo compact binary coalescence template banks.

# CHAPTER 7

NATHANIEL MICHAEL INDIK

## 7.1 Personal Data

PLACE AND DATE OF BIRTH: Tucson, AZ, USA — June 30<sup>th</sup> 1990  
ADDRESS: Callinstr. 38 30167, Hannover, DE  
EMAIL: [nathaniel.indik@aei.mpg.de](mailto:nathaniel.indik@aei.mpg.de)

## 7.2 Education

<i>Current</i>	Leibniz Universität Hannover, DE <i>Graduate Student in Physics</i>
SEP 2013	<i>Courses taken:</i> Introductory German (2014 Winter Semester), IMPRS Lecture Weeks
FALL 2010	CAMBRIDGE UNIVERSITY Cambridge, UK <i>Undergraduate study abroad</i> <i>Courses taken:</i> Math Tripos III General Relativity, Math Tripos III Quantum Field Theory, Natural Science Tripos III Condensed Matter Field Theory, Natural Science Tripos III Particle Physics.
JUN 2012	THE CALIFORNIA INSTITUTE OF TECHNOLOGY 1200 E. California Blvd. Pasadena, CA, USA <i>Bachelors of Science (Cum Laude)</i>
OCT 2008	<i>Courses taken:</i> Quantum Field Theory, Complex Analysis, Partial Differential Equations, Group Theory, Scientific Communication and Presentation, Thermodynamics Statistical Mechanics, Quantum Mechanics, Lagrangian Mechanics, Electricity & Magnetism, Fluid Mechanics, Condensed Matter.
SUMMER 2008	GREEN FIELDS COUNTRY DAY SCHOOL COLLEGE PREPARATORY 6000 N. Camino De La Tierra, Tucson, AZ, USA
FALL 1999	<i>High School and Junior High School Education</i>

## 7.3 Awards

- [Special Breakthrough Prize in Physics for Detection of Gravitational Waves](#) (May 2016)
- [Gruber Cosmology Prize](#) (May 2016)
- [Princess of Asturias Award for Scientific Research](#) (June 2017)

## 7.4 Technologies

Python(Preferred), C(Native), C++, Condor, GIT, Java, Linux, Matlab, MPI, PERL, R

## 7.5 Professional Experience

<i>Current</i>	Max Planck Instistüt für Gravitationsphysik (Albert Einstein Instistüt-Hannover)
SEP 2013	<i>Graduate Student Researcher</i> Member of the LIGO-Virgo collaboration serving as a Compact Binary Coalescence [CBC] data analysis group supervised by Research Group Leader Dr. rer. nat. Badri Krishnan and Director Prof. Dr. rer. nat. Bruce Allen specializing in gravitational waveform template bank construction.
JUN 2013	THE CALIFORNIA INSITUTE OF TECHNOLOGY 1200 E. California Blvd. Pasadena, CA, USA
OCT 2012	<i>Visiting Student Researcher</i> Follow up to undergraduate thesis research conducted with Senior Research Scientist Dr. rer. nat. Lee Lindblom Our primary goal was to improve the global convergence of our method for solving the inverse stellar structure problem.
SUMMER 2012	Summer Trading Intern at GRAY WHALE CAPITAL LLC 10 East Yanonali Street Santa Suite 2A Barbara, CA, <i>Trading Intern</i> Developed several programs for a high frequency trading firm used to price several commodities traded on the NYSE. Designed software for use in compliance checks and the firm's daily trading.

## 7.6 Presentations

- CBC R&D Telecon Presentation Compact Binary Coalescence Template Nudging, G1702448, 12/2017
- PYCBC Telecon Presentation Reducing the number of CBC templates, G1701560, 09/2017
- LVC Poster Optimal Template Placement, G1700330, Pasadena, CA,USA 03/2017
- LVC Poster Prospects for searches for precessing compact binary systems, P1600330,Glasgow, UK 08/2016
- GWPAAW Poster Precessing stochastic template bank for neutron star - black hole systems, G1601810, Osaka, Japan 06/2015
- LVC Poster Building a Stochastic Precessing Template Bank for use in CBC NSBH Searches, G1500245, Pasadena, CA 03/2015

## 7.7 Publication List (excluding LVC papers)

- [Reducing the number of templates for aligned-spin compact binary coalescence gravitational wave searches using metric-agnostic template nudging](#) , **N. Indik**, H. Fehmann, F. Harke, A. B. Nielsen, & B. Krishnan, arXiv:1712.07869 (2017)
- [Stochastic template bank for gravitational wave searches for precessing neutron-star–black-hole coalescence events](#), **N. Indik**, K Haris, T. Dal Canton, H. Fehrmann, B. Krishnan, A. Lundgren, A. B. Nielsen, & A. Pai, Physical Review D, 95 064056 (2017)
- [Spectral Approach to the Relativistic Inverse Stellar Structure Problem II](#), L. Lindblom & **N. M. Indik**, Physical Review D, 89 064003 (2014).
- [Spectral Approach to the Relativistic Inverse Stellar Structure Problem](#) , L. Lindblom & **N. M. Indik**, Physical Review D, 86 084003 (2012).



## CHAPTER 8

## ACKNOWLEDGMENTS

**I would like to thank:** My Family, Master Oogway, Badri Krishnan, Lee Lindblom, Alex B. Nielsen, Bruce Allen, Henning, Oksana, Gabi, David Dale, Ernie Mercado, ATLAS, Aleksandra, Miriam, Evan, Pablo, Reinhard, Andy, Tito, Sebastian, Colin, Heather, Christoph, Julian, Lars, Andrey, Jing, Gregg, Grant, Sylvia, Sinéad, Divya, Avi, Map, Francesco, Gérman, Karo, Giulio, Wolfgang, Archana, Haris, Michéle, Chris Messenger, Frank, Collin, Kate, Alex, Tom, HB, Ofek, Rahul, Arunava, Yuanhao, Iuri, Yoshinta, Carsten, Alexander, Karsten, Fumiko, Vaishali, Brigitte, Andi, Sarah, Phillipp, Thomas, Benjamin, Janis, Bernd, Oliver, Felix, Kahae, Claus, Adam, Weihao, LVC, DJT, Tim, Mike, Troy, Dane, Auriel, Kaj, Jason, César, Becca, Julie, GFCDS, Misha Stepanov, Shrinivas Manne, Haskett, Schaffer, Jorge, Mitchell Dorson, Derek Goto, Priyam, Yoon, AJ, Jason, Kolodrubetz, Chi, Gong, Chris, Giulio, Diego, Ruddock, Wyatt, Tedward, Eric, Peyton, Diamond Jim, Kingfisher, Coca Cola, Taco Bell, In-N-Out, Locorito, The KOK, The KFC Double Down, The RZA, The GZA, Ol' Dirty Bastard, Inspectah Deck, Raekwon The Chef, U-God, Ghostface Killah & The M.E.T.H.O.D. man [275].





## BIBLIOGRAPHY

- [1] Founding of the gravity research foundation. <https://www.gravityresearchfoundation.org/new-page/>. Accessed: Jan 23 2018.
- [2] Gauss's great triangle and the shape of space. <https://thatsmaths.com/2014/07/10/gauss-great-triangle-and-the-shape-of-space/>.
- [3] H1L1-ER8\_HARM\_MEAN\_PSD-1126033217-223200. [https://github.com/ligo-cbc/pycbc-config/blob/master/01/psd/H1L1-ER8\\_HARM\\_MEAN\\_PSD-1126033217-223200.txt.gz](https://github.com/ligo-cbc/pycbc-config/blob/master/01/psd/H1L1-ER8_HARM_MEAN_PSD-1126033217-223200.txt.gz).
- [4] McGill sgr/axp online catalog. <http://www.physics.mcgill.ca/~pulsar/magnetar/main.html>. Accessed: 2018-01-19.
- [5] The LIGO algorithms library. <https://www.lsc-group.phys.uwm.edu/daswg/projects/lalsuite.html>.
- [6] Bakerian lecture: Nuclear constitution of atoms. *Proceedings of the Royal Society of London A: Mathematical, Physical and Engineering Sciences*, 97(686):374–400, 1920.
- [7] On the theory of quantum mechanics. *Proceedings of the Royal Society of London A: Mathematical, Physical and Engineering Sciences*, 112(762):661–677, 1926.
- [8] Complete list of L D Landau's works. *Phys. Usp.*, 41(6):621–623, 1998.
- [9] Atlas. [http://www.aei.mpg.de/24838/02\\_Computing\\_and\\_ATLAS](http://www.aei.mpg.de/24838/02_Computing_and_ATLAS), 2008. Accessed: 2018-01-20.
- [10] ATNF Pulsar Catalogue. <http://www.atnf.csiro.au/research/pulsar/psrcat/>, 2017. Accessed: 2017-10-23.
- [11] J. Aasi et al. Prospects for Observing and Localizing Gravitational-Wave Transients with Advanced LIGO and Advanced Virgo. 2013. [Living Rev. Rel.19,1(2016)].
- [12] J Aasi et al. Advanced ligo. *Classical and Quantum Gravity*, 32(7):074001, 2015.
- [13] B. Abbott et al. Detector description and performance for the first coincidence observations between LIGO and GEO. *Nucl. Instrum. Meth.*, A517:154–179, 2004.
- [14] B. P. Abbott et al. Binary Black Hole Mergers in the first Advanced LIGO Observing Run. *Phys. Rev.*, X6(4):041015, 2016.

- [15] B. P. Abbott et al. GW150914: First results from the search for binary black hole coalescence with Advanced LIGO. *Phys. Rev.*, D93(12):122003, 2016.
- [16] B. P. Abbott et al. GW150914: The Advanced LIGO Detectors in the Era of First Discoveries. *Phys. Rev. Lett.*, 116(13):131103, 2016.
- [17] B. P. Abbott et al. GW151226: Observation of Gravitational Waves from a 22-Solar-Mass Binary Black Hole Coalescence. *Phys. Rev. Lett.*, 116(24):241103, 2016.
- [18] B. P. Abbott et al. Observation of Gravitational Waves from a Binary Black Hole Merger. *Phys. Rev. Lett.*, 116(6):061102, 2016.
- [19] B. P. Abbott et al. Observing gravitational-wave transient GW150914 with minimal assumptions. *Phys. Rev.*, D93(12):122004, 2016. [Addendum: *Phys. Rev.* D94,no.6,069903(2016)].
- [20] B. P. Abbott et al. Properties of the Binary Black Hole Merger GW150914. *Phys. Rev. Lett.*, 116(24):241102, 2016.
- [21] B. P. Abbott et al. Gravitational Waves and Gamma-rays from a Binary Neutron Star Merger: GW170817 and GRB 170817A. *Astrophys. J.*, 848(2):L13, 2017.
- [22] B. P. Abbott et al. GW170104: Observation of a 50-Solar-Mass Binary Black Hole Coalescence at Redshift 0.2. *Phys. Rev. Lett.*, 118(22):221101, 2017.
- [23] B. P. Abbott et al. GW170608: Observation of a 19-solar-mass Binary Black Hole Coalescence. 2017.
- [24] B. P. Abbott et al. GW170814: A Three-Detector Observation of Gravitational Waves from a Binary Black Hole Coalescence. *Phys. Rev. Lett.*, 119(14):141101, 2017.
- [25] B. P. Abbott et al. GW170817: Observation of Gravitational Waves from a Binary Neutron Star Inspiral. *Phys. Rev. Lett.*, 119(16):161101, 2017.
- [26] B. P. Abbott et al. Multi-messenger Observations of a Binary Neutron Star Merger. *Astrophys. J.*, 848(2):L12, 2017.
- [27] Benjamin P. Abbott et al. The basic physics of the binary black hole merger GW150914. *Annalen Phys.*, 529(1-2):1600209, 2017.
- [28] Thomas D. Abbott et al. Improved analysis of GW150914 using a fully spin-precessing waveform Model. *Phys. Rev.*, X6(4):041014, 2016.
- [29] F Acernese et al. Advanced virgo: a second-generation interferometric gravitational wave detector. *Classical and Quantum Gravity*, 32(2):024001, 2015.
- [30] T. Adams, D. Buskulic, V. Germain, G. M. Guidi, F. Marion, M. Montani, B. Mours, F. Piergiovanni, and G. Wang. Low-latency analysis pipeline for compact binary coalescences in the advanced gravitational wave detector era. *Class. Quant. Grav.*, 33(17):175012, 2016.
- [31] Walter S. Adams. The Spectrum of the Companion of Sirius. *Publ. Astron. Soc. Pac.*, 27:236–237, 1915.
- [32] P. Ajith et al. Inspiral-merger-ringdown waveforms for black-hole binaries with non-precessing spins. *Phys. Rev. Lett.*, 106:241101, 2011.

- [33] P. Ajith, N. Fotopoulos, S. Privitera, A. Neunzert, and A. J. Weinstein. Effectual template bank for the detection of gravitational waves from inspiralling compact binaries with generic spins. *Phys. Rev.*, D89(8):084041, 2014.
- [34] Bruce Allen, Warren G. Anderson, Patrick R. Brady, Duncan A. Brown, and Jolien D. E. Creighton. FINDCHIRP: An Algorithm for detection of gravitational waves from inspiraling compact binaries. *Phys. Rev.*, D85:122006, 2012.
- [35] Justin Alsing, Hector O. Silva, and Emanuele Berti. Evidence for a maximum mass cut-off in the neutron star mass distribution and constraints on the equation of state. 2017.
- [36] Wilhelm Anderson. Über die grendichte der materie und der energie. *Zeitschrift für Physik*, 56(11):851–856, Nov 1929.
- [37] Fabio Antonini, Sourav Chatterjee, Carl L. Rodriguez, Meagan Morscher, Bharath Pat-tabiraman, Vicky Kalogera, and Frederic A. Rasio. Black hole mergers and blue stragglers from hierarchical triples formed in globular clusters. *Astrophys. J.*, 816(2):65, 2016.
- [38] Theocharis A. Apostolatos, Curt Cutler, Gerald J. Sussman, and Kip S. Thorne. Spin induced orbital precession and its modulation of the gravitational wave forms from merging binaries. *Phys. Rev.*, D49:6274–6297, 1994.
- [39] Aristotle and W. D. Ross. *Aristotelis Analytica priora et posteriora*. Scriptorum classicorum bibliotheca Oxoniensis. Oxonii, 1964.
- [40] K. G. Arun, Alessandra Buonanno, Guillaume Faye, and Evan Ochsner. Higher-order spin effects in the amplitude and phase of gravitational waveforms emitted by inspiraling compact binaries: Ready-to-use gravitational waveforms. *Phys. Rev.*, D79:104023, 2009. [Erratum: *Phys. Rev.*D84,049901(2011)].
- [41] W. Baade and F. Zwicky. On super-novae. *Proceedings of the National Academy of Science*, 20:254–259, May 1934.
- [42] W. Baade and F. Zwicky. Remarks on super-novae and cosmic rays. *Phys. Rev.*, 46:76–77, Jul 1934.
- [43] S. Babak, R. Balasubramanian, D. Churches, T. Cokelaer, and B. S. Sathyaprakash. A Template bank to search for gravitational waves from inspiralling compact binaries. I. Physical models. *Class. Quant. Grav.*, 23:5477–5504, 2006.
- [44] S. Babak et al. Searching for gravitational waves from binary coalescence. *Phys. Rev.*, D87(2):024033, 2013.
- [45] Stanislav Babak. Building a stochastic template bank for detecting massive black hole binaries. *Class. Quant. Grav.*, 25:195011, 2008.
- [46] R. Balasubramanian. Data analysis of gravitational wave signals. In *Proceedings, 18th Conference of the Indian Association for General Relativity and Gravitation: Madras, India, February 15-17, 1996*, pages 43–56, 1996.
- [47] M.V. Barkov, G.S. Bisnovatyi-Kogan, and S.A. Lamzin. The thermal evolution of thorne-zytkow objects. *Astronomy Reports*, 45:230–235, Mar 2001.
- [48] Krzysztof Belczynski, Daniel E. Holz, Tomasz Bulik, and Richard O’Shaughnessy. The first gravitational-wave source from the isolated evolution of two 40-100 Msun stars. *Nature*, 534:512, 2016.

- [49] Peter G. Bergmann. *Summary of the Chapel Hill Conference*, volume 29. 07 1957.
- [50] Emanuele Berti and Vitor Cardoso. Quasinormal ringing of Kerr black holes. I. The Excitation factors. *Phys. Rev.*, D74:104020, 2006.
- [51] Luc Blanchet. Gravitational Radiation from Post-Newtonian Sources and Inspiralling Compact Binaries. *Living Rev. Rel.*, 17:2, 2014.
- [52] Luc Blanchet, Alessandra Buonanno, and Guillaume Faye. Higher-order spin effects in the dynamics of compact binaries. II. Radiation field. *Phys. Rev.*, D74:104034, 2006. [Erratum: *Phys. Rev.*D81,089901(2010)].
- [53] Luc Blanchet, Thibault Damour, Gilles Esposito-Farese, and Bala R. Iyer. Gravitational radiation from inspiralling compact binaries completed at the third post-Newtonian order. *Phys. Rev. Lett.*, 93:091101, 2004.
- [54] Luc Blanchet, Thibault Damour, and Bala R. Iyer. Gravitational waves from inspiralling compact binaries: Energy loss and wave form to second postNewtonian order. *Phys. Rev.*, D51:5360, 1995. [Erratum: *Phys. Rev.*D54,1860(1996)].
- [55] Luc Blanchet, Thibault Damour, Bala R. Iyer, Clifford M. Will, and Alan.G. Wiseman. Gravitational radiation damping of compact binary systems to second postNewtonian order. *Phys. Rev. Lett.*, 74:3515–3518, 1995.
- [56] A. Boehle, A. M. Ghez, R. Schödel, L. Meyer, S. Yelda, S. Albers, G. D. Martinez, E. E. Becklin, T. Do, J. R. Lu, K. Matthews, M. R. Morris, B. Sitarski, and G. Witzel. An improved distance and mass estimate for Sgr A\* from a multistar orbit analysis. *The Astrophysical Journal*, 830(1):17, 2016.
- [57] Alejandro Bohé et al. Improved effective-one-body model of spinning, nonprecessing binary black holes for the era of gravitational-wave astrophysics with advanced detectors. *Phys. Rev.*, D95(4):044028, 2017.
- [58] Alejandro Bohé, Sylvain Marsat, and Luc Blanchet. Next-to-next-to-leading order spin-orbit effects in the gravitational wave flux and orbital phasing of compact binaries. *Class. Quant. Grav.*, 30:135009, 2013.
- [59] Howard E. Bond, Gail H. Schaefer, Ronald L. Gilliland, Jay B. Holberg, Brian D. Mason, Irving W. Lindenblad, Miranda Seitz-McLeese, W. David Arnett, Pierre Demarque, Federico Spada, Patrick A. Young, Martin A. Barstow, Matthew R. Burleigh, and Donald Gudehus. The sirius system and its astrophysical puzzles: Hubble space telescope and ground-based astrometry. *The Astrophysical Journal*, 840(2):70, 2017.
- [60] Vladimir B Braginskii. Gravitational radiation and the prospect of its experimental discovery. *Soviet Physics Uspekhi*, 8(4):513, 1966.
- [61] H. W. Brinkmann. Einstein spaces which are mapped conformally on each other. *Mathematische Annalen*, 94(1):119–145, Dec 1925.
- [62] Duncan A. Brown, Ian Harry, Andrew Lundgren, and Alexander H. Nitz. Detecting binary neutron star systems with spin in advanced gravitational-wave detectors. *Phys. Rev.*, D86:084017, 2012.
- [63] Duncan A. Brown, Andrew Lundgren, and R. O’Shaughnessy. Nonspinning searches for spinning binaries in ground-based detector data: Amplitude and mismatch predictions in the constant precession cone approximation. *Phys. Rev.*, D86:064020, 2012.

- [64] Alessandra Buonanno, Bala Iyer, Evan Ochsner, Yi Pan, and B. S. Sathyaprakash. Comparison of post-Newtonian templates for compact binary inspiral signals in gravitational-wave detectors. *Phys. Rev.*, D80:084043, 2009.
- [65] Juan Calderón Bustillo, Alejandro Bohé, Sascha Husa, Alicia M. Sintes, Mark Hannam, and Michael Pürrer. Comparison of subdominant gravitational wave harmonics between post-Newtonian and numerical relativity calculations and construction of multi-mode hybrids. 2015.
- [66] Juan Calderón Bustillo, Sascha Husa, Alicia M. Sintes, and Michael Pürrer. Impact of gravitational radiation higher order modes on single aligned-spin gravitational wave searches for binary black holes. *Phys. Rev.*, D93(8):084019, 2016.
- [67] Juan Calderón Bustillo, Pablo Laguna, and Deirdre Shoemaker. Detectability of gravitational waves from binary black holes: Impact of precession and higher modes. *Phys. Rev.*, D95(10):104038, 2017.
- [68] M. Campanelli, C. O. Lousto, P. Marronetti, and Y. Zlochower. Accurate evolutions of orbiting black-hole binaries without excision. *Phys. Rev. Lett.*, 96:111101, Mar 2006.
- [69] Kipp Cannon et al. Toward Early-Warning Detection of Gravitational Waves from Compact Binary Coalescence. *Astrophys. J.*, 748:136, 2012.
- [70] Collin Capano, Ian Harry, Stephen Privitera, and Alessandra Buonanno. Implementing a search for gravitational waves from binary black holes with nonprecessing spin. *Phys. Rev.*, D93(12):124007, 2016.
- [71] Christian Y. Cardall, Madappa Prakash, and James M. Lattimer. Effects of strong magnetic fields on neutron star structure. *Astrophys. J.*, 554:322–339, 2001.
- [72] B. Caron et al. The Virgo interferometer. *Class. Quant. Grav.*, 14:1461–1469, 1997.
- [73] Jorge L. Cervantes-Cota, S. Galindo-Uribarri, and G-F. Smoot. A Brief History of Gravitational Waves. *Universe*, 2(3):22, 2016.
- [74] J. Chadwick. Possible Existence of a Neutron. *Nature*, 129:312, 1932.
- [75] J. Chadwick. The Existence of a Neutron. *Proc. Roy. Soc. Lond.*, A136(830):692–708, 1932.
- [76] CHANDRA. Vela Pulsar Jet: New Chandra Movie Features Neutron Star Action. <http://chandra.harvard.edu/photo/2013/vela/>, 2010.
- [77] S. Chandrasekhar. The highly collapsed configurations of a stellar mass (Second paper). *Mon. Not. Roy. Astron. Soc.*, 95:207–225, 1935.
- [78] Subrahmanyan Chandrasekhar. The maximum mass of ideal white dwarfs. *Astrophys. J.*, 74:81–82, 1931.
- [79] Subrahmanyan Chandrasekhar. Xlviii. the density of white dwarf stars. *The London, Edinburgh, and Dublin Philosophical Magazine and Journal of Science*, 11(70):592–596, 1931.
- [80] S Chatterji, L Blackburn, G Martin, and E Katsavounidis. Multiresolution techniques for the detection of gravitational-wave bursts. *Classical and Quantum Gravity*, 21(20):S1809, 2004.

- [81] J.P.A. Clark and D.M. Eardley. Evolution of close neutron star binaries. *Astrophys. J.*, 215:311–322, Jul 1977.
- [82] J.P.A. Clark, E.P.J. van den Heuvel, and W. Sutantyo. Formation of neutron star binaries and their importance for gravitational radiation. *Astronomy and Astrophysics*, 72:120–128, Feb 1979.
- [83] W. K. Clifford. *On the Space-Theory of Matter*, pages 295–296. Springer Netherlands, Dordrecht, 1976.
- [84] Thomas Cokelaer. Gravitational waves from inspiralling compact binaries: Hexagonal template placement and its efficiency in detecting physical signals. *Phys. Rev.*, D76:102004, 2007.
- [85] Neil J Cornish and Tyson B Littenberg. Bayeswave: Bayesian inference for gravitational wave bursts and instrument glitches. *Classical and Quantum Gravity*, 32(13):135012, 2015.
- [86] D. A. Coulter, R. J. Foley, C. D. Kilpatrick, M. R. Drout, A. L. Piro, B. J. Shappee, M. R. Siebert, J. D. Simon, N. Ulloa, D. Kasen, B. F. Madore, A. Murguia-Berthier, Y.-C. Pan, J. X. Prochaska, E. Ramirez-Ruiz, A. Rest, and C. Rojas-Bravo. Swope supernova survey 2017a (sss17a), the optical counterpart to a gravitational wave source. *Science*, 358(6370):1556–1558, 2017.
- [87] Curt Cutler and Eanna E. Flanagan. Gravitational waves from merging compact binaries: How accurately can one extract the binary’s parameters from the inspiral wave form? *Phys. Rev.*, D49:2658–2697, 1994.
- [88] Tito Dal Canton et al. Implementing a search for aligned-spin neutron star-black hole systems with advanced ground based gravitational wave detectors. *Phys. Rev.*, D90(8):082004, 2014.
- [89] Tito Dal Canton and Ian W. Harry. Designing a template bank to observe compact binary coalescences in Advanced LIGO’s second observing run. *eprint arXiv 1705.01845*, 2017.
- [90] Tito Dal Canton, Andrew P. Lundgren, and Alex B. Nielsen. Impact of precession on aligned-spin searches for neutron-star–black-hole binaries. *Phys. Rev.*, D91(6):062010, 2015.
- [91] Thibault Damour, Bala R. Iyer, and B. S. Sathyaprakash. Improved filters for gravitational waves from inspiralling compact binaries. *Phys. Rev.*, D57:885–907, 1998.
- [92] Thibault Damour, Bala R. Iyer, and B. S. Sathyaprakash. A Comparison of search templates for gravitational waves from binary inspiral. *Phys. Rev.*, D63:044023, 2001. [Erratum: *Phys. Rev.*D72,029902(2005)].
- [93] Thibault Damour, Bala R. Iyer, and B. S. Sathyaprakash. A Comparison of search templates for gravitational waves from binary inspiral - 3.5PN update. *Phys. Rev.*, D66:027502, 2002.
- [94] S. E. de Mink and K. Belczynski. Merger rates of double neutron stars and stellar origin black holes: The Impact of Initial Conditions on Binary Evolution Predictions. *Astrophys. J.*, 814(1):58, 2015.

- [95] S. E. de Mink, M. Cantiello, N. Langer, O. R. Pols, I. Brott, and S. Ch. Yoon. Rotational mixing in massive binaries: detached short-period systems. *Astron. Astrophys.*, 497:243, 2009.
- [96] S. E. de Mink, M. Cantiello, N. Langer, S. Ch. Yoon, I. Brott, E. Glebbeek, M. Verkoulen, and O. R. Pols. Rotational mixing in close binaries. *IAU Symp.*, 252:365–370, 2008.
- [97] S. V. Dhurandhar and B. S. Sathyaprakash. Choice of filters for the detection of gravitational waves from coalescing binaries. 2. Detection in colored noise. *Phys. Rev.*, D49:1707–1722, 1994.
- [98] T. Do, G. D. Martinez, S. Yelda, A. M. Ghez, J. Bullock, M. Kaplinghat, J. R. Lu, A. H. G. Peter, and K. Phifer. 3D stellar kinematics at the Galactic center: measuring the nuclear star cluster spatial density profile, black hole mass, and distance. *Astrophys. J.*, 779:L6, 2013.
- [99] Martin Durant, Oleg Kargaltsev, George G. Pavlov, Julia Kropotina, and Kseniya Levenfish. The helical jet of the Vela Pulsar. *Astrophys. J.*, 763:72, 2013.
- [100] H. Dussan and C. Horowitz. Fusion reactions of neutron rich nuclei in dense matter. In *APS April Meeting Abstracts*, Apr 2008.
- [101] Arthur Stanley Eddington. The propagation of gravitational waves. *Proc. Roy. Soc. Lond.*, A102:268–282, 1922.
- [102] A.S. Eddington. *The Internal Constitution of the Stars*. The University Press, 1926.
- [103] The Editors of Encyclopedia Britannica. Karl Schwarzschild. <https://www.britannica.com/biography/Karl-Schwarzschild>, Jan 2017. Accessed Jan 27 2018.
- [104] P. P. Eggleton. Approximations to the radii of Roche lobes. *Astrophys. J.*, 268:368, 1983.
- [105] A. Einstein. *The Collected Papers of Albert Einstein, Volume 8: The Berlin Years: Correspondence, 1914-1918*, volume 8.
- [106] A. Einstein. Näherungsweise integration der feldgleichungen der gravitation. *Sitzungsberichte der Königlich Preußischen Akademie der Wissenschaften (Berlin)*, Seite 688–696., 1916.
- [107] A. Einstein. Näherungsweise integration der feldgleichungen der gravitation. *Sitzungsberichte der Königlich Preussischen Akademie der Wissenschaften Berlin*, pages 688–696, 1916.
- [108] A. Einstein. Über gravitationswellen. *Sitzungsberichte der Königlich Preussischen Akademie der Wissenschaften Berlin*, pages 154–167, 1918.
- [109] A. Einstein, L. Infeld, and B. Hoffmann. The Gravitational Equations and the Problem of Motion. *Annals of Mathematics*, 39:65–100, Jan 1938.
- [110] A. Einstein and N. Rosen. On gravitational waves. *Journal of The Franklin Institute*, 223:43–54, Jan 1937.
- [111] Albert Einstein. Über das Relativitätsprinzip und die aus demselben gezogenen Folgerungen. *“Jahrbuch der Radioaktivität und Elektronik”*, 4, 1908.

- [112] Albert Einstein. Über den Einfluß der Schwerkraft auf die Ausbreitung des Lichtes. *Annalen der Physik*, 340:898–908, 1911.
- [113] Albert Einstein. Explanation of the Perihelion Motion of Mercury from the General Theory of Relativity. *Sitzungsber. Preuss. Akad. Wiss. Berlin (Math. Phys.)*, 1915:831–839, 1915.
- [114] Albert Einstein. On the General Theory of Relativity. *Sitzungsber. Preuss. Akad. Wiss. Berlin (Math. Phys.)*, 1915:778–786, 1915. [Addendum: *Sitzungsber. Preuss. Akad. Wiss. Berlin (Math. Phys.)*1915,799(1915)].
- [115] Albert Einstein. The Field Equations of Gravitation. *Sitzungsber. Preuss. Akad. Wiss. Berlin (Math. Phys.)*, 1915:844–847, 1915.
- [116] Ergma, E. and van den Heuvel. On the initial progenitor masses of stellar mass black holes and neutron stars. *aap*, 331:L29–L32, mar 1998.
- [117] Ann Ewing. “Black Holes” in Space. *Science News Letter*, 85(3), Jan 18 1964.
- [118] Y.A. Fadeyev and M.F. Novikova. Radial Pulsations of Helium Stars with Masses from 1 to 10 M. *Astronomy Letters*, 29:522–529, Aug 2003.
- [119] Y.A. Fadeyev and M.F. Novikova. Radial Pulsations of Helium Stars with Masses from 10 to 50M. *Astronomy Letters*, 30:707–714, Oct 2004.
- [120] Henning Fehrmann and Holger J. Pletsch. Efficient generation and optimization of stochastic template banks by a neighboring cell algorithm. *Phys. Rev.*, D90(12):124049, 2014.
- [121] Enrico Fermi and A. Zannoni. On the Quantization of the Monoatomic Ideal Gas (English translation). *eprint arXiv:cond-mat/9912229*, Dec 1999.
- [122] Lee S. Finn. Detection, measurement and gravitational radiation. *Phys. Rev.*, D46:5236–5249, 1992.
- [123] R. L. Forward. Wideband laser-interferometer gravitational-radiation experiment. *Physical Review D*, 17:379–390, Jan 1978.
- [124] Fotopoulos, Nickolas and Privitera, Stephen. Sbank. [http://software.ligo.org/docs/lalsuite/lalapps/lalapps\\_\\_cbc\\_\\_sbank\\_8py\\_source.html](http://software.ligo.org/docs/lalsuite/lalapps/lalapps__cbc__sbank_8py_source.html), 2017.
- [125] R.H Fowler. On dense matter. *Monthly Notices of the Royal Astronomical Society*, 87:114–122, Dec 1926.
- [126] M. E. Gertsenshtein and V. I. Pustovoit. On the Detection of Low Frequency Gravitational Waves. *Sov. Phys. JETP*, 16:433, 1962.
- [127] A. Ghez et al. The Galactic Center: A Laboratory for Fundamental Astrophysics and Galactic Nuclei. 2009.
- [128] A. M. Ghez, G. Duchêne, K. Matthews, S. D. Hornstein, A. Tanner, J. Larkin, M. Morris, E. E. Becklin, S. Salim, T. Kremenek, D. Thompson, B. T. Soifer, G. Neugebauer, and I. McLean. The first measurement of spectral lines in a short-period star bound to the galaxy’s central black hole: A paradox of youth. *The Astrophysical Journal Letters*, 586(2):L127, 2003.



- [129] A. M. Ghez, S. Salim, Seth D. Hornstein, A. Tanner, M. Morris, E. E. Becklin, and G. Duchêne. Stellar orbits around the galactic center black hole. *Astrophys. J.*, 620:744–757, 2005.
- [130] P. Gil-Pons and E. Garcia-Berro. On the formation of oxygen-neon white dwarfs in close binary systems. *Astron. Astrophys.*, 375:87, 2001.
- [131] Norman K. Glendenning. Limiting rotational period of neutron stars. *Phys. Rev.*, D46:4161–4168, 1992.
- [132] T. Gold. Rotating neutron stars as the origin of the pulsating radio sources. *Nature*, 218:731–732, 1968.
- [133] A. Gullstrand. *Allgemeine Lösung des statischen Einkörperproblems in der Einsteinschen Gravitationstheorie*. Stockholm [u.a.] Almqvist & Wiksell [u.a.], 1922.
- [134] M. Habibi, S. Gillessen, F. Martins, F. Eisenhauer, P. M. Plewa, O. Pfuhl, E. George, J. Dexter, I. Waisberg, T. Ott, S. von Fellenberg, M. Bauböck, A. Jimenez-Rosales, and R. Genzel. Twelve years of spectroscopic monitoring in the galactic center: The closest look at s-stars near the black hole. *The Astrophysical Journal*, 847(2):120, 2017.
- [135] Mark Hannam, Patricia Schmidt, Alejandro Bohé, Leela Haegel, Sascha Husa, Frank Ohme, Geraint Pratten, and Michael Pürrer. Simple Model of Complete Precessing Black-Hole-Binary Gravitational Waveforms. *Phys. Rev. Lett.*, 113(15):151101, 2014.
- [136] Ian Harry, Stephen Privitera, Alejandro Bohé, and Alessandra Buonanno. Searching for Gravitational Waves from Compact Binaries with Precessing Spins. *Phys. Rev.*, D94(2):024012, 2016.
- [137] Ian W. Harry, Bruce Allen, and B. S. Sathyaprakash. A Stochastic template placement algorithm for gravitational wave data analysis. *Phys. Rev.*, D80:104014, 2009.
- [138] Ian W. Harry, Alexander H. Nitz, Duncan A. Brown, Andrew P. Lundgren, Evan Ochsner, and Drew Keppel. Investigating the effect of precession on searches for neutron-star-black-hole binaries with Advanced LIGO. *Phys. Rev.*, D89(2):024010, 2014.
- [139] O. Heaviside. *Electromagnetic Theory*. Number Bd. 1 in Electrician series. “The Electrician” Printing and Publishing Company, Limited, 1893.
- [140] Jason W. T. Hessels, Scott M. Ransom, Ingrid H. Stairs, Paulo Cesar Carvalho Freire, Victoria M. Kaspi, and Fernando Camilo. A radio pulsar spinning at 716-hz. *Science*, 311:1901–1904, 2006.
- [141] J. B. Holberg, M. A. Barstow, F. C. Bruhweiler, A. M. Cruise, and A. J. Penny. Sirius b: A new, more accurate view. *The Astrophysical Journal*, 497(2):935, 1998.
- [142] David A. Hubber and A. P. Whitworth. Binary star formation from ring fragmentation. *Astron. Astrophys.*, 437:113, 2005.
- [143] R. A. Hulse and J. H. Taylor. Discovery of a pulsar in a binary system. *Astrophys. J.*, 195:L51–L53, 1975.
- [144] Jarrod R. Hurley, Christopher A. Tout, and Onno R. Pols. Evolution of binary stars and the effect of tides on binary populations. *Mon. Not. Roy. Astron. Soc.*, 329:897, 2002.

- [145] Nathaniel Indik, Henning Fehrmann, Franz Harke, Badri Krishnan, and Alex B. Nielsen. Reducing the number of templates for aligned-spin compact binary coalescence gravitational wave searches. 2017.
- [146] Nathaniel Indik, K. Haris, Tito Dal Canton, Henning Fehrmann, Badri Krishnan, Andrew Lundgren, Alex B. Nielsen, and Archana Pai. Stochastic template bank for gravitational wave searches for precessing neutron-star–black-hole coalescence events. *Phys. Rev.*, D95(6):064056, 2017.
- [147] Piotr Jaranowski, Andrzej Krolak, and Bernard F. Schutz. Data analysis of gravitational - wave signals from spinning neutron stars. 1. The Signal and its detection. *Phys. Rev.*, D58:063001, 1998.
- [148] Xisco Jiménez-Forteza, David Keitel, Sascha Husa, Mark Hannam, Sebastian Khan, and Michael Pürrer. Hierarchical data-driven approach to fitting numerical relativity data for nonprecessing binary black holes with an application to final spin and radiated energy. *Phys. Rev.*, D95(6):064024, 2017.
- [149] S. Jones, R. Hirschi, K. Nomoto, T. Fischer, F. X. Timmes, F. Herwig, B. Paxton, H. Toki, T. Suzuki, G. Martínez-Pinedo, Y. H. Lam, and M. G. Bertolli. Advanced burning stages and fate of 8-10 m stars. *The Astrophysical Journal*, 772(2):150, 2013.
- [150] Vassiliki Kalogera, K. Belczynski, C. Kim, Richard W. O’Shaughnessy, and B. Willems. Formation of Double Compact Objects. *Phys. Rept.*, 442:75–108, 2007.
- [151] S. O. Kepler, S. J. Kleinman, A. Nitta, D. Koester, B. G. Castanheira, O. Giovannini, A. F. M. Costa, and L. Althaus. White Dwarf Mass Distribution in the SDSS. *Mon. Not. Roy. Astron. Soc.*, 375:1315–1324, 2007.
- [152] Drew Keppel, Andrew P. Lundgren, Benjamin J. Owen, and Hanyuan Zhu. Parameter space metric for 3.5 post-Newtonian gravitational-waves from compact binary inspirals. *Phys. Rev.*, D88:063002, 2013.
- [153] Roy P. Kerr. Gravitational field of a spinning mass as an example of algebraically special metrics. *Phys. Rev. Lett.*, 11:237–238, Sep 1963.
- [154] Roy P. Kerr. Gravitational field of a spinning mass as an example of algebraically special metrics. *Phys. Rev. Lett.*, 11:237–238, 1963.
- [155] Sebastian Khan, Sascha Husa, Mark Hannam, Frank Ohme, Michael Pürrer, Xisco Jiménez Forteza, and Alejandro Bohé. Frequency-domain gravitational waves from nonprecessing black-hole binaries. II. A phenomenological model for the advanced detector era. *Phys. Rev.*, D93(4):044007, 2016.
- [156] Lawrence E. Kidder. Coalescing binary systems of compact objects to postNewtonian 5/2 order. 5. Spin effects. *Phys. Rev.*, D52:821–847, 1995.
- [157] Mukremin Kilic, Carlos Allende Prieto, Warren R. Brown, and D. Koester. The Lowest Mass White Dwarf. *Astrophys. J.*, 660:1451–1461, 2007.
- [158] Pavel Kroupa, Monika Petr, and Mark McCaughrean. Binary stars in young clusters: models versus observations of the trapezium cluster. *New Astron.*, 4:495–520, 1999.
- [159] Matthias U. Kruckow, Thomas M. Tauris, Norbert Langer, Michael Kramer, and Robert G. Izzard. Progenitors of gravitational wave mergers: Binary evolution with the stellar grid based code ComBinE. 2018.

- [160] A. G. Kuranov and K. A. Postnov. Neutron stars in globular clusters: formation and observational manifestations. *Astron. Lett.*, 32:393, 2006.
- [161] Charles J. Lada. Stellar Multiplicity and the IMF: Most Stars Are Single. *Astrophys. J.*, 640:L63–L66, 2006.
- [162] L. D. Landau. On the theory of phase transitions. *Zh. Eksp. Teor. Fiz.*, 7:19–32, 1937. [Ukr. J. Phys.53,25(2008)].
- [163] J. M. Lattimer and M. Prakash. Neutron star structure and the equation of state. *Astrophys. J.*, 550:426, 2001.
- [164] James M. Lattimer, Madappa Prakash, Dieter Masak, and Amos Yahil. Rapidly rotating pulsars and the equation of state. *Astrophys. J.*, 355:241–254, 1990.
- [165] G. Lemaître. L’Univers en expansion. *Annales de la Société Scientifique de Bruxelles*, 53, 1933.
- [166] Emily M. Levesque, Philip Massey, Anna N. Zytzkow, and Nidia Morrell. Discovery of a thorne-zytkow object candidate in the small magellanic cloud. *Monthly Notices of the Royal Astronomical Society: Letters*, 443(1):L94–L98, 2014.
- [167] LIGO and Virgo and Farr, B. (University of Oregon). Comparison of gravitational-wave signal templates from recent LIGO/Virgo observations. <https://www.ligo.org/detections/GW170814.php>, 2017. Accessed: 2018-01-08.
- [168] LIGO Scientific Collaboration. <https://www.lsc-group.phys.uwm.edu/daswg/projects/lal.html>, 2017.
- [169] David Lindley. Focus: Landmarks–forgotten black hole birth. <https://physics.aps.org/story/v13/st23>, May 2004. Accessed Jan 27 2018.
- [170] Lionel London, Sebastian Khan, Edward Fauchon-Jones, Xisco Jiménez Forteza, Mark Hannam, Sascha Husa, Chinmay Kalaghatgi, Frank Ohme, and Francesco Pannarale. First higher-multipole model of gravitational waves from spinning and coalescing black-hole binaries. 2017.
- [171] D. R. Lorimer. Binary and Millisecond Pulsars. *Living Rev. Rel.*, 11:8, 2008.
- [172] Lorimer, D.R. and Kramer, M. *Handbook of Pulsar Astronomy*. Cambridge University Press, Oct 2012.
- [173] J. R. Lu, A. M. Ghez, Seth D. Hornstein, M. R. Morris, E. E. Becklin, and K. Matthews. A Disk of Young Stars at the Galactic Center as Determined by Individual Stellar Orbits. *Astrophys. J.*, 690:1463–1487, 2009.
- [174] A. Lundgren and R. O’Shaughnessy. Single-spin precessing gravitational waveform in closed form. *Phys. Rev.*, D89(4):044021, 2014.
- [175] M. Maggiore. *Gravitational Waves: Volume 1: Theory and Experiments*. Gravitational Waves. OUP Oxford, 2008.
- [176] Gian Mario Manca and Michele Vallisneri. Cover art: Issues in the metric-guided and metric-less placement of random and stochastic template banks. *Phys. Rev.*, D81:024004, 2010.

- [177] Pablo Marchant, Norbert Langer, Philipp Podsiadlowski, Thomas M. Tauris, and Takashi J. Moriya. A new route towards merging massive black holes. *Astron. Astrophys.*, 588:A50, 2016.
- [178] A. G. Masevitch, A. V. Tutukov, and L. R. Yungelson. Evolution of massive close binaries and formation of neutron stars and black holes. *Astrophysics and Space Science*, 40(1):115–133, Mar 1976.
- [179] C. Messenger, R. Prix, and M. A. Papa. Random template banks and relaxed lattice coverings. *Phys. Rev.*, D79:104017, 2009.
- [180] Cody Messick et al. Analysis Framework for the Prompt Discovery of Compact Binary Mergers in Gravitational-wave Data. *Phys. Rev.*, D95(4):042001, 2017.
- [181] L. Meyer, A. M. Ghez, R. Schodel, S. Yelda, A. Boehle, J. R. Lu, M. R. Morris, E. E. Becklin, and K. Matthews. Supplementary Materials for The Shortest Known Period Star Orbiting our Galaxy’s Supermassive Black Hole. <http://science.sciencemag.org/content/sci/suppl/2012/10/03/338.6103.84.DC1/Meyer.SM.pdf>, 2012.
- [182] L. Meyer, A. M. Ghez, R. Schodel, S. Yelda, A. Boehle, J. R. Lu, M. R. Morris, E. E. Becklin, and K. Matthews. The Shortest Known Period Star Orbiting our Galaxy’s Supermassive Black Hole. *Science*, 338:84–87, 2012.
- [183] Albert Abraham Michelson and Edward Williams Morley. On the Relative Motion of the Earth and the Luminiferous Ether. *Am. J. Sci.*, 34:333–345, 1887.
- [184] M. Coleman Miller and Vanessa M. Lauburg. Mergers of Stellar-Mass Black Holes in Nuclear Star Clusters. *Astrophys. J.*, 692:917–923, 2009.
- [185] C.W. Misner, K.S. Thorne, and J.A. Wheeler. *Gravitation*. Number 3 in Gravitation. W. H. Freeman, 1973.
- [186] S. Miyaji, K. Nomoto, K. Yokoi, and D. Sugimoto. Supernova triggered by electron captures. *Publications of the Astronomical Society of Japan*, 32:303, 1980.
- [187] Meagan Morscher, Bharath Pattabiraman, Carl Rodriguez, Frederic A. Rasio, and Stefan Umbreit. The Dynamical Evolution of Stellar Black Holes in Globular Clusters. *Astrophys. J.*, 800(1):9, 2015.
- [188] G. E. Moss, L. R. Miller, and R. L. Forward. Photon-noise-limited laser transducer for gravitational antenna. *Appl. Opt.*, 10:2495–2498, 1971.
- [189] Abdul H. Mroué, Mark A. Scheel, Béla Szilágyi, Harald P. Pfeiffer, Michael Boyle, Daniel A. Hemberger, Lawrence E. Kidder, Geoffrey Lovelace, Serguei Ossokine, Nicholas W. Taylor, Anıl Zenginoğlu, Luisa T. Buchman, Tony Chu, Evan Foley, Matthew Giesler, Robert Owen, and Saul A. Teukolsky. Catalog of 174 binary black hole simulations for gravitational wave astronomy. *Phys. Rev. Lett.*, 111:241104, Dec 2013.
- [190] NASA and ESA and Bond, H. (STScI) and Barslow, M. (University of Leicester). Hubble Space Telescope Sirius A and Sirius B (WFPC2) (STScI-PRC05-36a). [http://hubblesite.org/image/1820/news\\_release/2005-36](http://hubblesite.org/image/1820/news_release/2005-36), 2003.
- [191] J. A. Nelder and R. Mead. A Simplex Method for Function Minimization. *Comput. J.*, 7:308–313, 1965.

- [192] E.T. Newman, E. Couch, K. Chinnapared, A. Exton, A. Prakash, and R. Torrence. Metric of a Rotating, Charged Mass. *Journal of Mathematical Physics*, 6:918–919, jun 1965.
- [193] E.T. Newman and A.I. Janis. Note on the Kerr Spinning-Particle Metric. *Journal of Mathematical Physics*, 6:915–917, jun 1965.
- [194] I. Newton. *Philosophiæ naturalis principia mathematica*. Jussu Societatis Regiæ ac Typis Joseph Streater, 1687.
- [195] A. B. Nielsen. Private communication, 2018.
- [196] Alexander H. Nitz, Thomas Dent, Tito Dal Canton, Stephen Fairhurst, and Duncan A. Brown. Detecting binary compact-object mergers with gravitational waves: Understanding and Improving the sensitivity of the PyCBC search. *Astrophys. J.*, 849(2):118, 2017.
- [197] Nitz, A. and Harry, I. and Brown, D. and Biwer, C. and Willis, J. and Dal Canton, T. and Pekowsky, L. and Dent, T. and Williamson, A. and Capano, C. and others. Pycbc software. <https://doi.org/10.5281/zenodo.1058970>, 2017.
- [198] Gunnar Nordstrom. On a theory of electricity and gravitation. 1914.
- [199] T. Nugis and H.J.G.L.M. Lamers. Mass-loss rates of Wolf-Rayet stars as a function of stellar parameters. *Astronomy and Astrophysics*, 360:227–244, Aug 2000.
- [200] J. J. O’Connor and E. F. Robertson. Karl schwarzschild. <http://www-groups.dcs.st-and.ac.uk/~johistory/Biographies/Schwarzschild.html>.
- [201] Frank Ohme, Alex B. Nielsen, Drew Keppel, and Andrew Lundgren. Statistical and systematic errors for gravitational-wave inspiral signals: A principal component analysis. *Phys. Rev.*, D88(4):042002, 2013.
- [202] S.A. Olausen and V.M. Kaspi. The McGill Magnetar Catalog. *The Astrophysical Journal Supplement*, 212:6, May 2014.
- [203] J. R. Oppenheimer and Robert Serber. On the stability of stellar neutron cores. *Phys. Rev.*, 54:540–540, Oct 1938.
- [204] J. R. Oppenheimer and H. Snyder. On continued gravitational contraction. *Phys. Rev.*, 56:455–459, Sep 1939.
- [205] J. R. Oppenheimer and G. M. Volkoff. On Massive neutron cores. *Phys. Rev.*, 55:374–381, 1939.
- [206] Benjamin J. Owen. Search templates for gravitational waves from inspiraling binaries: Choice of template spacing. *Phys. Rev.*, D53:6749–6761, 1996.
- [207] Benjamin J. Owen and B. S. Sathyaprakash. Matched filtering of gravitational waves from inspiraling compact binaries: Computational cost and template placement. *Phys. Rev.*, D60:022002, 1999.
- [208] B P and van den Heuvel E P J Flannery. On the origin of the binary pulsar psr 1913+16. *Astronomy and astrophysics*, 39:61, 1975.
- [209] F. Pacini. The secular decrease of the optical and X-ray luminosity of pulsars. *Astrophys. J.*, 163:L17–L19, 1971.

- [210] P. Painlevé. La mécanique classique et la théorie de la relativité. *Comptes Rendus Academie des Sciences (serie non specifiée)*, 173:677–680, 1921.
- [211] W. Pauli. Über den Zusammenhang des Abschlusses der Elektronengruppen im Atom mit der Komplexstruktur der Spektren. *Zeitschrift für Physik*, 31(1):765–783, Feb 1925.
- [212] D. Percival and A. Walden. *Spectral Analysis for Physical Applications: Multitaper and Conventional Univariate Techniques*. Cambridge University Press, Cambridge, UK, 1993.
- [213] P.C. Peters and J. Mathews. Gravitational Radiation from Point Masses in a Keplerian Orbit. *Physical Review*, 131:435–440, Jul 1963.
- [214] F. A. E. Pirani. On the Physical significance of the Riemann tensor. *Acta Phys. Polon.*, 15:389–405, 1956. [Gen. Rel. Grav.41,1215(2009)].
- [215] F. A. E. Pirani. Invariant formulation of gravitational radiation theory. *Phys. Rev.*, 105:1089–1099, 1957.
- [216] H. J. Pletsch et al. Binary Millisecond Pulsar Discovery via Gamma-Ray Pulsations. *Science*, 338:1314, 2012.
- [217] M. H. Poincaré. Sur la dynamique de l'électron. *Rendiconti del Circolo Matematico di Palermo (1884-1940)*, 21(1):129–175, Dec 1906.
- [218] Eric Poisson and Clifford M. Will. Gravitational waves from inspiraling compact binaries: Parameter estimation using second postNewtonian wave forms. *Phys. Rev.*, D52:848–855, 1995.
- [219] Simon F. Portegies Zwart and Stephen McMillan. Black hole mergers in the universe. *Astrophys. J.*, 528:L17, 2000.
- [220] Konstantin Postnov and Lev Yungelson. The Evolution of Compact Binary Star Systems. *Living Rev. Rel.*, 9:6, 2006.
- [221] Konstantin A. Postnov and Lev R. Yungelson. The Evolution of Compact Binary Star Systems. *Living Rev. Rel.*, 17:3, 2014.
- [222] Madappa Prakash, Ignazio Bombaci, Manju Prakash, Paul J. Ellis, James M. Lattimer, and Roland Knorren. Composition and structure of protoneutron stars. *Phys. Rept.*, 280:1–77, 1997.
- [223] Stephen Privitera, Satyanarayan R. P. Mohapatra, Parameswaran Ajith, Kipp Cannon, Nickolas Fotopoulos, Melissa A. Frei, Chad Hanna, Alan J. Weinstein, and John T. Whelan. Improving the sensitivity of a search for coalescing binary black holes with nonprecessing spins in gravitational wave data. *Phys. Rev.*, D89(2):024003, 2014.
- [224] Reinhard Prix. Template-based searches for gravitational waves: Efficient lattice covering of flat parameter spaces. *Class. Quant. Grav.*, 24:S481–S490, 2007.
- [225] H. Reissner. Ueber die eigengravitation des elektrischen felde nach der einsteinschen theorie. *Annalen der Physik*, 355(9):106–120, 1916.
- [226] Dean Rickles and M. Cécile DeWitt. The role of gravitation in physics: Report from the 1957 chapel hill conference. <http://www.edition-open-sources.org/sources/5/index.html>. Accessed: Jan 23 2018.

- [227] Bernhard Riemann. *Ueber die Hypothesen, welche der Geometrie zu Grunde liegen*, pages 67–83. Springer Vienna, Vienna, 1984.
- [228] Carl L. Rodriguez, Meagan Morscher, Bharath Pattabiraman, Sourav Chatterjee, Carl-Johan Haster, and Frederic A. Rasio. Binary Black Hole Mergers from Globular Clusters: Implications for Advanced LIGO. *Phys. Rev. Lett.*, 115(5):051101, 2015. [Erratum: *Phys. Rev. Lett.* 116, no. 2, 029901 (2016)].
- [229] Soumen Roy, Anand S. Sengupta, and Parameswaran Ajith. Effectual gravitational-wave template banks for coalescing compact binaries using a hybrid placement algorithm. 2017.
- [230] Soumen Roy, Anand S. Sengupta, and Nilay Thakor. Hybrid geometric-random template-placement algorithm for gravitational wave searches from compact binary coalescences. *Phys. Rev.*, D95(10):104045, 2017.
- [231] H.N. Russell. “Giant” and “dwarf” stars. *The Observatory*, 36:324–329, Aug 1913.
- [232] L. Santamaria et al. Matching post-Newtonian and numerical relativity waveforms: systematic errors and a new phenomenological model for non-precessing black hole binaries. *Phys. Rev.*, D82:064016, 2010.
- [233] B. S. Sathyaprakash and S. V. Dhurandhar. Choice of filters for the detection of gravitational waves from coalescing binaries. *Phys. Rev.*, D44:3819–3834, 1991.
- [234] Patricia Schmidt, Mark Hannam, and Sascha Husa. Towards models of gravitational waveforms from generic binaries: A simple approximate mapping between precessing and non-precessing inspiral signals. *Phys. Rev.*, D86:104063, 2012.
- [235] Patricia Schmidt, Mark Hannam, Sascha Husa, and P. Ajith. Tracking the precession of compact binaries from their gravitational-wave signal. *Phys. Rev.*, D84:024046, 2011.
- [236] Karl Schwarzschild. On the gravitational field of a sphere of incompressible fluid according to Einstein’s theory. *Sitzungsber. Preuss. Akad. Wiss. Berlin (Math. Phys.)*, 1916:424–434, 1916.
- [237] Anand S. Sengupta, Sanjeev Dhurandhar, and Albert Lazzarini. A Faster implementation of the hierarchical search algorithm for detection of gravitational waves from inspiraling compact binaries. *Phys. Rev.*, D67:082004, 2003.
- [238] S. L. Shapiro and S. A. Teukolsky. *Black holes, white dwarfs, and neutron stars: The physics of compact objects*. 1983.
- [239] Tom Siegfried. 50 years later, it’s hard to say who named black holes. <https://www.sciencenews.org/blog/context/50-years-later-it%E2%80%99s-hard-say-who-named-black-holes>, 2013. Accessed: 2018-01-15.
- [240] Steinn Sigurdsson and Lars Hernquist. Primordial black holes in globular clusters. *Nature*, 364:423–425, 1993.
- [241] Cambridge Philosophical Society. *Proceedings of the Cambridge Philosophical Society: Mathematical and physical sciences*. Number Bd. 2. University Press, 1876.
- [242] Wolfgang Steinicke. Einstein and the gravitational waves. <http://www.hs.uni-hamburg.de/DE/GNT/events/pdf/steinicke05.pdf>.

- [243] E. C. Stoner. V. the limiting density in white dwarf stars. *The London, Edinburgh, and Dublin Philosophical Magazine and Journal of Science*, 7(41):63–70, 1929.
- [244] E. C. Stoner. Lxxxvii. the equilibrium of dense stars. *The London, Edinburgh, and Dublin Philosophical Magazine and Journal of Science*, 9(60):944–963, 1930.
- [245] Nobert Straumann. On the einstein-grossmann collaboration 100 years ago. <http://www.ihes.fr/~vanhove/Slides/Straumann-IHES-octobre2012.pdf>, 2012. Accessed Jan 27 2018.
- [246] B. Strömngren. On the Interpretation of the Hertzsprung-Russell-Diagram. Mit 4 Abbildungen. *Zeitschrift für Astrophysik*, 7:222, 1933.
- [247] Koh Takahashi, Takashi Yoshida, and Hideyuki Umeda. Evolution of progenitors for electron capture supernovae. *The Astrophysical Journal*, 771(1):28, 2013.
- [248] Takahiro Tanaka and Hideyuki Tagoshi. The Use of new coordinates for the template space in hierarchical search for gravitational waves from inspiraling binaries. *Phys. Rev.*, D62:082001, 2000.
- [249] Andrea Taracchini et al. Effective-one-body model for black-hole binaries with generic mass ratios and spins. *Phys. Rev.*, D89(6):061502, 2014.
- [250] T. M. Tauris et al. Formation of Double Neutron Star Systems. *Astrophys. J.*, 846(2):170, 2017.
- [251] J. H. Taylor, L. A. Fowler, and P. M. McCulloch. Measurements of general relativistic effects in the binary pulsar PSR 1913+16. *Nature*, 277:437–440, 1979.
- [252] K.S. Thorne and A.N. Zytков. Red giants and supergiants with degenerate neutron cores. *Astrophysical Journal Letters*, 199:L19–L24, Jul 1975.
- [253] K.S. Thorne and A.N. Zytков. Stars with degenerate neutron cores. I - Structure of equilibrium models. *Astrophysical Journal*, 212:832–858, Mar 1977.
- [254] A. Tutukov and L. Yungelson. Evolution of massive close binaries. *Nauchnye Informatsii*, 27:70, 1973.
- [255] Samantha A. Usman et al. The PyCBC search for gravitational waves from compact binary coalescence. *Class. Quant. Grav.*, 33(21):215004, 2016.
- [256] Stefano Valenti, David J. Sand, Sheng Yang, Enrico Cappellaro, Leonardo Tartaglia, Alessandra Corsi, Saurabh W. Jha, Daniel E. Reichart, Joshua Haislip, and Vladimir Kouprianov. The discovery of the electromagnetic counterpart of GW170817: kilonova AT 2017gfo/DLT17ck. *Astrophys. J.*, 848(2):L24, 2017.
- [257] Vijay Varma, Parameswaran Ajith, Sascha Husa, Juan Calderón Bustillo, Mark Hannam, and Michael Pürrer. Gravitational-wave observations of binary black holes: Effect of nonquadrupole modes. *Phys. Rev.*, D90(12):124004, 2014.
- [258] Robert M. Wald. *General Relativity*. Chicago Univ. Pr., Chicago, USA, 1984.
- [259] J. Weber. Detection and Generation of Gravitational Waves. *Phys. Rev.*, 117:306–313, 1960.



- [260] J. Weber. On the possibility of detection and generation of gravitational waves. *Colloq. Int. CNRS*, 91:441–450, 1962.
- [261] B. Louise Webster and Paul Murdin. Cygnus X-1-a Spectroscopic Binary with a Heavy Companion ? *Nature*, 235:37–38, 1972.
- [262] Nevin N. Weinberg, Milos Milosavljevic, and Andrea M. Ghez. Stellar dynamics at the Galactic Center with a Thirty Meter Telescope. *Astrophys. J.*, 622:878, 2005.
- [263] J. M. Weisberg, D. J. Nice, and J. H. Taylor. Timing Measurements of the Relativistic Binary Pulsar PSR B1913+16. *Astrophys. J.*, 722:1030–1034, 2010.
- [264] J. M. Weisberg, J. H. Taylor, and L. A. Fowler. GRAVITATIONAL WAVES FROM AN ORBITING PULSAR. *Sci. Am.*, 245:66–74, 1981.
- [265] Rainer Weiss. Interferometric broad band gravitational antenna. grant identification number mps75–04033. [https://dspace.mit.edu/bitstream/handle/1721.1/56655/RLE\\_PR\\_119\\_XV.pdf?sequence=1](https://dspace.mit.edu/bitstream/handle/1721.1/56655/RLE_PR_119_XV.pdf?sequence=1).
- [266] Rainer Weiss. Quarterly progress report 1972, no 105, 54-76. research laboratory of electronics, mit. [https://dspace.mit.edu/bitstream/handle/1721.1/56271/RLE\\_QPR\\_105\\_V.pdf?sequence=1](https://dspace.mit.edu/bitstream/handle/1721.1/56271/RLE_QPR_105_V.pdf?sequence=1), 1972.
- [267] K. Werner, N. J. Hammer, T. Nagel, T. Rauch, and S. Dreizler. On possible oxygen/neon white dwarfs: H1504+65 and the white dwarf donors in ultracompact x-ray binaries. *ASP Conf. Ser.*, 334:165, 2005.
- [268] Karl Wette. Lattice template placement for coherent all-sky searches for gravitational-wave pulsars. *Phys. Rev.*, D90(12):122010, 2014.
- [269] Hermann Weyl. *Allgemeine Relativitätstheorie*. Springer Berlin Heidelberg, Berlin, Heidelberg, 1919.
- [270] J.C. Wheeler, Z. Barkat, and J.-R. Buchler. On the Possibility of Neutron-Star Formation in a Carbon-Detonation Supernova. *Astrophysics Journal Letters*, 162:L129, nov 1970.
- [271] Clifford M. Will and Alan G. Wiseman. Gravitational radiation from compact binary systems: Gravitational wave forms and energy loss to second postNewtonian order. *Phys. Rev.*, D54:4813–4848, 1996.
- [272] Kurtis A. Williams, Michael Bolte, and Detlev Koester. Probing The Lower Mass Limit for Supernova Progenitors and the High-Mass End of the Initial-Final Mass Relation from White Dwarfs in the Open Cluster M35 (NGC 2168). *Astrophys. J.*, 693:355–369, 2009.
- [273] Peter M. Woods, Chryssa Kouveliotou, Mark H. Finger, Ersin Göğüs, Colleen A. Wilson, Sandeep K. Patel, Kevin Hurley, and Jean H. Swank. The prelude to and aftermath of the giant flare of 2004 december 27: Persistent and pulsed x-ray properties of sgr 1806–20 from 1993 to 2005. *The Astrophysical Journal*, 654(1):470, 2007.
- [274] S. E. Woosley and T. A. Weaver. The Physics of supernova explosions. *Ann. Rev. Astron. Astrophys.*, 24:205–253, 1986.
- [275] Wu-Tang et al. Enter the Wu-Tang (36 Chambers). Loud Records, RCA Records, Firehouse Studio in New York City, Nov 1993.

- [276] Dmitrii G Yakovlev, Pawel Haensel, Gordon Baym, and Christopher Pethick. Lev Landau and the concept of neutron stars. *Physics-Uspekhi*, 56(3):289, 2013.
- [277] Sheng Yang, Stefano Valenti, Enrico Cappellaro, David J. Sand, Leonardo Tartaglia, Alessandra Corsi, Daniel E. Reichart, Joshua Haislip, and Vladimir Kouprianov. An Empirical Limit on the Kilonova Rate from the DLT40 One Day Cadence Supernova Survey. *Astrophys. J.*, 851(2):L48, 2017.